Studies on transport phenomena of cohesive granular particles

Satoshi Takada

January 7, 2016

Abstract

In this thesis, we numerically and theoretically study the transport phenomena of cohesive granular particles.

First, we study spatial patterns of cohesive granular gases under a plane shear. From the results of three-dimensional molecular dynamics (MD) simulations, we find various spatial patterns depending on the density, the shear rate, and the dissipation rate. We also find that the velocity distribution function (VDF) near the interface between the dense region and the gas dilute region in the dense-plate coexistence phase deviates from the Gaussian function. Introducing a stochastic model and its corresponding Kramers equation, we have obtained its perturbative VDF, which reproduces the semi-quantitative behavior of the VDF observed in the MD simulations.

Next, we develop the kinetic theory of dilute cohesive granular gases in which the attractive part is described by a square well potential. We derive a set of hydrodynamic equations from the kinetic theory including the dissipation rate and the transport coefficients. We check the validity of our theory by performing the direct simulation Monte Carlo.

Publication list for requirement of this thesis

1. S. Takada, K. Saitoh, and H. Hayakawa,
   "Kinetic theory for dilute cohesive granular gases with a square well potential"
   Submitted to Phys. Rev. E.

2. S. Takada, K. Saitoh, and H. Hayakawa,
   "Simulation of cohesive fine powders under a plane shear"
   Phys. Rev. E 90, 062207 (2014). Featured as Kaleidoscope.

Reference papers

1. K. Saitoh, S. Takada, and H. Hayakawa,
   "Hydrodynamic instabilities in shear flows of dry cohesive granular particles"
   Soft Matter, **11**, 6371–6385 (2015). Selected as Inside front cover.

2. S. Takada and H. Hayakawa,
   "Drag Law of Two Dimensional Granular Fluids"
   to be published in J. Eng. Mech.

3. R. Yoshii, S. Takada, S. Tsuchiya, G. Marmorini, H. Hayakawa, and M. Nitta,
   "Fulde-Ferrell-Larkin-Ovchinnikov states in a superconducting ring with magnetic fields: Phase diagram and the first-order phase transitions"
   Phys. Rev. B **92**, 224512 (2015).

4. S. Takada and H. Hayakawa,
   "Pattern dynamics of cohesive granular particles under plane shear"
   POWDERS AND GRAINS 2013: Proceedings of the 7th International Conference on Micromechanics of Granular Media, AIP Conf. Proc. **1542**, 819–822 (2013).

5. S. Takada and H. Hayakawa,
   "Simulation of pattern dynamics of cohesive granular particles under a plane shear"
   Proceedings of 4th International Symposium on Slow Dynamics in Complex Systems: Keep Going Tohoku, AIP Conf. Proc. **1518**, 741–744 (2013).

Contents

Chapter 1

Introduction

We are surrounded by a plenty of granular materials which behave as unusual solids, liquids, and gases [1]. To understand complex behavior of such systems is important in both physics and industry. Granular meterials are characterized by the repulsive force and the dissipative force, i. e., the energy dissipation during collisions of particles. Because a granular particle is composed of many molecules, there are some excitations of internal vibrations, radiation of sounds, and deformations. Such processes are the origin of dissipations [2–11].

Let us consider a granular gas system without any external forces. The kinetic temperature of this system decreases because of inelastic collisions, where the time evolution of the kinetic temperature is known to obey Haff's law if the system is homogeneous [12]. However, this homogeneous state cannot be maintained as time goes on, because clusters of dense region appear as shown in Fig. 2.1 [13–18]. Such inhomogeneity of granular gases can be understood by granular hydrodynamics [19–29]. Esipov and Pöschel [30] and Noije and Ernst [31] have found that the tail of the velocity distribution function (VDF) deriates from Gaussian for homogeneous cooling system. Such deviations have also been reported for the vibrated system [31–33], sheared system [34], and falling systems [35, 36], and these deviations are usually expressed by expansions of Sonine polynomials [37, 38]. There are some papers to determine the transport coefficients for this system. The most successful tool is the kinetic theory for inelastic hard core system. One can derive the transport coefficients with the aid of Chapman-Enskog expansion [39]. The earliest application of the kinetic theory to dilute granular gases using inelastic Boltzmann equation [40] calculated the stress tensor, and later one derived the transport coefficients [41–43], in which the deviation of VDF from the Maxwellian was ignored. In the precise treatment of later literature, of course, the kinetic theory includes the deviation of VDF from the Maxwellian [31, 44–46]. Brey *et al.* [44] have adopted the homogeneous cooling state as the zeroth order of the Chapman-Enskog expansion.

The kinetic theory has also been applied for the moderately dense gases using inelastic Enskog equation [47]. It should be noted that there exists an alternative method to derive the transport coefficients in terms of Grad's moment method with the aid of Hilbert expansion of the distribution function [48–50], in terms of an anisotropic Maxwellian distribution function [51], or in terms of BGK model [52]. Sela and Goldhirsch [53] and Ramírez *et al.* [54] have shown that Grad method can cover results with those by the Chapman-Enskog method. As Mitarai and Nakanishi [55] and Chialvo and Sundaresan [56] showed, Enskog theory [47] gives precise transport coefficients if the density is lower than the Alder transition point, but it fails to predict correct behavior of the coefficients above the Alder point. Recently, Suzuki and Hayakawa [57] have developed a new theory for sheared granular liquids even near the jamming point. They perturbatively derived a steady-state distribution function which depends on the stress tensor in the limit of the small inelasticity and weakly shear condition. Their obtained shear viscosity is consistent with the result of the molecular dynamics (MD) simulation. It should be noted that the shear viscosity for sheared system is, in general, different from that for homogeneous system even in the dilute limit in contrast to elastic cases, because the base states for two situations are different in inelastic cases [58, 59].

The attractive interaction between particles plays an important role for fine powders such as aerosols, volcanic ashes, flour, and toner particles. Such cohesive forces can cause a liquid-gas phase transition, a variety of cluster formation, and the appearance of a solid-like state below the jamming point. We also indicate that water among grains exists in many situations, and attractive interaction between fine powders becomes important. Thus, the study of cohesive granular materials is important for both physics and industry to treat real granular materials. Once there exists the attractive interaction between grains, grains tend to form clusters as the result of coalescence processes. The earliest treatment of the coalescence processes is Smoluchowski equation, which describe the time evolution of the number of particles of size. One example of an application of the equation is to explain the size distribution of Saturn's ring [60,61]. The interaction between cohesive particles or wet particles is also studied [62–65], which is discussed in chapter 3.

In this thesis, we try to characterize nonequilibrium pattern formation of cohesive fine powders under a plane shear by the three-dimensional MD simulations. We also try to analyze the time evolution of the granular temperature and derive the transport coefficients for dilute cohesive granular gases in freely cooling processes. The organization of this paper is as follows. In the next Chapter, we briefly summarize the results for dry granular gases. In chapter 3, we show various examples to treat the attractive force between particles. In chapter 4, we introduce a hydrodynamic description of cohesive granular particles. In chapter 5, we introduce numerical methods

for MD simulations for soft core particles and hard core particles, and direct simulation Monte Carlo (DSMC) method in details. In chapters 6 and 7, the main parts of this paper, are devoted to show the results of our simulation and derivation of the transport coefficients for dilute cohesive granular particles in terms of the kinetic theory of inelastic Boltzmann equation. In chapter 8, we summarize our results. In Appendix A, we briefly examine the pattern formation of the dissipative Lennard-Jones (LJ) system under a sheared flat boundary condition. In Appendix B, we illustrate the existence of Coulombic friction near the interface of the plate-gases coexistence phase. In Appendix C, we demonstrate that the viscous heating term near the interface is always positive. In Appendix D, we present a perturbative solution of the Kramers equation. In Appendix E, we show the detailed calculation for each moment of the VDF. In Appendix F, we show the detailed calculation of the VDF. In Appendix G, we explain collision geometries for core collisions and grazing collisions to determine the velocity change during collisions in details. In Appendix H, we briefly explain the procedure to obtain the transport coefficients by using the Chapman-Enskog theory. In Appendices I and J, we calculate the second moment of the collision integral and two Sonine coefficients in terms of the kinetic theory, respectively. In Appendix K, we calculate the explicit expressions of the transport coefficients in the high and low temperature limit. In Appendix L, we calculate the Omega integrals and compare the results by the kinetic theory and those by the event-driven MD simulation.

Chapter 2

Inelastic Boltzmann equation for hard core potential

In this chapter, we review the kinetic theory of inelastic Boltzmann equation for hard core potential and the transport coefficients. Next, we explain the structure formation from the stability analysis of the linearized hydrodynamic equations.

2.1 Chapman-Enskog method

Boltzmann equation is the oldest equation in nonequilibrium statistical mechanics. Its quantitative validity in describing molecule gases has already been examined in many times. Inelastic Boltzmann equation has been introduced implicitly by Ogawa [66], and later explicitly by Savage and Jeffrey [40] for dilute granular gases. Let us consider the inelastic Boltzmann equation:

$$\left(\frac{\partial}{\partial t} + \boldsymbol{v}_1 \cdot \boldsymbol{\nabla}\right) f(\boldsymbol{r}, \boldsymbol{v}_1, t) = I(f, f), \tag{2.1}$$

where $f(\boldsymbol{r}, \boldsymbol{v}_1, t)$ is the distribution function for the position $\boldsymbol{r}$ and the velocity $\boldsymbol{v}_1$, and $I(f, f)$ is the collision integral

$$\begin{aligned} I(f,f) =& d^2 \int d\boldsymbol{v}_2 \int d\hat{\boldsymbol{k}} \Theta(-\boldsymbol{v}_{12} \cdot \hat{\boldsymbol{k}}) |\boldsymbol{v}_{12} \cdot \hat{\boldsymbol{k}}| \\ & \times \left[\frac{1}{e^2} f(\boldsymbol{r}, \boldsymbol{v}_1'', t) f(\boldsymbol{r}, \boldsymbol{v}_2'', t) - f(\boldsymbol{r}, \boldsymbol{v}_1, t) f(\boldsymbol{r}, \boldsymbol{v}_2, t) \right]. \end{aligned} \tag{2.2}$$

Here we have introduced the step function $\Theta(x) = 1$ for $x \geq 0$ and $\Theta(x) = 0$ otherwise. We also write the relationship between the pre-collisional velocities $(\boldsymbol{v}_1'', \boldsymbol{v}_2'')$ and the post-collisional velocities $(\boldsymbol{v}_1, \boldsymbol{v}_2)$

$$\boldsymbol{v}_1 = \boldsymbol{v}_1'' - \frac{1+e}{2} (\boldsymbol{v}_{12}'' \cdot \hat{\boldsymbol{k}}) \hat{\boldsymbol{k}}, \quad \boldsymbol{v}_2 = \boldsymbol{v}_2'' + \frac{1+e}{2} (\boldsymbol{v}_{12}'' \cdot \hat{\boldsymbol{k}}) \hat{\boldsymbol{k}} \tag{2.3}$$

with the restitution coefficient e, which is defined by the ratio of the post-collisional relative speed $v_{12} = |\boldsymbol{v}_1 - \boldsymbol{v}_2|$ to the pre-collisional relative speed $\boldsymbol{v}''_{12} = |\boldsymbol{v}''_1 - \boldsymbol{v}''_2|$. We note that the factor $1/e^2$ in the first term in the integrand in Eq. (2.2) is the result from the Jacobian and the collision rule (2.3) for each collision.

2.1.1 Homogeneous cooling state

In this section, let us determine the VDF $f(\boldsymbol{v}, t)$ in freely cooling hard core granular gases based on the inelastic Boltzmann equation (2.1). First, we expand the distribution function in terms of Sonine polynomials [31, 38, 45, 46, 67] as

$$f^{(0)}(\boldsymbol{v}, t) = f_{\rm M}(\boldsymbol{V}) \left[1 + \sum_{\ell=1}^{\infty} a_\ell S_\ell^{(1/2)} \left(\frac{mV^2}{2T(t)} \right) \right], \tag{2.4}$$

where $V = |\boldsymbol{V}| = |\boldsymbol{v} - \boldsymbol{U}|$ is the local velocity fluctuation from the flow velocity $\boldsymbol{U}(\boldsymbol{r}, t)$. $f_{\rm M}(\boldsymbol{V}) = n(m/2\pi T)^{3/2} \exp(-mV^2/2T)$ is the Maxwellian at the temperature T and the number density n, and $S_\ell^{(1/2)}(x)$ is the Sonine polynomial:

$$S_\ell^{(j)}(x) = \sum_{k=0}^{\ell} \frac{(-1)^k \Gamma(j + \ell + 1)}{\Gamma(j + k + 1)(\ell - k)! k!} x^k \tag{2.5}$$

with the Gamma function $\Gamma(x)$. The time evolution of the granular temperature obtained by the product of the Boltzmann equation (2.1) with $mv_1^2/2$ and integrating over $\boldsymbol{v}_1$, is written as

$$\frac{dT}{dt} = -\zeta^{(0)} T, \tag{2.6}$$

where we have introduced the cooling rate for the homogeneous gas

$$\zeta^{(0)} = \frac{2}{3} n d^2 \sqrt{\frac{2T}{m}} \mathcal{M}_2. \tag{2.7}$$

Here, $\mathcal{M}_2$ is the second moment of the dimensionless collision integral

$$\mathcal{M}_2 = -\int d\boldsymbol{c}_1 c_1^2 \tilde{I}(\tilde{f}^{(0)}, \tilde{f}^{(0)}), \tag{2.8}$$

where we have introduced the dimensionless velocity $\boldsymbol{c}_1 = \boldsymbol{v}_1/v_T$ with the thermal velocity $\boldsymbol{v}_T = \sqrt{2T(t)/m}$, the dimensionless collision integral $\tilde{I}(\tilde{f}^{(0)}, \tilde{f}^{(0)}) = (v_T^2/n^2 d^2) I(f^{(0)}, f^{(0)})$, and the dimensionless distribution function $\tilde{f}^{(0)}(\boldsymbol{c}) = (v_T^3/n) f^{(0)}(\boldsymbol{v}, t)$. After some algebra of Eq. (2.8) with the aid of Eq. (2.3), $\mathcal{M}_2$ can be rewritten as [31, 46]

$$\mathcal{M}_2 = -\frac{1}{2} \int d\boldsymbol{c}_1 \int d\boldsymbol{c}_2 \int d\hat{\boldsymbol{k}} \Theta(-\boldsymbol{c}_{12} \cdot \hat{\boldsymbol{k}}) |\boldsymbol{c}_{12} \cdot \hat{\boldsymbol{k}}| \tilde{f}^{(0)}(\boldsymbol{c}_1) \tilde{f}^{(0)}(\boldsymbol{c}_2) \Delta[c_1^2 + c_2^2] \tag{2.9}$$

where $\Delta\psi(\boldsymbol{c}_i) \equiv \psi(\boldsymbol{c}_i') - \psi(\boldsymbol{c}_i)$. It should be noted that the density keeps a constant and the flow velocity is zero in the homogeneous state. Let us determine the explicit form of $\mathcal{M}_2$ under a certain approximation. Many papers assume that the zeroth order distribution function can be well reproduced by the truncation up to the second order Sonine polynomials [31, 38, 44, 46, 67] as

$$\tilde{f}^{(0)} = \phi(c)\left[1 + a_2 S_2^{(1/2)}(c^2)\right], \tag{2.10}$$

with $\phi(c) = \pi^{-3/2}\exp(-c^2)$, where a_1 is automatically zero because the first order moment is absorbed in the definition of the zeroth velocity distribution function. It should be noted that there are some papers studying the effect of the truncation by considering the distribution function up to the third order [68–70]. From now on, we use the truncated distribution function (2.10) as well as the linearization on a_2. Let us determine a_2 in Eq. (2.10) by using the moments of the dimensionless collision integrals. When we use the truncated distribution function (2.10), the n-th moment $\mathcal{M}_p = -\int d\boldsymbol{c}_1 c_1^p \tilde{I}(\tilde{f}^{(0)}, \tilde{f}^{(0)})$ ($p \in \mathbb{N}$) as

$$\begin{cases} \mathcal{M}_2 = \sqrt{2\pi}(1-e^2)(1+\frac{3}{16}a_2), \\ \mathcal{M}_4 = \sqrt{2\pi}(T_1 + a_2 T_2), \end{cases} \tag{2.11}$$

where the coefficients T_1 and T_2 are, respectively, given by

$$T_1 = (1-e^2)\left(\frac{9}{2} + e^2\right), \tag{2.12}$$

$$T_2 = \frac{3}{32}(1-e^2)(69+10e^2) + 2(1+e). \tag{2.13}$$

Here, $\mathcal{M}_4$ is related to $\mathcal{M}_2$ and the fourth moment $\langle c^4 \rangle$ as

$$\frac{4}{3}\mathcal{M}_2\langle c^4\rangle = \mathcal{M}_4. \tag{2.14}$$

Substituting Eqs. (2.11) into Eq. (2.14) with $\langle c^4\rangle = (15/4)(1+a_2)$, we obtain the explicit form of a_2 as

$$a_2 = \frac{16(1-e)(1-2e^2)}{81 - 17e + 30e^2(1-e)}. \tag{2.15}$$

Substituting Eqs. (2.7), (2.11) and (2.15) into Eq. (2.6), we obtain the time evolution of the temperature as

$$T(t) = \frac{T_0}{\left(1 + \frac{t}{\tau}\right)^2} \tag{2.16}$$

with

$$\tau^{-1} \equiv \frac{1}{3} n d^2 \sqrt{\frac{2T_0}{m}} \mathcal{M}_2. \tag{2.17}$$

2.1.2 Hydrodynamic equations

Next, let us derive the transport coefficients which appear in a set of hydrodynamic equations. Multiplying the Boltzmann equations (2.1) by 1, $\boldsymbol{v}_1$, and $mv_1^2/2$ and integrating over $\boldsymbol{v}_1$, we obtain the hydrodynamic equations

$$\frac{\partial n}{\partial t} + \boldsymbol{\nabla} \cdot (n\boldsymbol{U}) = 0, \tag{2.18}$$

$$\frac{\partial \boldsymbol{U}}{\partial t} + \boldsymbol{U} \cdot \boldsymbol{\nabla}\boldsymbol{U} + \frac{1}{mn}\boldsymbol{\nabla} \cdot P = 0, \tag{2.19}$$

$$\frac{\partial T}{\partial t} + \boldsymbol{U} \cdot \boldsymbol{\nabla} T + \frac{2}{3n}\left(P : \boldsymbol{\nabla}\boldsymbol{U} + \boldsymbol{\nabla} \cdot \boldsymbol{q}\right) + \zeta T = 0, \tag{2.20}$$

where $n(\boldsymbol{r}, t)$ is the density field, $\boldsymbol{U}(\boldsymbol{r}, t)$ is the flow velocity, and $T(\boldsymbol{r}, t)$ is the granular temperature. The pressure tensor P, the heat flux $\boldsymbol{q}$, and the cooling rate ζ are, respectively, defined as

$$P_{ij} \equiv \int d\boldsymbol{v} D_{ij}(\boldsymbol{V}) f(\boldsymbol{r}, \boldsymbol{v}, t) + nT\delta_{ij}, \tag{2.21}$$

$$\boldsymbol{q} \equiv \int d\boldsymbol{v} \boldsymbol{S}(\boldsymbol{V}) f(\boldsymbol{r}, \boldsymbol{v}, t), \tag{2.22}$$

$$\zeta \equiv -\frac{m}{3nT}\int d\boldsymbol{v} v^2 I(f, f), \tag{2.23}$$

where $D_{ij}(\boldsymbol{V}) \equiv m(V_i V_j - V^2\delta_{ij}/3)$ and $\boldsymbol{S}(\boldsymbol{V}) \equiv (mV^2/2 - 5T/2)\boldsymbol{V}$. We adopt the constitutive equations at the Navier-Stokes order

$$P = p\delta_{ij} - \eta\left(\nabla_i U_j + \nabla_j U_i - \frac{2}{3}\delta_{ij}\boldsymbol{\nabla} \cdot \boldsymbol{U}\right), \tag{2.24}$$

$$\boldsymbol{q} = -\kappa\boldsymbol{\nabla} T - \mu\boldsymbol{\nabla} n, \tag{2.25}$$

where p is the hydrostatic pressure, η is the shear viscosity, κ is the thermal conductivity, and μ is the coefficient proportional to the density gradient.

To obtain the transport coefficients, we adopt the Chapman-Enskog method [39, 46, 67]. Here, we expand the distribution function around Eq. (2.10) as

$$f = f^{(0)} + \delta f^{(1)} + \cdots \tag{2.26}$$

by a small parameter δ corresponding to the gradients of the fields. Similarly, the time derivative of the distribution function is expanded as

$$\frac{\partial}{\partial t} = \frac{\partial^{(0)}}{\partial t} + \delta\frac{\partial^{(1)}}{\partial t} + \cdots. \tag{2.27}$$

We, thus, rewrite the Boltzmann equation (2.1) as

$$\begin{aligned}&\left(\frac{\partial^{(0)}}{\partial t} + \delta\frac{\partial^{(1)}}{\partial t} + \cdots + \delta\boldsymbol{v}_1 \cdot \boldsymbol{\nabla}\right)\left(f^{(0)} + \delta f^{(1)} + \cdots\right)\\ &= I\left[\left(f^{(0)} + \delta f^{(1)} + \cdots\right), \left(f^{(0)} + \delta f^{(1)} + \cdots\right)\right].\end{aligned} \tag{2.28}$$

The equation at the zeroth order of Eq. (7.39) is reduced to

$$\frac{\partial^{(0)}}{\partial t} f^{(0)} = I\left(f^{(0)}, f^{(0)}\right). \tag{2.29}$$

From Eqs (2.18)–(2.20), the zeroth order hydrodynamic equations are, respectively, given by

$$\frac{\partial^{(0)}}{\partial t} n = 0, \quad \frac{\partial^{(0)}}{\partial t} \boldsymbol{U} = 0, \quad \frac{\partial^{(0)}}{\partial t} T = -\zeta^{(0)} T, \tag{2.30}$$

which are equivalent to those obtained in the previous subsection for the homogeneous cooling state. The zeroth order of the pressure tensor and the heat flux are, respectively, given by

$$P_{ij}^{(0)} = nT\delta_{ij}, \quad \boldsymbol{q}^{(0)} = 0. \tag{2.31}$$

The first-order Boltzmann equation becomes

$$\frac{\partial^{(0)}}{\partial t} f^{(1)} + \left(\frac{\partial^{(1)}}{\partial t} + \boldsymbol{v}_1 \cdot \boldsymbol{\nabla}\right) f^{(0)} = I\left(f^{(0)}, f^{(1)}\right) + I\left(f^{(1)}, f^{(0)}\right). \tag{2.32}$$

The corresponding first-order hydrodynamic equations are, respectively, given by

$$\begin{aligned}
&\frac{\partial^{(1)}}{\partial t} n = -\boldsymbol{\nabla} \cdot (n\boldsymbol{U}), \\
&\frac{\partial^{(1)}}{\partial t} \boldsymbol{U} = -\boldsymbol{U} \cdot \boldsymbol{\nabla} \boldsymbol{U} - \frac{1}{mn} \boldsymbol{\nabla}(nT), \\
&\frac{\partial^{(1)}}{\partial t} T = -\boldsymbol{U} \cdot \boldsymbol{\nabla} T - \frac{2}{3} T \boldsymbol{\nabla} \cdot \boldsymbol{U} - \zeta^{(1)} T,
\end{aligned} \tag{2.33}$$

where the first-order dissipation rate $\zeta^{(1)}$ is defined by

$$\zeta^{(1)} = -\frac{2m}{3nT} \int d\boldsymbol{v} v^2 I\left(f^{(0)}, f^{(1)}\right). \tag{2.34}$$

We note that $\zeta^{(1)}$ becomes zero because of the parity of the integral (2.34) [44, 46, 67]. We assume that the distribution function $f^{(0)}$ depends on time and space only via its moments: the density n, the average velocity $\boldsymbol{U}$ and the temperature T as $f^{(0)} = f^{(0)}[\boldsymbol{v}|n, \boldsymbol{U}, T]$. Then we can rewrite the first-order equation (2.32) as

$$\begin{aligned}
&\frac{\partial^{(0)} f^{(1)}}{\partial t} + J^{(1)}\left(f^{(0)}, f^{(1)}\right) - \zeta^{(1)} T \frac{\partial f^{(0)}}{\partial T} \\
&= f^{(0)} \left(\boldsymbol{\nabla} \cdot \boldsymbol{U} - \boldsymbol{V} \cdot \boldsymbol{\nabla} n\right) + \frac{\partial f^{(0)}}{\partial T} \left(\frac{2}{3} T \boldsymbol{\nabla} \cdot \boldsymbol{U} - \boldsymbol{V} \cdot \boldsymbol{\nabla} T\right) \\
&\quad + \frac{\partial f^{(0)}}{\partial \boldsymbol{V}} \cdot \left((\boldsymbol{V} \cdot \boldsymbol{\nabla}) \boldsymbol{U} - \frac{1}{mn} \boldsymbol{\nabla} P\right),
\end{aligned} \tag{2.35}$$

where

$$J^{(1)}\left(f^{(0)},f^{(1)}\right)=-I\left(f^{(0)},f^{(1)}\right)-I\left(f^{(1)},f^{(0)}\right). \tag{2.36}$$

Equation (2.35) can be rewritten as

$$\begin{aligned}&\frac{\partial^{(0)}f^{(1)}}{\partial t}+J^{(1)}\left(f^{(0)},f^{(1)}\right)-\zeta^{(1)}T\frac{\partial f^{(0)}}{\partial T}\\&=\boldsymbol{A}\cdot\boldsymbol{\nabla}\log T+\boldsymbol{B}\cdot\boldsymbol{\nabla}\log n+C_{ij}\nabla_j U_i,\end{aligned} \tag{2.37}$$

where the coefficients $\boldsymbol{A}$, $\boldsymbol{B}$, and C_{ij} are, respectively, given by

$$\begin{aligned}\boldsymbol{A}(\boldsymbol{V})&=\frac{1}{2}\boldsymbol{V}\frac{\partial}{\partial\boldsymbol{V}}\cdot\left(\boldsymbol{V}f^{(0)}\right)-\frac{T}{m}\frac{\partial}{\partial\boldsymbol{V}}f^{(0)}\\&=\boldsymbol{V}\left[\frac{T}{m}\left(\frac{mV^2}{2T}-1\right)\frac{1}{V}\frac{\partial}{\partial V}+\frac{3}{2}\right]f^{(0)},\end{aligned} \tag{2.38}$$

$$\begin{aligned}\boldsymbol{B}(\boldsymbol{V})&=-\boldsymbol{V}f^{(0)}-\frac{T}{m}\frac{\partial}{\partial\boldsymbol{V}}f^{(0)}\\&=-\boldsymbol{V}\left(\frac{T}{m}\frac{1}{V}\frac{\partial}{\partial V}+1\right)f^{(0)},\end{aligned} \tag{2.39}$$

$$\begin{aligned}C_{ij}(\boldsymbol{V})&=\frac{\partial}{\partial V_i}\left(V_j f^{(0)}\right)-\frac{1}{3}\delta_{ij}\frac{\partial}{\partial\boldsymbol{V}}\cdot\left(\boldsymbol{V}f^{(0)}\right)\\&=\left(V_iV_j-\frac{1}{3}\delta_{ij}V^2\right)\frac{1}{V}\frac{\partial f^{(0)}}{\partial V}.\end{aligned} \tag{2.40}$$

From Eq. (H.1), $f^{(1)}$ is expected to have the form

$$f^{(1)}=\mathcal{A}\cdot\boldsymbol{\nabla}\log T+\mathcal{B}\cdot\boldsymbol{\nabla}\log n+\mathcal{C}_{ij}\nabla_j U_i. \tag{2.41}$$

The relationship between the coefficients $\mathcal{A}$, $\mathcal{B}$, $\mathcal{C}_{ij}$ and $\boldsymbol{A}$, $\boldsymbol{B}$, C_{ij} are, respectively, given by substituting the solution Eq. (2.41) into Eq. (H.1) as:

$$-T\frac{\partial}{\partial T}\left(\zeta^{(0)}\mathcal{A}\right)+J^{(1)}\left(f^{(0)},\mathcal{A}\right)=\boldsymbol{A}, \tag{2.42}$$

$$-\zeta^{(0)}T\frac{\partial\mathcal{B}}{\partial T}-\zeta^{(0)}\mathcal{A}+J^{(1)}\left(f^{(0)},\mathcal{B}\right)=\boldsymbol{B}, \tag{2.43}$$

$$-\zeta^{(0)}T\frac{\partial\mathcal{C}_{ij}}{\partial T}+J^{(1)}\left(f^{(0)},\mathcal{C}_{ij}\right)=C_{ij}, \tag{2.44}$$

where we have used $\zeta^{(1)}=0$ because the coefficient C_{ij} is traceless. The pressure tensor and the heat flux can be written as

$$P_{ij}^{(1)}=-\eta\left(\nabla_i U_j+\nabla_j U_i-\frac{2}{3}\delta_{ij}\boldsymbol{\nabla}\cdot\boldsymbol{U}\right), \tag{2.45}$$

$$\boldsymbol{q}^{(1)}=-\kappa\boldsymbol{\nabla}T-\mu\boldsymbol{\nabla}n. \tag{2.46}$$

Substituting $f = f^{(0)} + f^{(1)}$ and Eq. (2.45) into Eq. (2.21), we obtain the differential equation for the shear viscosity η with respect to T as

$$-\zeta^{(0)} T \frac{\partial \eta}{\partial T} - \frac{2}{5} n d^2 \sqrt{\frac{2T}{m}} \Omega_\eta^e \eta = nT, \tag{2.47}$$

where Ω_η^e is given by

$$\begin{aligned}\Omega_\eta^e =& \int d\boldsymbol{c}_1 \int d\boldsymbol{c}_2 \int d\hat{\boldsymbol{k}} \tilde{\sigma}(\chi, c_{12})(\boldsymbol{c}_{12} \cdot \hat{\boldsymbol{k}}) \phi(c_1)\phi(c_2) \\ &\times \left[1 + \sum_{\ell=1}^{\infty} a_\ell S_\ell(c_1^2)\right] \tilde{D}_{ij}(\boldsymbol{c}_2) \Delta \left[\tilde{D}_{ij}(\boldsymbol{c}_1) + \tilde{D}_{ij}(\boldsymbol{c}_2)\right] \\ =& -\sqrt{2\pi}(1+e)(3-e)\left(1 - \frac{1}{32} a_2\right)\end{aligned} \tag{2.48}$$

with $\tilde{D}_{ij} = D_{ij}/\varepsilon$. By solving Eq. (2.47), we obtain the shear viscosity as

$$\eta = \frac{15}{2(1+e)(13-e)d^2} \sqrt{\frac{mT}{\pi}} \left[1 + \frac{3}{8} \frac{4-3e}{13-e} a_2\right]. \tag{2.49}$$

Similarly, substituting Eq. (7.50) into Eq. (2.22), we obtain the differential equations for the thermal conductivity κ and the coefficient μ with respect to T as

$$\frac{\partial}{\partial T}\left(3\zeta^{(0)} \kappa T\right) + \frac{4}{5} \kappa n d^2 \sqrt{\frac{2T}{m}} \Omega_\kappa^e = -\frac{15}{2} \frac{nT}{m} (1 + 2a_2), \tag{2.50}$$

and

$$-3n\zeta^{(0)} \frac{\partial \mu}{\partial T} - 3\kappa\zeta^{(0)} - \frac{4}{5} n^2 d^2 \sqrt{\frac{2}{mT}} \Omega_\kappa^e \mu = a_2 \frac{15}{2} \frac{nT}{m}, \tag{2.51}$$

respectively, where Ω_κ^e is given by

$$\begin{aligned}\Omega_\kappa^e =& \int d\boldsymbol{c}_1 \int d\boldsymbol{c}_2 \int d\hat{\boldsymbol{k}} \tilde{\sigma}(\chi, c_{12})(\boldsymbol{c}_{12} \cdot \hat{\boldsymbol{k}}) \phi(c_1)\phi(c_2) \\ &\times \left[1 + \sum_{\ell=1}^{\infty} a_\ell S_\ell(c_1^2)\right] \tilde{\boldsymbol{S}}(\boldsymbol{c}_2) \cdot \Delta \left[\tilde{\boldsymbol{S}}(\boldsymbol{c}_1) + \tilde{\boldsymbol{S}}(\boldsymbol{c}_2)\right] \\ =& -\sqrt{2\pi}(1+e)\left(\frac{49-33e}{8} + \frac{19-3e}{256} a_2\right)\end{aligned} \tag{2.52}$$

with $\tilde{\boldsymbol{S}} = \boldsymbol{S}\sqrt{m/\varepsilon^3}$. We obtain the thermal conductivity and the coefficient μ as

$$\kappa = \frac{75}{2(1+e)(9+7e)d^2} \sqrt{\frac{T}{\pi m}} \left[1 + \frac{1}{32} \frac{797 + 211e}{9+7e} a_2\right], \tag{2.53}$$

$$\begin{aligned}\mu =& \frac{750(1-e)}{(1+e)(9+7e)(19-3e)nd^2} \sqrt{\frac{T}{\pi m}} \\ &\times \left[1 + \frac{50201 - 30971e - 7253e^2 + 4407e^3}{80(1-e)(19-3e)(9+7e)} a_2\right],\end{aligned} \tag{2.54}$$

respectively. Brey *et al.* [71] have numerically shown that these results (2.49), (2.53), and (2.54) are consistent with those by the Green-Kubo relations. It is also noted that Brilliantov and Pöschel [46] have checked the magnitude of a_n ($n \geq 2$) as a function of the restitution coefficient, and obtained that a_n ($n \geq 3$) is much smaller than a_2, which ensures that the truncation up to a_2 order is reasonable.

2.2 Structure formation

In Sec. 2.1, we have explained Haff's law for the time evolution of the granular temperature in a homogeneous cooling system. However, it is known that homogeneous system is unstable because granular particles tend to align as time goes on because of inelastic collisions [13, 14, 18, 46]. In the first stage, the system is uniform and homogeneous. Later, the system is still uniform, while correlations of the velocities grow with time, and finally the system becomes spatially inhomogeneous.

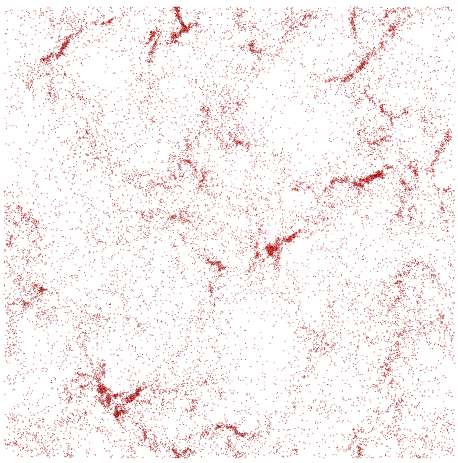

Figure 2.1: A typical time evolution of dry granular gases [13]. There appear clusters of dense region.

Figure 2.1 shows a typical time evolution of the system after the homogeneous state becomes unstable. This structure formation can be understood by the alignment of particles as depicted in Fig. 2.2, i. e. the normal relative speed decreases as a result of an inelastic collision while the tangential speed is conserved in the collision. To understand this instability quantitatively, hydrodynamic description is useful. The linear stability analysis [72, 73] shows that two modes become unstable, one mode is the shear mode and the other is the heat mode. This illustrates that the long wave shear mode of the linearized hydrodynamic equations are always unstable as shown in

Fig. 2.3. The hydrodynamic description for sheared granular materials is also studied [24–29], in which Saitoh and Hayakawa [24, 25] have performed weakly nonlinear analysis and derived the amplitude equation to investigate the instability of the uniformly sheared state.

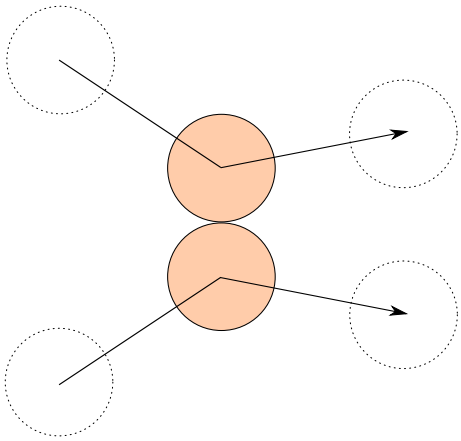

Figure 2.2: A schematic picture of an inelastic collision. Two particles tend to align after the collision because of inelasticity.

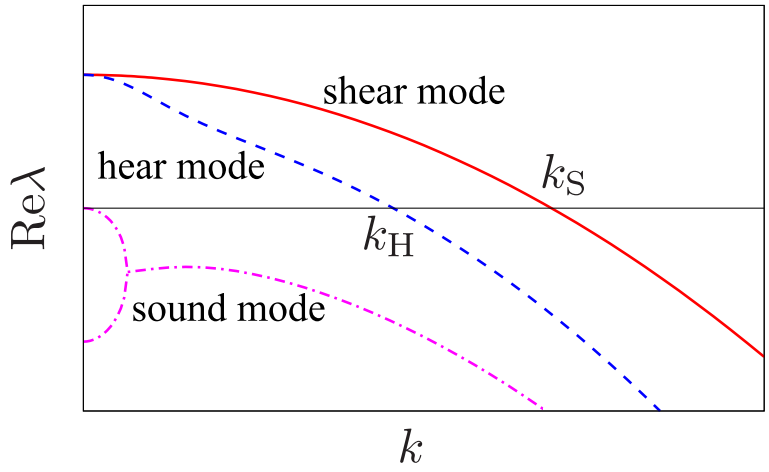

Figure 2.3: Real parts of eigenvalues of a set of hydrodynamic equations. Shear (the red solid line) and heat (the blue dashed line) modes have positive eigenvalues for the long wave length. This figure is drawn based on the calculation corresponding to Fig. 25.3 in Ref. [46].

Chapter 3

Physical properties of cohesive granular particles

In this chapter, let us review physical properties of cohesive granular particles. First, we briefly explain the properties of cohesive granular particles, and then those of wet granular particles. Both granular systems have attractive interactions, while the origins are different.

3.1 Dry cohesive granular particles

The interaction between contacting granular particles usually consists of the repulsive force and the dissipative force proportional to the relative speed. For fine powders such as aerosols, volcanic ashes, flours, and toner particles, however, cohesive force cannot be ignored [75–85]. The origin of this cohesive force for neutral powders is van der Waals force [62]. The positions of the electrons around the nuclear protons cause electric dipoles, which generate an attractive force between two adjacent particles. The simplest expression of this force is the Lennard-Jones (LJ) potential

$$U(r) = -\frac{C}{r^6} + \frac{D}{r^{12}}, \tag{3.1}$$

where $\boldsymbol{r}$ is the relative distance between two particles, and C and D are the fitting parameters, respectively. When the LJ molecules are quenched below the coexistence curve of gas-liquid phases [86–91], a phase ordering process proceeds after nucleation takes place [92–94]. Müller and Luding [95] and Murphy and Subramaniam [96] have studied the homogeneous cooling state for particles having an inelastic hard core with attractive potential. Murphy and Subramaniam have adopted the system having a hard core potential associated with attractive part

$$\Phi(r) = -\Theta(d_0 - r)\frac{AR_{\rm s}}{6r}, \tag{3.2}$$

where A and $R_{\rm s}$ are the effective Hamaker constant and the effective radius of curvature of the particle surface, respectively, and d_0 is the cutoff length. They have obtained that the time evolution of the kinetic energy as

$$\left\langle \frac{\partial E_{\rm kin}(t)}{\partial t} \right\rangle = -\frac{m}{2}\omega T_{\rm g}\left[1 - e^2 \exp\left(-\frac{Ha}{4Ha_{\rm crit}}\right)\right], \tag{3.3}$$

where m is the mass of the particles, e is the restitution coefficient, $T_{\rm g}$ is the granular temperature, $\omega = 16\pi^{1/2}d^2 g_{\rm c} T_g^{1/2}$ is the collision frequency with the diameter d and the radial distribution function at contact $g_{\rm c}$, $Ha = 4\Phi(d_0)/mv^2$ with the relative speed v, and $Ha_{\rm crit} = -e^2/(1-e^2)$. Equation (3.3) obeys Haff's law in the initial stage and decrease faster as time goes on, then approaches Haff's law for $e = 0$. Müller and Luding have also obtained the similar time evolution of the kinetic energy as

$$\left\langle \frac{\partial E_{\rm kin}(t)}{\partial t} \right\rangle = -\frac{m}{2}\omega T_{\rm g}(1-e^2)\left[2 - \exp\left(\frac{Ha}{2}\right)\right], \tag{3.4}$$

which also obeys Haff's law in the initial stage. However, these papers have not discussed the transport coefficients.

There are some papers to study the aggregation and fragmentation processes induced by collisions. The simplest approach to treat the aggregation process is Smoluchowski equation:

$$\frac{dn_k}{dt} = \frac{1}{2}\sum_{i+j=k} C_{ij} n_i n_j - \sum_{i=1}^{\infty} C_{ij} n_i n_k, \tag{3.5}$$

where n_k is the number of particles of size k, C_{ij} is the kinetic coefficients. For specific forms of C_{ij}, Eq. (3.5) is known to be solved analytically.

Recently, Brilliantov *et al.* [60] have applied the kinetic theory to a system including aggregation and breakup as well as inelastic scatterings. They have numerically and analytically solved a rate equation for the cluster size and succeeded to explain the size distribution of dusts in Saturn's ring.

3.2 Wet granular particles

There is another origin of the cohesive force, which is the capillary force for wet granular particles because of the existence of liquids on granular surface [63–65,97]. It is known that there are various states of wet particles: pendular state, funicular state, capillary state, and slurry state depending on the amount of liquids in the system as in Table 3.1 [65]. For the case of capillary state, the formation and the rupture of a capillary bridge coexist as in Fig. 3.1. The magnitude of this force is given by

$$\begin{aligned} F &= 2\pi R\gamma\cos\theta\frac{1 + d_{\rm c}/4R}{1 - d_{\rm c}/2R} \\ &\approx 2\pi R\gamma\cos\theta \end{aligned} \tag{3.6}$$

for $d_c \ll 4R$, where R is the radius of particles, γ is the liquid surface tension, θ is the macroscopic contact angle, and d_c is the vertical distance of the contact lines of a capillary bridge [63,98]. This process is irreversible, which is different from that for fine powders. The Johnson-Kendall-Roberts theory is usually used for the description of the microscopic surface energy for the contact of cohesive particles [99,100].

Table 3.1: A various kind of states depending on the amount of the liquid. This table is depicted based on Table 2 in Ref. [65].

state	schematic picture	physical description
dry	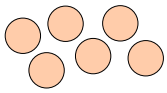	no cohesion
pendular	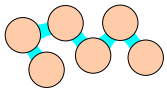	liquid bridge
funicular	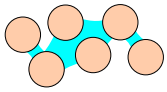	liquid bridge + liquid-filled pore
capillary	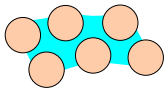	liquid-filled pores
slurry	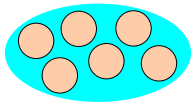	no cohesive interaction

Luding [101] proposed a linear irreversible model for describing the wet interaction as

$$F = \begin{cases} k_1\delta & (k_2(\delta-\delta_0) \geq k_1\delta) \\ k_2(\delta-\delta_0) & (k_1\delta > k_2(\delta-\delta_0) > -k_c\delta) \\ -k_c\delta & (-k_c\delta \geq k_2(\delta-\delta_0)) \end{cases}. \tag{3.7}$$

He and his workers [102] have studied the rheology of cohesive granular materials using this model.

Ulrich *et al.* [103,104] have numerically studied clustering phenomena for wet granular particles without any external forces as in Fig. 3.2. They have phenomenologically derived the time evolution of the granular temperature in the early stage as

$$\frac{3}{2}\frac{dT_g}{dt} = -\frac{1}{2}f_{\rm coll}\Delta E, \tag{3.8}$$

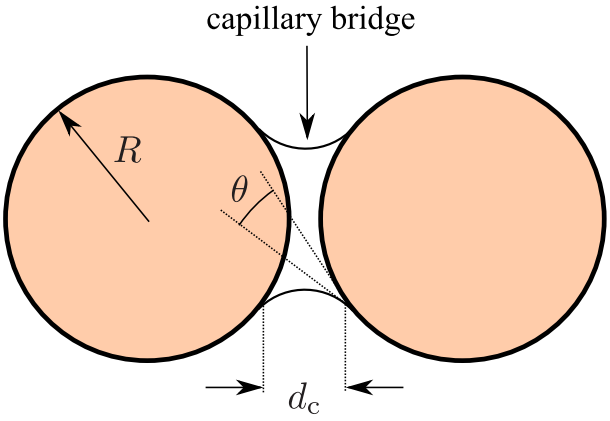

Figure 3.1: A schematic picture of a capillary bridge.

where ΔE is the energy dissipation per one collision and

$$f_{\rm coll} = 8\pi R^2 g_{\rm c} n \sqrt{\frac{T_{\rm g}}{\pi m}}. \tag{3.9}$$

Equations (3.8) and (3.9) show the time evolution of the temperature as

$$T_{\rm g}(t) = \frac{T_{\rm g}^0}{(1 - t/t_0)^2} \tag{3.10}$$

with the initial granular temperature $T_{\rm g}^0$ and the characteristic time scale

$$t_0 = \frac{\sqrt{9\pi m T_{\rm g}^0}}{8\pi R^2 g_{\rm c} \Delta E}. \tag{3.11}$$

They have also demonstrated that the aggregation processes are self-similar and satisfies a scaling law in the late stage.

Royer and his workers [105,106] have experimentally studied a free falling process of wet granular systems. They have obtained the size distribution of the culster and the phase diagram of pattern formation of freely falling particles with respect to the cohesive force and the restitution coefficient.

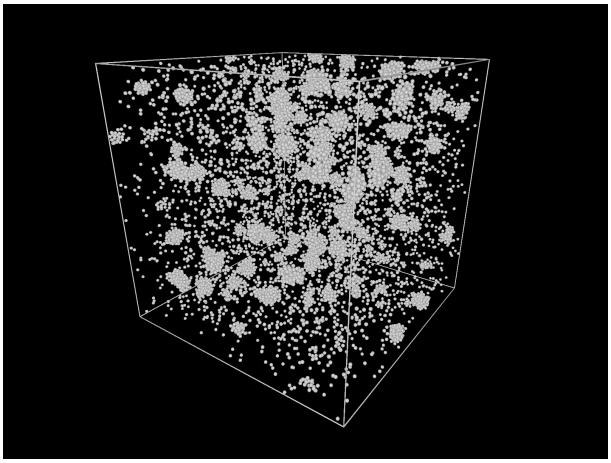

Figure 3.2: A typical pattern of wet granular particles obtained after a freely cooling process without any external forces.

Chapter 4

Hydrodynamic description of cohesive granular particles

In this chapter, let us introduce the hydrodynamic description of cohesive granular particles by K. Saitoh, S. Takada, and H. Hayakawa, "Hydrodynamic instabilities in shear flows of dry cohesive granular particles" Soft Matter, **11**, 6371 (2015) [107]. Note that this is one of the reference papers by the present author. In their paper, they have proposed an extended dynamic van der Waals model originally proposed by A. Onuki [108, 109] to describe hydrodynamic behaviors of a collection of cohesive granular particles. Then, they have studied hydrodynamic instabilities in shear flows of cohesive granular particles with the aid of the dynamic van der Waals model. First, they have introduced a continuum model of cohesive granular particles, where they have modified the dynamic van der Waals theory [108,109] to include the energy dissipation caused by inelastic collisions between granular particles. Then, they have numerically solved the model under a plane shear, where they have adopted the Lees-Edwards boundary condition [110–112]. They have also analyzed the linear stability of homogeneous state to explain observed spatial structures in the presence of a shear rate and inelasticity. Finally, they have discussed and concluded their results.

4.1 Model

In this section, let us explain a continuum model of cohesive granular materials, where the dynamic van der Waals theory for multiphase fluids [108,109] is extended to include the dissipation of energy. First, they have introduced a set of hydrodynamic equations of cohesive granular particles and explained their model of constitutive relations. Second, they adopt the transport coefficients in the hydrodynamic equations predicted by the kinetic theory of granular gases. Third, they have nondimensionalized the

hydrodynamic equations and obtained their homogeneous solution. Fourth, they have solved the hydrodynamic equations numerically. Fifth, they have demonstrated that the neutral curve for the stability of the homogeneous state is determined by the thermodynamic instability.

4.1.1 Hydrodynamic equations

Let us introduce hydrodynamic fields as the mass density, $\rho = mn$, velocity field, $\tilde{u}_i$, and granular temperature, T, where m, n, and $i = x, y, z$ are the particle mass, the number density, and the coordinate, respectively. Dimensionless hydrodynamic fields are introduced as the volume fraction, $\phi = v_0 n$, dimensionless velocity field, $u_i = (t_{\rm m}/d)\tilde{u}_i$, and dimensionless granular temperature, $\theta = T/\varepsilon$, respectively. Then, the nondimensionalized hydrodynamic equations (the continuity equation, the equation of momentum conservation, and the equation of granular temperature) are nondimensionalized as

$$\frac{\mathcal{D}\phi}{\mathcal{D}t} = -\phi \nabla_i u_i, \tag{4.1}$$

$$\phi \frac{\mathcal{D}u_i}{\mathcal{D}t} = \nabla_j \sigma_{ij}, \tag{4.2}$$

$$\frac{d_{\rm m}}{2}\phi \frac{\mathcal{D}\theta}{\mathcal{D}t} = \sigma_{ij}\nabla_i u_j - \nabla_i q_i - \frac{d_{\rm m}}{2}\phi\theta\zeta, \tag{4.3}$$

respectively, where we have adopted Einstein's convention for the dimensionless coordinates ($i, j = x, y, z$) and have introduced the dimensionless material derivative as $\mathcal{D}/\mathcal{D}t \equiv \partial/\partial t + u_i \nabla_i$ with $\partial/\partial t = t_{\rm m}\partial/\partial\tilde{t}$ and $\nabla_i = d\tilde{\nabla}_i$. The last term on the right-hand-side of Eq. (4.3) represents the energy dissipation in the bulk caused by inelastic collisions, where ζ is a dissipation rate.

4.1.2 Constitutive relations

Next, they have discussed the constitutive relations for the stress tensor, σ_{ij}, and the heat flux, q_i. The stress tensor is divided into the viscous and reversible parts as

$$\sigma_{ij} = \tau_{ij} - \pi_{ij}, \tag{4.4}$$

where the viscous part is defined as

$$\tau_{ij} = \eta\left(\nabla_i u_j + \nabla_j u_i\right) + \delta_{ij}\left(\xi - \frac{2}{d_{\rm m}}\eta\right)\nabla_k u_k \tag{4.5}$$

($k = x, y, z$) with the shear viscosity, η, and bulk viscosity, ξ. In the dynamic van der Waals theory [108, 109], the reversible part can be written as

$$\pi_{ij} = (p + p_1)\delta_{ij} + M\nabla_i n \nabla_j n, \tag{4.6}$$

where the static pressure is given by the van der Waals equation of state,

$$p = \frac{nT}{1 - v_0 n} - \varepsilon v_0 n^2, \tag{4.7}$$

with the particle volume, v_0, and well-depth of the attractive potential for cohesive granular particles, ε. In Eq. (4.6), the diagonal part, p_1, and higher order gradient, $M\nabla_i n \nabla_j n$, with the coupling constant, M, represent the increase of energy due to the existence of interfaces between two different phases. In their paper, they have adopted the model used in Refs. [108,109] for the diagonal part, i.e.

$$p_1 = -\frac{M}{2}|\nabla n|^2 - Mn\nabla^2 n, \tag{4.8}$$

where the coupling constant is assumed to be proportional to the temperature as $M = 2d^2 v_0 T$ with the particle diameter, d, measured by the range of square-well potential [1]. It should be noted that the coupling term can be derived from a microscopic model for thermodynamic interfaces [97], but they phenomenologically used this expression, because the microscopic derivation for cohesive granular particles, so far, does not exist.

The heat flux is given by

$$q_i = -\kappa \nabla_i T - \mu \nabla_i n, \tag{4.9}$$

where the first term on the right-hand-side represents Fourier's law with the thermal conductivity, κ. The second term on the right-hand-side of Eq. (4.9), which does not exist in usual fluids, is derived from the kinetic theory of granular gases. The physical origin of this term can be explained as follows: Inelastic collisions in dense regions decrease the kinetic energy of granular particles so that the granular temperature tends to be lower than that in dilute regions [37, 42–44, 46, 47, 49, 113–116].

4.1.3 Transport coefficients and the dissipation rate

Transport coefficients and the dissipation rate of moderately dense dry granular particles are well described by the kinetic theory [37, 42–44, 46, 47, 49, 113–116]. However, it is still a challenging task to derive those for cohesive granular particles, where our attempt to develop a kinetic theory of cohesive granular gases is reported in Chapter 7. In their paper, they only studied moderately dense systems, where the mean volume fraction of granular particles is much lower than 0.5 (but is sufficiently dense to be regarded as a

[1] The complete form of the diagonal part is given by $\tilde{p}_1 = \{(nM' - M)/2\}|\tilde{\nabla}_i n|^2 - nM\tilde{\nabla}_i^2 n - nT(\tilde{\nabla}_i n)\tilde{\nabla}_i(M/T)$ with $M' = \partial M/\partial n$, where the surface tension is given by $\varsigma = \int_{-\infty}^{\infty} M\left(dn_{eq}/dr\right)^2 dr$ with the equilibrium density profile, $n_{eq}(r)$. If the coefficient depends only on the temperature, the diagonal part is reduced to the one used in this paper [108, 109].

finite density system). In addition, they assumed that the granular particles are nearly elastic and are driven by a small shear rate to keep the low granular temperature. Therefore, they used the transport coefficients and the dissipation rate derived from the kinetic theory of inelastic hard-core potentials, where the diameter, d, represents the interaction range of the square-well potential. The nondimensionalized transport coefficients for three-dimensional hard core granular gases are listed in Table 4 in Ref. [107].

4.1.4 Homogeneous solution

It is readily found that the dimensionless hydrodynamic equations (4.1)–(4.3) have a homogeneous solution, $\phi = \phi_0$, $\theta = \theta_0$, and $\boldsymbol{u} = \boldsymbol{u}_0 \equiv (sy, 0, 0)$, corresponding to a uniform shear flow, where ϕ_0, θ_0, and $\boldsymbol{u}_0$ are a homogeneous volume fraction, homogeneous temperature, and uniformly sheared velocity field, respectively. From Eq. (4.3), the homogeneous temperature is found to be

$$\theta_0 = \left\{ \frac{15 f_\eta(\phi_0)}{\pi d_{\rm m}(3h_1 + 32)\phi_0^2 \chi(\phi_0)} \right\} \frac{s^2}{1 - e^2} \ . \tag{4.10}$$

Note that a finite value of the homogeneous temperature represents the balance between the viscous heating and the dissipation of energy, where the dimensionless shear rate and inelasticity are scaled as $s^2 \sim 1 - e^2$.

4.2 Numerical simulations

In this section, the dimensionless hydrodynamic equations (4.1)–(4.3) are numerically solved under a plane shear. Let us explain their numerical setup in Sec. 4.2.1 and show our numerical results in Sec. 4.2.2.

4.2.1 Setup

They prepared a periodic $L \times L \times L$ cubic box with the dimensionless system size, $L/d = 50$, and divided it into $N = 125000$ $(= 50^3)$ small cells with the identical volume, d^3. Next, they randomly distributed the volume fraction, dimensionless temperature, and dimensionless velocity field in each cell around the homogeneous solution, i.e. ϕ_0, θ_0, and $\mathbf{u}_0 = (sy, 0, 0)$, respectively, where the amplitudes of fluctuations are less than 10% of the mean values.

To apply a plane shear to the system, they used the Lees-Edwards boundary condition. They moved the upper and lower image-cells in the opposite directions along the x-axis so that the system is sheared by the scaled shear rate, $s = t_{\rm m}\dot{\gamma}$. Note that the external shear is applied only at the boundaries and there is no external force in the bulk.

4.2.2 Transient dynamics and steady states

Depending on the mean volume fraction, ϕ_0, dimensionless shear rate, s, and inelasticity, $1-e^2$, the system exhibits various transient dynamics and different spatial structures in steady states. Figure 4.1 displays the time evolution of an isosurface, where the shear rate is fixed to be $s = 3 \times 10^{-4}$. In this figure, the mean volume fraction and the inelasticity are given by $\phi_0 = 0.9\phi_{\rm iso}$ and $1-e^2 = 3.0\times10^{-7}$, respectively. Initially, the isosurface has a random structure in space. As time goes on, the density contrast starts to grow and the domains merge with each other to make a large cluster. If the mean volume fraction is relatively low, the cluster is isolated in the bulk so that we observe a spheroidal or a droplet like structure in a steady state. On the other hand, if the mean volume fraction is relatively high, the cluster is elongated along the x-axis by the external shear and we observe either a cylindrical structure or a plate structure in the steady state.

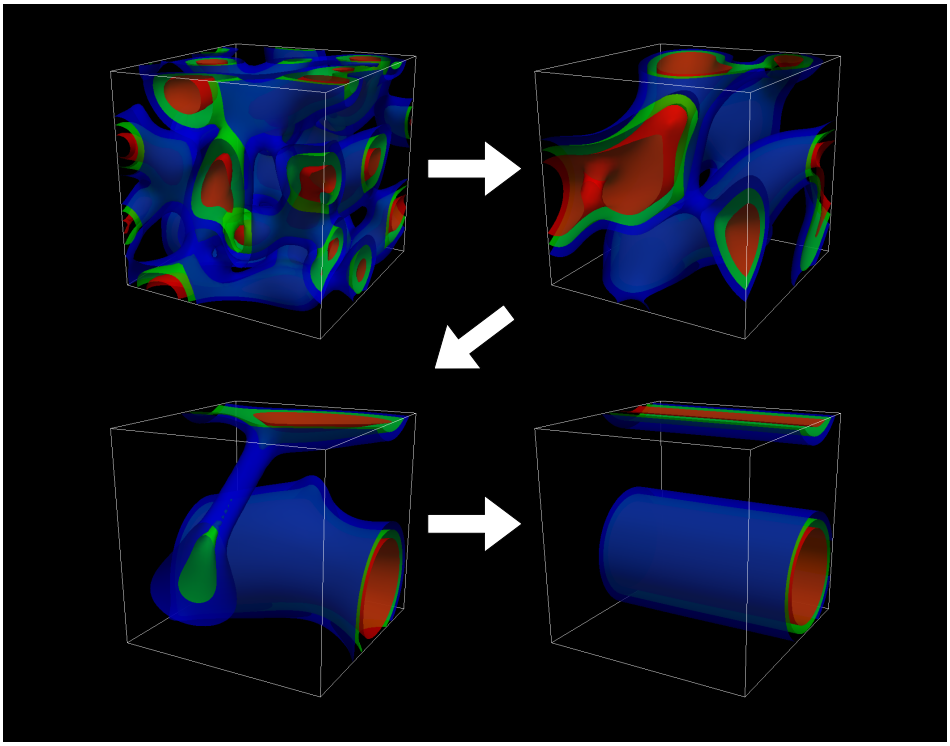

Figure 4.1: A typical time evolution of the system from top left to top right, bottom left, and bottom right. The mean volume fraction is given by $\phi_0 = \phi_{\rm iso}$. The dimensionless shear rate is fixed to $s = 3 \times 10^{-4}$, and the inelasticity is given by $1-e^2 = 3 \times 10^{-7}$. This figure is drawn based on the data of the simulation by Dr. Kuniyasu Saitoh, corresponding to Fig. 2 in Ref. [107].

They then have classified spatial structures of the isosurface based on the dimensionless wave number, (k_x, k_y, k_z), for the spatial undulation of the isosurface. For example, $k_x = 0$ if the isosurface is homogeneous along the x-axis, while $k_x = k_y = 0$ if the isosurface is homogeneous along both the x- and y-axes, etc. Clearly, the homogeneous state is characterized by $k_x = k_y = k_z = 0$. They have obtained (a) a droplet ($k_x = k_y = k_z \neq 0$), (b) a cylinder ($k_x = 0$, $k_y = k_z \neq 0$), (c) a plate ($k_x = k_z = 0$, $k_y \neq 0$), (d) a transverse-cylinder ($k_x = k_y \neq 0$, $k_z = 0$), and (e) a transverse-plate ($k_x = k_y = 0$, $k_z \neq 0$) structure. Here, they also introduced another case which does not belong to any of them as (f) an irregular pattern.

Next, they have mapped their numerical results onto phase diagrams of the dimensionless shear rate, s, and inelasticity, $1 - e^2$ (see Fig. 4 in Ref. [107]). Both the spheroidal and cylindrical structures (droplet and cylinder) can be observed in relatively low volume fractions, while the plate structures (plate and transverse-plate) appear in higher volume fractions. In these figures, the initial homogeneous state is stable if the applied shear is large or the inelasticity is small, where the borders between stable and unstable regions are well described by the solid lines obtained from their linear stability analysis in the next section. If the system is in the unstable region far from the solid line, i.e. in the highly nonlinear regime, the structure in the steady state tends to be irregular and strongly depends on the initial condition.

4.3 Linear stability analysis

They analyzed the linear stability of the homogeneous state to explain the dependence of observed spatial structures on the control parameters, i.e. ϕ_0, s, and $1 - e^2$.

First, they linearized the dimensionless hydrodynamic equations (4.1)–(4.3) against the small fluctuations $\hat{\phi}$, $\hat{\theta}$, and $\hat{\boldsymbol{u}} = (\hat{u}_x, \hat{u}_y, \hat{u}_z)$. Thus, the Fourier transforms of the linearized hydrodynamic equations are written as

$$\left(\frac{\partial}{\partial t} - s k_x \frac{\partial}{\partial k_y} \right) \varphi_{\mathbf{k}} = \mathcal{L} \varphi_{\mathbf{k}}, \tag{4.11}$$

where $\varphi_{\mathbf{k}} = (\phi_{\mathbf{k}}, \theta_{\mathbf{k}}, u_{x\mathbf{k}}, u_{y\mathbf{k}}, u_{z\mathbf{k}})^{\mathrm{T}}$ is a transverse vector of the Fourier coefficients and $\mathcal{L}$ is a time-independent 5×5 matrix.

Next, they introduced a growth rate of the Fourier coefficients as $\hat{\varphi}_{\mathbf{k}}(t) \propto e^{\lambda t}$ so that the linearized hydrodynamic equation (4.11) is reduced to an eigenvalue problem,

$$\left(\mathcal{L} + s k_x \frac{\partial}{\partial k_y} \right) \varphi_{\mathbf{k}} = \lambda \varphi_{\mathbf{k}}. \tag{4.12}$$

They perturbatively solved the eigenvalue problem (4.12) by expanding the eigenvalues, eigenvectors, and matrix into the powers of the wave number,

$k = |\mathbf{k}|$. In their perturbative calculations, the shear rate and inelasticity are scaled as $s \sim O(k^2)$ and $1 - e^2 \sim O(k^4)$, respectively, so that the homogeneous temperature, $\theta_0 \sim s^2/(1-e^2)$, remains as finite. Then, they found that the eigenvalue for the most unstable mode is given by $\lambda = \lambda^{(3)}$ with

$$\lambda^{(3)} \simeq -\frac{2\kappa_0 p_\phi}{d_\mathrm{m}\phi_0 f^2}k^2, \tag{4.13}$$

where they have truncated the expansion of $\lambda^{(3)}$ at k^2 and have introduced $p_\phi = \partial p/\partial\phi$ and a coefficient, $f = \sqrt{a_0\bar{p}_\phi + \phi_0\bar{p}_\theta}$ with $\bar{p}_\phi = p_\phi/\phi_0$ and $\bar{p}_\theta = p_\theta/\phi_0$. Therefore, the eigenvalue is positive if

$$p_\phi = \frac{\partial p}{\partial \phi} < 0, \tag{4.14}$$

i.e. the hydrodynamic instability is triggered if the system is thermodynamically unstable. Note that the other factor in Eq. (4.13) is negative, $-2\kappa_0 k^2/d_\mathrm{m}\phi_0 f^2 < 0$. The neutral curve, i.e. $p_\phi = 0$, is given by the van der Waals equation of state, Eq. (4.7), and the homogeneous granular temperature, Eq. (4.10), where the dimensionless critical shear rate for the neutral stability is found to be

$$s_\mathrm{cr} = \sqrt{\frac{2\pi d_\mathrm{m}\phi_0^3(1-\phi_0)^2\chi(\phi_0)\left\{3h_1(e)+32\right\}(1-e^2)}{15 f_\eta(\phi_0)}}\ . \tag{4.15}$$

The solid lines in the phase diagrams (Fig. 4.2) are given by Eq. (4.15) which well describe the results of the MD presented in Ref. [117]. Note that there is no fitting parameter in Eq. (4.15).

Their perturbative calculation also agrees with the numerical solution of the eigenvalue problem, Eq. (4.12). Figure 4.2 is a stability diagram plotted against the shear rate, s, and inelasticity, $1 - e^2$, where the solid line is the neutral curve, Eq. (4.15). They have confirmed a good agreement between their perturbative calculation and the numerical result.

4.4 Discussion

Though the neutral curve, Eq. (4.15), is given by the stability criterion, Eq. (4.13), the eigenvalue, $\lambda^{(3)} \sim k^2$, is isotropic in the Fourier space. In other words, the isotropic eigenvalue cannot distinguish the observed spatial structures. On the other hand, they also found the anisotropic eigenvalue, $\lambda^{(4)} = se_xe_y - \bar{\eta}_0 k^2$, where its stability criterion corresponds to the shear-induced instability for usual (dry) granular shear flows [24]. Therefore, the thermodynamic instability, $p_\phi < 0$, and the shear-induced instability compete with each other, where the latter also depends on the system size, L, through the wave numbers. We find that the isotropic eigenvalue is always

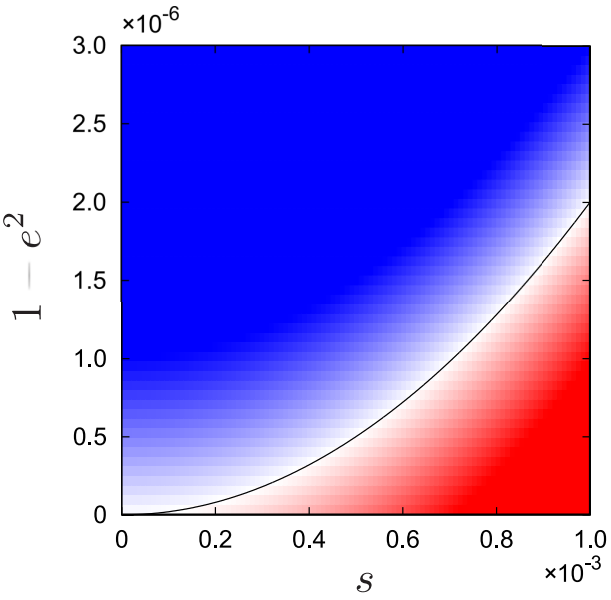

Figure 4.2: Phase diagrams of the spatial structures in the steady states plotted against the dimensionless shear rate, s, and inelasticity, $1 - e^2$. The mean volume fraction is fixed to $\phi_0 = \phi_{\rm iso}$. The red (blue) region shows that the homogeneous state is stable (unstable). This figure is reproduced by courtesy of Dr. Kuniyasu Saitoh, corresponding to Fig. 6 in Ref. [107].

larger than the anisotropic one, i.e. $\lambda^{(3)} > \lambda^{(4)}$, because their system size, $L = 50d$, is too small to observe the shear-induced instability for the range of control parameters studied in this paper. In future, further systematic studies of the pattern selection for larger systems will be needed as well as the weakly nonlinear analysis for the amplitude equation [24, 27, 28].

It should be noted that the temperature increases with time if there is no dissipation of energy. Thus, the homogeneous solution is linearly stable in the absence of inelastic collisions [118]. In our model, however, the mean temperature converges to a finite value in the steady state because the viscous heating is canceled by the energy dissipation. Therefore, the hydrodynamic instability presented in this paper is one of consequences of the dissipative nature of granular materials. We also stress that the thermodynamic instability, $p_\phi < 0$, can be achieved only if the interaction between the particles is attractive. In addition, the stability analyses of dry granular shear flows show that the hydrodynamic instability is induced only by the layering mode ($k_x = 0$), while the non-layering mode ($k_x \neq 0$) is always linearly stable [24, 25, 27, 28]. Therefore, spatial undulations in the sheared direction (x-axis), e.g. droplets, transverse-cylinders, and irregular patterns, do not exist in dry granular systems. Thus, their results are also specific to cohesive granular materials.

Chapter 5

Numerical method

In this chapter, let us briefly explain numerical methods to analyze our system. In the next section, we summarize the MD method for soft core particles. Section 5.2 is devoted to the explanation of the MD for hard core particles. In Sec. 5.3, we explain the outline of the method for the DSMC.

5.1 The method of molecular dynamics simulation of soft core particles

In this section, let us explain the methodology of the MD simulations for soft particles [119,120]. First, we explain an integration scheme of Newton's equation. Let us consider the time evolution of the system is given by Newton equation,

$$\begin{cases} \dfrac{d\boldsymbol{r}_i}{dt} = \dfrac{\boldsymbol{p}_i}{m_i} \\ \dfrac{d\boldsymbol{p}_i}{dt} = \boldsymbol{F}_i \end{cases} , \tag{5.1}$$

where $\boldsymbol{r}_i$ and $\boldsymbol{p}_i$ are, respectively, the position and the momentum of particles i, m is the mass, and $\boldsymbol{F}_i$ is the force acting on i.

There are many methods to solve Eq. (5.1) such as Leap-Frog method, Verlet method, and Adams-Bashforth method. In this thesis, we perform the MD simulation by using the velocity Verlet method

$$\begin{cases} \boldsymbol{r}_i(t+\Delta t) = \boldsymbol{r}_i(t) + \boldsymbol{v}_i(t) + \dfrac{\boldsymbol{F}_i(t)}{2m_i}\Delta t^2 \\ \boldsymbol{v}_i(t+\Delta t) = \boldsymbol{v}_i(t) + \dfrac{\boldsymbol{F}_i(t) + \boldsymbol{F}_i(t+\Delta t)}{2m_i}\Delta t \end{cases} . \tag{5.2}$$

This method is known that the accuracy is Δt^2. It should be noted that the velocity Verlet method is not symplectic integration scheme while the computational cost is lighter than other methods.

5.2 Outline of the algorithm of event-driven molecular dynamics

When the interaction between particles contains a hard core part, the duration of a collision is infinitisimal. The trajectories of such particles are represented by polygonal lines, which have discontinuities in their differentiation. Therefore, we cannot use the method introduced in Sec. 5.1. We need to solve Newton's equation by a different algorithm, known as the event-driven MD, to find a pair of particles of the earliest collision [121,122]. It is known that the event-driven MD is more efficient than the MD for soft particles. Then, we need to replace LJ potential introduced in Eq. (5.1) by a hard core potential surrounded by a square well potential. If we adopt such a model, we need to use the algorithm for the event-driven MD for the corresponding potential.

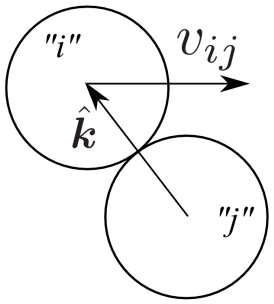

Figure 5.1: A schematic view of a collision geometry, where $\hat{\boldsymbol{k}}$ is the unit vector parallel to $\boldsymbol{r}_{ij} = \boldsymbol{r}_i - \boldsymbol{r}_j$.

Let us consider a system of particles having the hard core surrounded by a square well potential. The position change caused by a collision between i-th and j-th particles satisfies the relation

$$|\boldsymbol{r}_i + \boldsymbol{v}_i \Delta t - (\boldsymbol{r}_j + \boldsymbol{v}_j \Delta t)| = \begin{cases} d & \text{(core)} \\ \lambda d & \text{(outer edge)} \end{cases}. \tag{5.3}$$

The collision geometry for this collision is represented by Fig. 5.1. According to the parameters, the collision time can be calculated as follows:

1. For $(\boldsymbol{v}_{ij} \cdot \hat{\boldsymbol{k}}) < 0$
   (a) in the case of $r_{ij} < \lambda d$
      i. when $(\boldsymbol{v}_{ij} \cdot \hat{\boldsymbol{k}})^2 - v_{ij}^2(r_{ij}^2 - d^2) > 0$ is satisfied, the collision interval is given by

$$\Delta t_{ij} = \frac{-(\boldsymbol{v}_{ij} \cdot \hat{\boldsymbol{k}}) - \sqrt{(\boldsymbol{v}_{ij} \cdot \hat{\boldsymbol{k}})^2 - v_{ij}^2(r_{ij}^2 - d^2)}}{v_{ij}^2}. \tag{5.4}$$

ii. when $(\boldsymbol{v}_{ij} \cdot \hat{\boldsymbol{k}})^2 - v_{ij}^2(r_{ij}^2 - d^2) < 0$ is satisfied, the collision interval is given by

$$\Delta t_{ij} = \frac{-(\boldsymbol{v}_{ij} \cdot \hat{\boldsymbol{k}}) + \sqrt{(\boldsymbol{v}_{ij} \cdot \hat{\boldsymbol{k}})^2 - v_{ij}^2(r_{ij}^2 - \lambda^2 d^2)}}{v_{ij}^2}. \tag{5.5}$$

(b) in the case of $r_{ij} > \lambda d$

i. when $(\boldsymbol{v}_{ij} \cdot \hat{\boldsymbol{k}})^2 - v_{ij}^2(r_{ij}^2 - \lambda^2 d^2) > 0$ is satisfied, the collision interval is given by

$$\Delta t_{ij} = \frac{-(\boldsymbol{v}_{ij} \cdot \hat{\boldsymbol{k}}) - \sqrt{(\boldsymbol{v}_{ij} \cdot \hat{\boldsymbol{k}})^2 - v_{ij}^2(r_{ij}^2 - \lambda^2 d^2)}}{v_{ij}^2}. \tag{5.6}$$

ii. when $(\boldsymbol{v}_{ij} \cdot \hat{\boldsymbol{k}})^2 - v_{ij}^2(r_{ij}^2 - \lambda^2 d^2) < 0$ is satisfied, Eq. (5.3) has no solutions. Thus, there is no collision, i. e. $\Delta t_{ij} = \infty$.

2. For $(\boldsymbol{v}_{ij} \cdot \hat{\boldsymbol{k}}) > 0$

(a) in the case of $r_{ij} < \lambda d$ the collision interval is given by

$$\Delta t_{ij} = \frac{-(\boldsymbol{v}_{ij} \cdot \hat{\boldsymbol{k}}) + \sqrt{(\boldsymbol{v}_{ij} \cdot \hat{\boldsymbol{k}})^2 - v_{ij}^2(r_{ij}^2 - \lambda^2 d^2)}}{v_{ij}^2}. \tag{5.7}$$

(b) in the case of $r_{ij} > \lambda d$, Eq. (5.3) has no solutions. Thus there is no collision, i. e. $\Delta t_{ij} = \infty$.

Correspondingly, the change of the relative velocity during each collision type is given as in Fig. 5.2.

(a) for a core collision ($r_{ij} = d$)

$$\Delta \boldsymbol{v}_{ij} = -2(\boldsymbol{v}_{ij} \cdot \hat{\boldsymbol{k}})\hat{\boldsymbol{k}}, \tag{5.8}$$

(b) for a well enter collision ($r_{ij} = \lambda d$)

$$\Delta \boldsymbol{v}_{ij} = -\left[(\boldsymbol{v}_{ij} \cdot \hat{\boldsymbol{k}}) + \sqrt{(\boldsymbol{v}_{ij} \cdot \hat{\boldsymbol{k}})^2 + \frac{4\varepsilon}{m}}\right]\hat{\boldsymbol{k}}, \tag{5.9}$$

(c) for a well escape collision ($r_{ij} = \lambda d$)

$$\Delta \boldsymbol{v}_{ij} = -\left[(\boldsymbol{v}_{ij} \cdot \hat{\boldsymbol{k}}) - \sqrt{(\boldsymbol{v}_{ij} \cdot \hat{\boldsymbol{k}})^2 - \frac{4\varepsilon}{m}}\right]\hat{\boldsymbol{k}}, \tag{5.10}$$

(d) for a bounce collision ($r_{ij} = \lambda d$)

$$\Delta \boldsymbol{v}_{ij} = -\frac{2}{\lambda^2}(\boldsymbol{v}_{ij} \cdot \hat{\boldsymbol{k}})\hat{\boldsymbol{k}}. \tag{5.11}$$

The iteration of event-driven MD is as follows: (i) We calculate Δt_{ij} for all candidates of collisions and determine the earliest one $\Delta t \leftarrow \Delta t_{ij}$. (ii) We update the time $t + \Delta t$ as

$$\boldsymbol{r}_k(t + \Delta t) \leftarrow \boldsymbol{r}^* + \boldsymbol{v}_k \Delta t. \tag{5.12}$$

(iii) We update the velocities of the collision pair as

$$\boldsymbol{v}_i(t + \Delta t) \leftarrow \boldsymbol{v}_i^* + \frac{1}{2}\Delta \boldsymbol{v}_{ij}, \quad \boldsymbol{v}_j(t + \Delta t) \leftarrow \boldsymbol{v}_j^* - \frac{1}{2}\Delta \boldsymbol{v}_{ij}. \tag{5.13}$$

From the repeat of these processes, we can trace the time evolution of hard core potential.

5.3 The method of direct simulation Monte Carlo

We usually use the DSMC to evaluate the transport coefficients for a system described by the Boltzmann equation instead of using the MD simulation, which was originally introduced by Bird [123] to study rarefied gas [124–127] and later has been extended to dilute inelastic gases [21, 128] and to dense inelastic gases [129, 130]. This is because we should keep the system almost uniform.

In this section, we briefly summarize the DSMC procedure [123, 125–127, 131], which is a numerical technique to obtain the solution of the Boltzmann equation at $t + \Delta t$ from that at t. For small Δt, the velocity distribution function at $t + \Delta t$ is given by

$$f(\boldsymbol{v}, t + \Delta t) = f(\boldsymbol{v}, t) + \frac{\partial f(\boldsymbol{v}, t)}{\partial t}\Delta t. \tag{5.14}$$

Substituting the Boltzmann equation (7.17) into this, we obtain

$$\begin{aligned} f(\boldsymbol{v}, t + \Delta t) &= (1 - \Delta t D + \Delta t J)\, f(\boldsymbol{v}, t) \\ &= (1 + \Delta t J)\,(1 - \Delta t D)\, f(\boldsymbol{v}, t) + \mathcal{O}\left(\Delta t^2\right), \end{aligned} \tag{5.15}$$

where we have introduced $Df = \boldsymbol{v} \cdot \boldsymbol{\nabla} f$ and $Jf = I(f, f)$ for simplicity. Equation (5.15) shows that the time evolution of the VDF can be separated into two parts: advective process and collision process. According to this separation, DSMC iteration is as follows: (i) We determine the time step Δt smaller than $L/v_{\max}$, where L is the system size and $v_{\max}$ is the maximum speed among the particles, which is evaluated as $v_{\max} = 5v_{\mathrm{T}}$ with the thermal velocity v_{T}. In this paper, we adopt $\Delta t = 0.2L/v_{\max}$. (ii) We move the particles during Δt without any collisions as

$$\boldsymbol{r}_i^* = \boldsymbol{r}_i(t) + \boldsymbol{v}_i \Delta t, \tag{5.16}$$

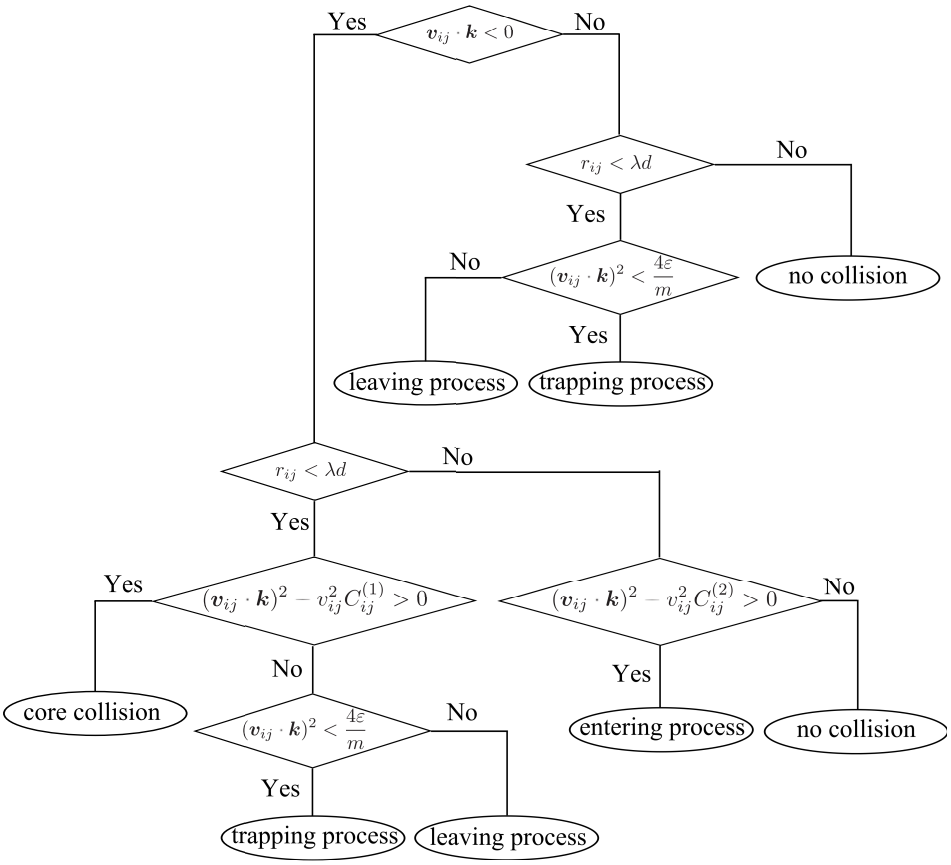

Figure 5.2: Schematic description of collisions for event-driven MD. Here, $C_{ij}^{(1)} = r_{ij}^2 - d^2$ and $C_{ij}^{(2)} = r_{ij}^2 - \lambda^2 d^2$. This figure is drawn based on Fig. 1 in Ref. [121].

which corresponds to update the VDF $f^*(\boldsymbol{v}, t) = (1 - \Delta t D)\, f(\boldsymbol{v}, t)$. (iii) We update the velocities of the particles due to collisions. We randomly determine the collision without taking into account the actual positions of the particles. The square of the collision parameter, b^2, is chosen in the range $0 < b^2 < \lambda^2 d^2$ at random. A pair of colliding particles changes the velocities according to rule in Eqs. (7.19) and (7.20) for a hard core collisions and Eqs. (7.19) and (7.21) for a grazing collision. Here, the number of collisions N_c is evaluated as $\pi(\lambda d)^2 N^2 v_{\max} \Delta t$, which is proportional to the total cross section, the maximum speed, and the time step Δt. This process corresponds to obtain $f(\boldsymbol{v}, t + \Delta t) = (1 + \Delta t J)\, f^*(\boldsymbol{v}, t)$. (iv) We update the time $t + \Delta t$ as

$$\begin{cases} \boldsymbol{r}_i(t + \Delta t) \leftarrow \boldsymbol{r}_i^* \\ \boldsymbol{v}_i(t + \Delta t) \leftarrow \boldsymbol{v}_i^* \end{cases} . \tag{5.17}$$

DSMC is known to be equivalent to the Boltzmann equation in the dilute limit. Montanero and Santos [132] have extended the DSMC method to Enskog equation (Enskog Simulation Monte Carlo) for moderately dense gases, in which they have considered the collisional parts of the pressure tensor and the heat flux, which are ingnored for a dilute system. Brey *et al.* [133] have extended DSMC method to dilute granular systems, in which collisions are inelastic. They have obtained a consistent results with the prediction of the kinetic theory.

Chapter 6

Simulation of cohesive fine powders under a plane shear

Abstract

Three-dimensional MD simulations of cohesive dissipative powders under a plane shear are performed. We find the various phases depending on the dimensionless shear rate and the dissipation rate as well as the density. We also find that the shape of clusters depends on the initial condition of velocities of particles when the dissipation is large. Our simple stochastic model reproduces the non-Gaussian velocity distribution function appearing in the coexistence phase of a gas and a plate.

6.1 Introduction

In this chapter we try to characterize nonequilibrium pattern formation of cohesive fine powders under the plane shear by the three-dimensional MD simulations of the dissipative Lennard-Jones (LJ) molecules under the Lees-Edwards boundary condition [110]. In our previous paper [134] we mainly focused on the effect of dissipation on the pattern formation in Sllod dynamics [135, 136]. In this study, we systematically study it by scanning a large area of parameter space to draw the phase diagrams with respect to the density, the dimensionless shear rate, and the dissipation rate without the influence of Sllod dynamics.

The organization of this chapter is as follows. In the next section we introduce our model and setup for this study. Section 6.3, the main part of this paper, is devoted to exhibiting the results of our simulation. In Sec. 6.3.1 we show the phase diagrams for several densities, each of which has various distinct steady phases. We find that the system has a quasi-particle-hole symmetry. We also find that the steady states depend on the initial condition of velocities of particles when the dissipation is large. In Sec. 6.3.2 we

analyze the velocity distribution function and try to reproduce it by solving the Kramers equation with Coulombic friction under the shear. In Secs. 6.4 and 6.5 we discuss and summarize our results, respectively. In Appendix A we study the pattern formation of the dissipative LJ system under the physical boundary condition. In Appendix B we illustrate the existence of Coulombic friction near the interface of the plate-gases coexistence phase. In Appendix C we demonstrate that the viscous heating term near the interface is always positive. In Appendix D we present a perturbative solution of the Kramers equation. In Appendix E we show the detailed calculations for each moment. In Appendix F we show the detailed calculations of the velocity distribution function.

6.2 Simulation Model and Setup

In this section, we explain our model and setup of the MD simulation for cohesive fine powders under a plane shear. We introduce our model of cohesive fine powders and explain our numerical setup.

6.2.1 Model

We assume that the interaction between two cohesive fine powders can be described by the LJ potential and an inelastic force caused by collisions with finite relative speeds. The explicit expression of the LJ potential is given by

$$U^{\mathrm{LJ}}(r_{ij}) = 4\varepsilon\Theta(\sigma_{\mathrm{c}} - r_{ij})\left[\left(\frac{\sigma}{r_{ij}}\right)^{12} - \left(\frac{\sigma}{r_{ij}}\right)^{6}\right] \tag{6.1}$$

with a step function $\Theta(r) = 1$ and 0 for $r > 0$ and $r \leq 0$, respectively, where ε, σ, and r_{ij} are the well depth, the diameter of the repulsive core, and the distance between the particles i and j, respectively. Here we have introduced the cutoff length $r_{\mathrm{c}} = 3\sigma$ to save the computational cost, i.e., $U^{\mathrm{LJ}}(r) = 0$ for $r \geq r_{\mathrm{c}}$. To model the inelastic interaction, we introduce a viscous force between two colliding particles as

$$\boldsymbol{F}^{\mathrm{vis}}(\boldsymbol{r}_{ij}, \boldsymbol{v}_{ij}) = -\zeta\Theta(\sigma - r_{ij})(\boldsymbol{v}_{ij} \cdot \hat{\boldsymbol{r}}_{ij})\hat{\boldsymbol{r}}_{ij}, \tag{6.2}$$

where ζ, $\hat{\boldsymbol{r}}_{ij} \equiv \boldsymbol{r}_{ij}/r_{ij}$, and $\boldsymbol{v}_{ij} = \boldsymbol{v}_i - \boldsymbol{v}_j$ are the dissipation rate, a unit vector parallel to $\boldsymbol{r}_{ij} = \boldsymbol{r}_i - \boldsymbol{r}_j$, and the relative velocity between the particles, respectively. Here $\boldsymbol{r}_\alpha$ and $\boldsymbol{v}_\alpha$ ($\alpha = i,\ j$) are, respectively, the position and velocity of the particle. It should be noted that the range of inelastic interaction is only limited within the distance σ. From Eqs. (6.1) and (6.2) the force acting on the ith particle is given by

$$\boldsymbol{F}_i = -\sum_{j\neq i} \boldsymbol{\nabla}_i U^{\mathrm{LJ}}(r_{ij}) + \sum_{j\neq i} \boldsymbol{F}^{\mathrm{vis}}(\boldsymbol{r}_{ij}, \boldsymbol{v}_{ij}). \tag{6.3}$$

Our LJ model has advantage of knowing the detailed properties in equilibrium [86–91]. The normal restitution coefficient e, defined as the ratio of post-collisional speed to pre-collisional speed, depends on both the dissipation rate ζ and incident speed. For instance, the particles are nearly elastic, i.e., the restitution coefficient $e = 0.994$ for the case of $\zeta = \sqrt{m\varepsilon/\sigma^2}$ and the incident speed $\sqrt{\varepsilon/m}$, where m is the mass of each colliding particle. Figure 6.1 plots the restitution coefficient against the dimensionless dissipation rate $\zeta^* = \zeta\sqrt{m\varepsilon/\sigma^2}$, where the incident speeds are given by $4\sqrt{\varepsilon/\pi m}$ and $4\sqrt{3\varepsilon/2\pi m}$. We restrict the dissipation rate to small values in the range $0 < \zeta^* \leq 3.2$. Note that small and not too large inelasticity is necessary to reproduce a steady coexistence phase between a dense and a dilute region, which will be analyzed in detail in this study. In this study we use three dimensionless parameters to characterize a system: the dimensionless density $n^* = n\sigma^3 N\sigma^3/L^3$, the shear rate $\dot{\gamma}^* = \dot{\gamma}\sqrt{m\sigma^2/\varepsilon}$, and the dissipation rate $\zeta^* = \zeta\sqrt{m\varepsilon/\sigma^2}$. It should be noted that the well depth ε is absorbed in the dimensionless shear rate and the dissipation rate. Thus, we may regard the control of two independent parameters as the change of the well depth.

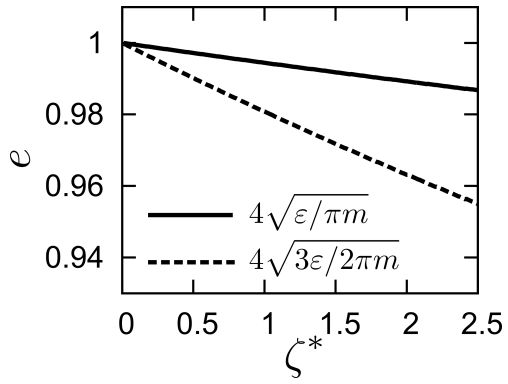

Figure 6.1: The relationship between the dimensionless dissipation rate ζ^* and the coefficient of restitution e when the pre-collisional relative velocities (solid and dashed lines) are given by $4\sqrt{\varepsilon/\pi m}$ and $4\sqrt{3\varepsilon/2\pi m}$, respectively.

6.2.2 Setup

Figure 6.2 is a snapshot of our MD simulations for a uniformly sheared state, where we randomly distribute $N = 10^4$ particles in a cubic periodic box and control the number density n by adjusting the linear system size L. We first equilibrate the system by performing the MD simulations with the Weeks-Chandler-Andersen potential [137, 138] during a time interval $100\sqrt{m\sigma^2/\varepsilon}$. We set the instance of the end of the initial equilibration process as the origin of the time for later discussion. Then we replace the interaction between

particles by the truncated LJ potential 6.1 with the dissipation force 6.2 under the Lees-Edwards boundary condition. As shown in Appendix A, the results under the Lees-Edwards boundary condition are almost equivalent to those under the flat boundary. The time evolution of position $\boldsymbol{r}_i = (x_i, y_i, z_i)$ is given by Newton's equation of motion $md^2\boldsymbol{r}_i/dt^2 = \boldsymbol{F}_i$.

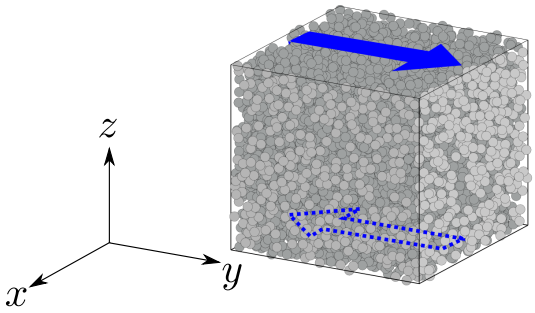

Figure 6.2: A snapshot of our simulation in a uniformly sheared state. We apply a plane shear in xy plane, that is, we choose y-axis as the shear direction and z-axis as the velocity gradient direction.

6.3 Results

In this sectionwe present the results of our MD simulations. In Sec. 6.3.1 we draw phase diagrams of the spatial structures of cohesive fine powders. In Sec. 6.3.2 we present the results of velocity distribution functions and reproduce it by solving a phenomenological model.

6.3.1 Phase diagram

Figure 6.3 displays typical patters formed by the particles in their steady states, which are characterized by the dimensionless parameters n^*, $\dot{\gamma}^*$, and ζ^* as listed in Table 6.1. Figure 6.4 shows phase diagrams in the steady states for (a) $n^* = 0.0904$, (b) $n^* = 0.156$, (c) $n^* = 0.305$, and (d) $n^* = 0.723$. Three of these phases, those in Figs. 6.3(a), 6.3(d), and 6.3(g), are similar to those observed in a quasi-two-dimensional case with Sllod dynamics [134]. If the shear is dominant, the system remains in a uniformly sheared phase [Fig. 6.3(a)]. However, if the viscous heating by the shear is comparable to the energy dissipation, we find that a spherical droplet, a dense cylinder, and a dense plate coexist for extremely dilute ($n^* = 0.0904$), dilute ($n^* = 0.156$), and moderately dense ($n^* = 0.305$) gases, respectively [Fig. 6.3(b)–6.3(d)]. These three coexistence phases are realized by the competition between the equilibrium phase transition and the dynamic instability caused by inelastic collisions. Furthermore, if the energy dissipation is dominant, there are

no gas particles in steady states [Fig. 6.3(e)–6.3(g)]. For an extremely-high-density case ($n^* = 0.723$), we observe an inverse cylinder, where the vacancy forms a hole passing through the dense region along the y-axis [Fig. 6.3(h)], and an inverse droplet, where the shape of the vacancy is spherical [Fig. 6.3(i)]. In our simulation, the role of particles in a dilute system corresponds to that of vacancies in a dense system. Thus, the system has a quasi-particle-hole symmetry.

Moreover, the shape of clusters depends on the initial condition of the velocities of particles, even though a set of parameters such as the density, the shear rate, the dissipation rate, and the variance of the initial velocity distribution function is identical when the dissipation is strong. We observe a dense plate parallel to the xy-plane [Fig. 6.5(a)], a dense plate parallel to the yz-plane [Fig. 6.5(b)], and a dense cylinder parallel to the y-axis [Fig. 6.5(c)] under the identical set of parameters. This initial velocity dependence appears in the region far from the coexistence phases, where the system evolves from aggregates of many clusters (see Fig. 6.6).

Table 6.1: The dimensionless parameters used in Fig. 6.3.

Phase	n^*	$\dot{\gamma}^*$	ζ^*
(a)	0.305	10^{-1}	10^{-2}
(b)	0.0904	$10^{-0.5}$	$10^{0.5}$
(c)	0.156	$10^{-0.5}$	10^{0}
(d)	0.305	$10^{-0.2}$	$10^{0.2}$
(e)	0.0904	10^{-2}	10^{-1}
(f)	0.156	10^{-1}	$10^{-0.75}$
(g)	0.305	10^{-1}	10^{-1}
(h)	0.723	10^{-2}	10^{-1}
(i)	0.723	10^{-2}	10^{-2}

6.3.2 Velocity distribution function

We also measure the velocity distribution function (VDF) $P(u_i)$ $(i = x, y, z)$, where u_i is the velocity fluctuation around the mean velocity field $\bar{v}_i$ averaged over time and different samples in the steady state. For simplicity, we focus only on the following three phases: the uniformly sheared phase [Fig. 6.3(a)], the dense-plate coexistence phase [Fig. 6.3(d)], and the dense-plate cluster phase [Fig. 6.3(g)]. In this paper we use the width $z = \sigma$ for bins in the z-direction, while the bin sizes in both the x and y-directions are L to evaluate the VDF from our MD simulations as in Fig. 6.7. It is remarkable that the VDF is almost an isotropic Gaussian function for the phases corresponding to Figs. 6.3(a) and 6.3(g) as well as deep inside both the dense and the

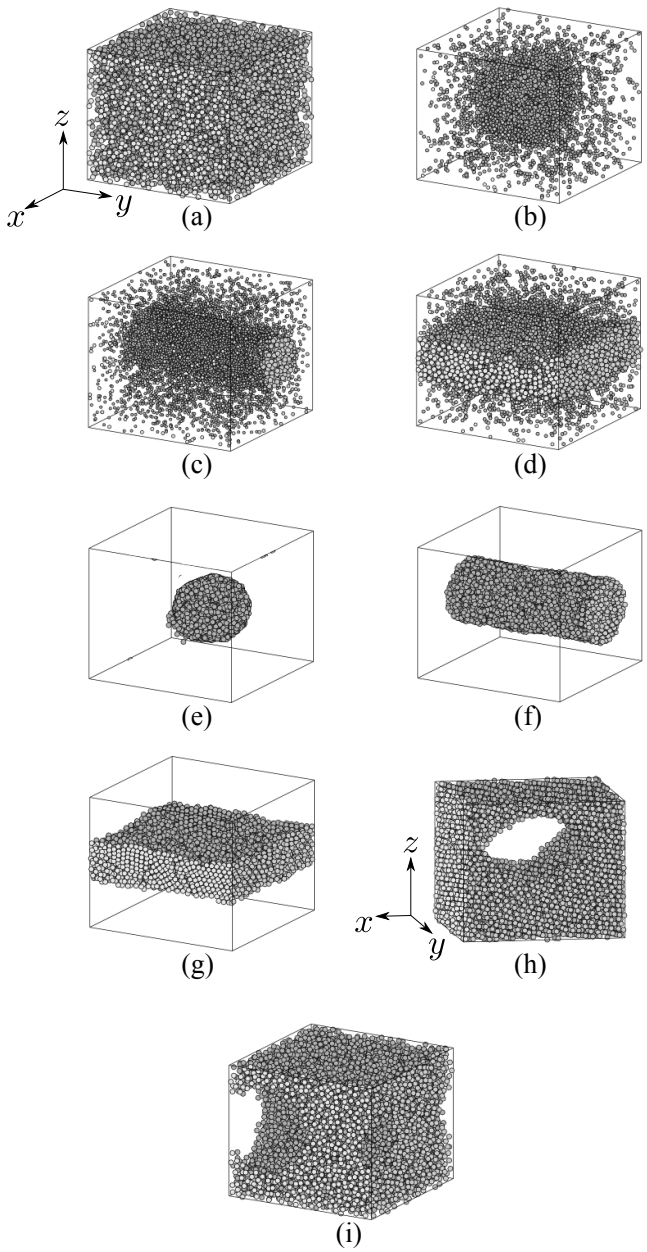

Figure 6.3: (Color online) Steady patterns made of the particles under the plane shear: (a) uniformly sheared phase, (b) coexistence of a spherical-droplet and gas, (c) coexistence of a dense-cylinder and gas, (d) coexistence of a dense-plate and gases, (e) an isolated spherical-droplet, (f) an isolated dense-cylinder, (g) an isolated dense-plate, (h) an inverse cylinder, and (i) an inverse droplet, where the corresponding dimensionless parameters n^*, $\dot{\gamma}^*$, and ζ^* for (a)–(i) are listed in Table 6.1. We note that gas particles in (b), (c) and (d) are drawn smaller than the real size for visibility.

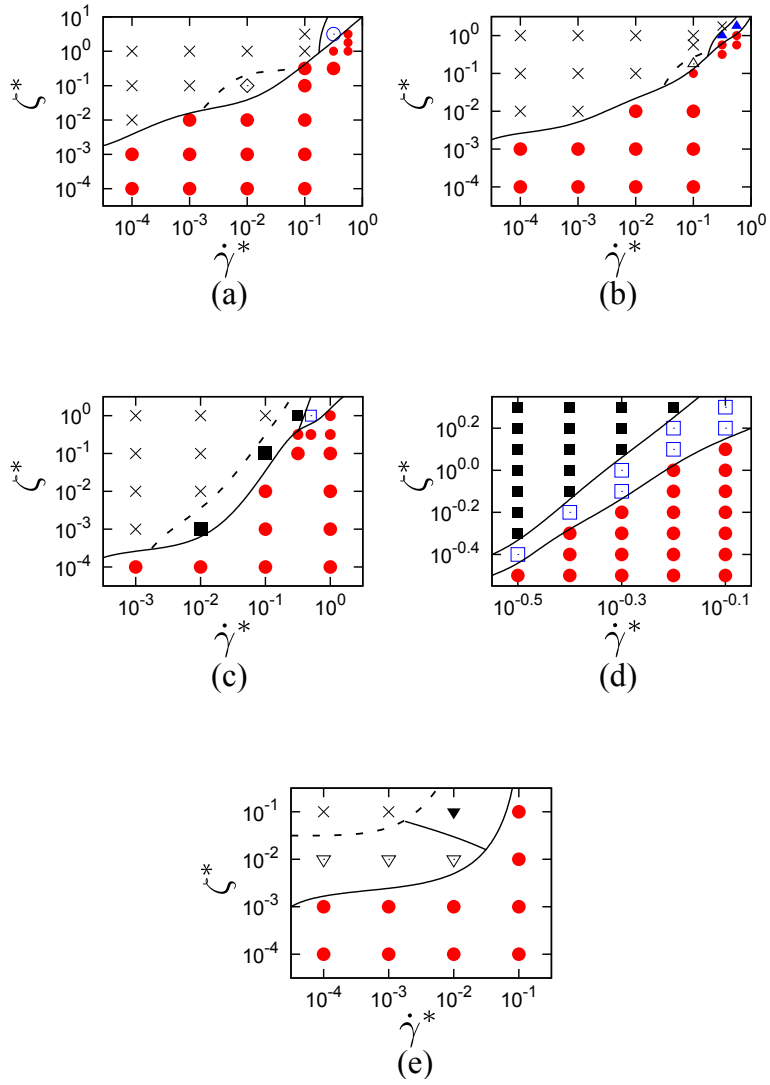

Figure 6.4: (Color online) Phase diagrams for various densities, where the dimensionless densities are given by (a) $n^* = 0.0463$, (b) 0.156, (c) 0.305, (d) 0.305 for $10^{-0.5} \leq \dot{\gamma}^* \leq 10^{-0.1}$, and (e) 0.723, respectively. The spatial patterns corresponding to Fig. 6.3(a)–(i) are represented by red filled circles [Fig. 6.3(a)], blue open circles [Fig. 6.3(b)], blue filled upper triangles [Fig. 6.3(c)], blue open squares [Fig. 6.3(d)], black open diamond [Fig. 6.3(e)], black open upper triangles [Fig. 6.3(f)], black filled squares [Fig. 6.3(g)], black filled lower triangles [Fig. 6.3(h)], and black filled triangles [Fig. 6.3(i)], respectively. The steady states represented by the cross marks show various patterns depending on the initial velocities of particles.

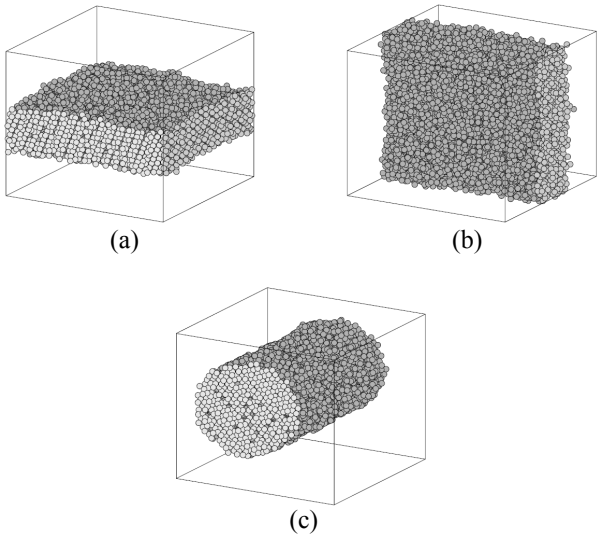

Figure 6.5: (Color online) Typical examples of initial configuration dependence when we start from the identical parameters ($n^* = 0.305$, $\dot{\gamma}^* = 10^{-3}$, $\zeta^* = 10^{-2}$): (a) a dense-plate cluster parallel to xy plane, (b) a dense-plate cluster parallel to yz plane and (c) a dense-cylinder cluster parallel to x-axis.

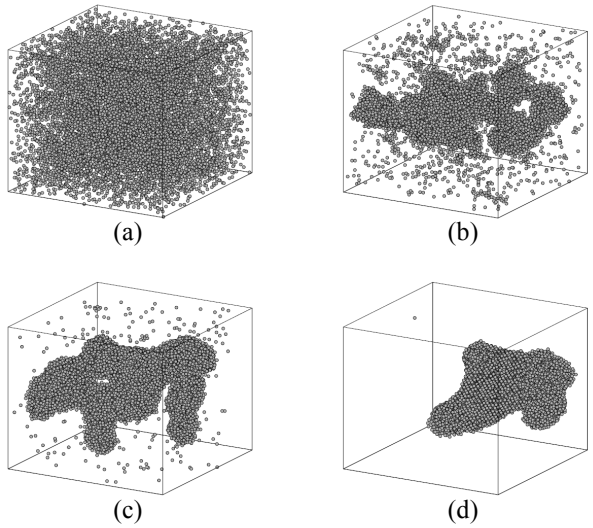

Figure 6.6: (Color online) Time evolution of configurations for $n^* = 0.0904$, $\dot{\gamma}^* = 10^{-1}$, $\zeta^* = 10^{0.5}$. (a) $t^* = 0$, (b) 50, (c) 100, and (d) 550.

gas regions in the coexistence phase in Fig. 6.3(d) [see Figs. 6.8(a)–6.8(d)]. This is because we are interested in weak shear and weak dissipation cases without the influence of gravity. On the other hand, the VDF is nearly equal to an anisotropic exponential function [35, 36] in the vicinity of the interface between the dense and the gas regions in the coexistence phase corresponding to Fig. 6.3(d) as in Figs. 6.8(e)–6.8(g). We now explain the non-Gaussian feature near the interface by a simple stochastic model of a tracer particle subjected to Coulombic friction (the justification to use such a model is explained in Appendix B). Let us consider a situation in which a gas particle hits and slides on the wall formed by the particles in the dense region (see Fig. 6.9). Because the velocity gradient in the gas region is almost constant as shown in Fig. 6.10, we may assume that a tracer particle in the gas near the interface is affected by a plane shear. Moreover, the tracer particle on a dense region may be influenced by Coulombic friction (see Appendix B). When we assume that the collisional force among gas particles can be written as the Gaussian random noise $\boldsymbol{\xi}$, the equations of motion of a tracer particle at the position r may be given by

$$\frac{d\boldsymbol{r}}{dt} = \frac{\boldsymbol{p}}{m} + \dot{\gamma} z \hat{\mathrm{e}}_y, \tag{6.4}$$

$$\frac{d\boldsymbol{p}}{dt} = -\mu F_0 \frac{\boldsymbol{p}}{|\boldsymbol{p}|} - \dot{\gamma} p_z \hat{\boldsymbol{e}}_y + \boldsymbol{\xi}, \tag{6.5}$$

where p is a peculiar momentum, which is defined by Eq. (6.4). Here we have introduced the friction constant μ_0 and the effective force F_0, which is a function of the activation energy ΔE from the most stable trapped configuration of the solid crystal (see Fig. 6.9). Here $\boldsymbol{\xi}$ is assumed to satisfy

$$\langle \xi_\alpha(t) \rangle = 0, \quad \left\langle \xi_\alpha(t) \xi_\beta(t') \right\rangle = 2D\delta_{\alpha,\beta}\delta(t-t'), \tag{6.6}$$

where $\langle \cdots \rangle$ is the average over the distribution of the random variable $\boldsymbol{\xi}$ and D is the diffusion coefficient in the momentum space, which satisfies the fluctuation-dissipation relation $D = \mu F_0 \sqrt{mT/(d+1)}$ in the d-dimensional system with a temperature T. A set of Langevin equations (6.4) and (6.5) can be converted into the Kramers equation [139–143]

$$\frac{\partial f}{\partial t} = \left\{ -\frac{\partial}{\partial \boldsymbol{r}} \cdot \left(\frac{\boldsymbol{p}}{m} + \dot{\gamma} z \hat{\boldsymbol{e}}_y \right) + \frac{\partial}{\partial \boldsymbol{p}} \cdot \left(\dot{\gamma} p_z \hat{\boldsymbol{e}}_y + \mu F_0 \frac{\boldsymbol{p}}{|\boldsymbol{p}|} + D \frac{\partial}{\partial \boldsymbol{p}} \right) \right\} f, \tag{6.7}$$

where $f = f(\boldsymbol{r}, \boldsymbol{p}, t)$ is the probability distribution function of the tracer particle.

If we multiply Eq. (6.7) by p^2 and integrate over $\boldsymbol{p}$, we immediately obtain

$$\frac{\partial}{\partial t} \left\langle p^2 \right\rangle = -\frac{\partial}{\partial \boldsymbol{r}} \cdot \frac{\left\langle p^2 \boldsymbol{p} \right\rangle}{m} - \dot{\gamma} z \frac{\partial}{\partial y} \left\langle p^2 \right\rangle - 2\dot{\gamma} \left\langle p_y p_z \right\rangle - 2\mu F_0 \left\langle p \right\rangle + 2D, \tag{6.8}$$

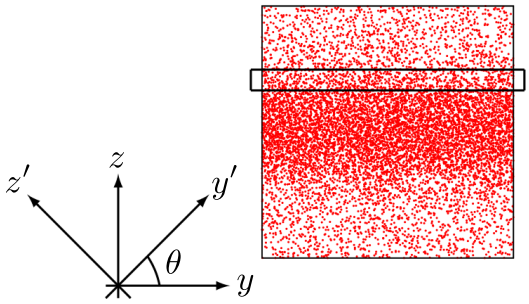

Figure 6.7: (Color online) A snapshot of our simulation for the plate-gases coexistence phase. Solid lines refer to the edges of a bin. The binwise velocity distribution function is calculated in each bin, whose width is $\Delta z = \sigma$. In addition, we introduce a new coordinate (y', z'), and θ, which is the angle between y' and y-direction (in the counterclockwise direction) for later analysis.

where $p = (p_y^2 + p_z^2)^{1/2}$. Because the third term on the right hand side (RHS) of Eq. (6.8) represents the viscous heating which is always positive as shown in Eq. (C.2) and the fourth term is the loss of the energy due to friction, the balance among the third, the fourth and the fifth terms on RHS of Eq. (6.8) produces a steady state. It should be noted that the first and the second terms on RHS do not contribute to the energy balance equation for the whole system.

Here, we only consider the steady distribution, i.e. $\partial f/\partial t = 0$. Thus, Eq. (6.7) is reduced to

$$\frac{\boldsymbol{p}}{m} \cdot \boldsymbol{\nabla} f + \dot{\gamma} z \frac{\partial}{\partial y} f - \dot{\gamma} p_z \frac{\partial}{\partial p_y} f - \mu F_0 \frac{\partial}{\partial \boldsymbol{p}} \cdot \left(\frac{\boldsymbol{p}}{|\boldsymbol{p}|} f \right) - D \Delta_{\boldsymbol{p}} f = 0, \tag{6.9}$$

where $\Delta_{\boldsymbol{p}} = \partial^2/\partial p_y^2 + \partial^2/\partial p_z^2$. If there is neither a shear nor a density gradient, we find that Eq. (6.9) has the steady solution obeying an exponential distribution, i.e. $f(\boldsymbol{p}) = (\kappa^2/2\pi)\exp[-\kappa p]$, where we have introduced $\kappa \equiv \mu F_0/D$. We adopt the perturbative expression for f in terms of $\epsilon \equiv \sigma/\lambda$, which is the ratio of the diameter σ to the interface width λ, and the dimensionless shear rate $\dot{\gamma}^*$ as (see the derivation in Appendix D)

$$f(p, \theta) = f^{(0,0)}(p, \theta) + \epsilon f^{(0,1)}(p, \theta) + \dot{\gamma}^* f^{(1,0)}(p, \theta). \tag{6.10}$$

We also adopt the expansions

$$f^{(i,j)}(p, \theta) = \sum_{n=1}^{\infty} f_n^{(i,j)} \sin(n\theta), \tag{6.11}$$

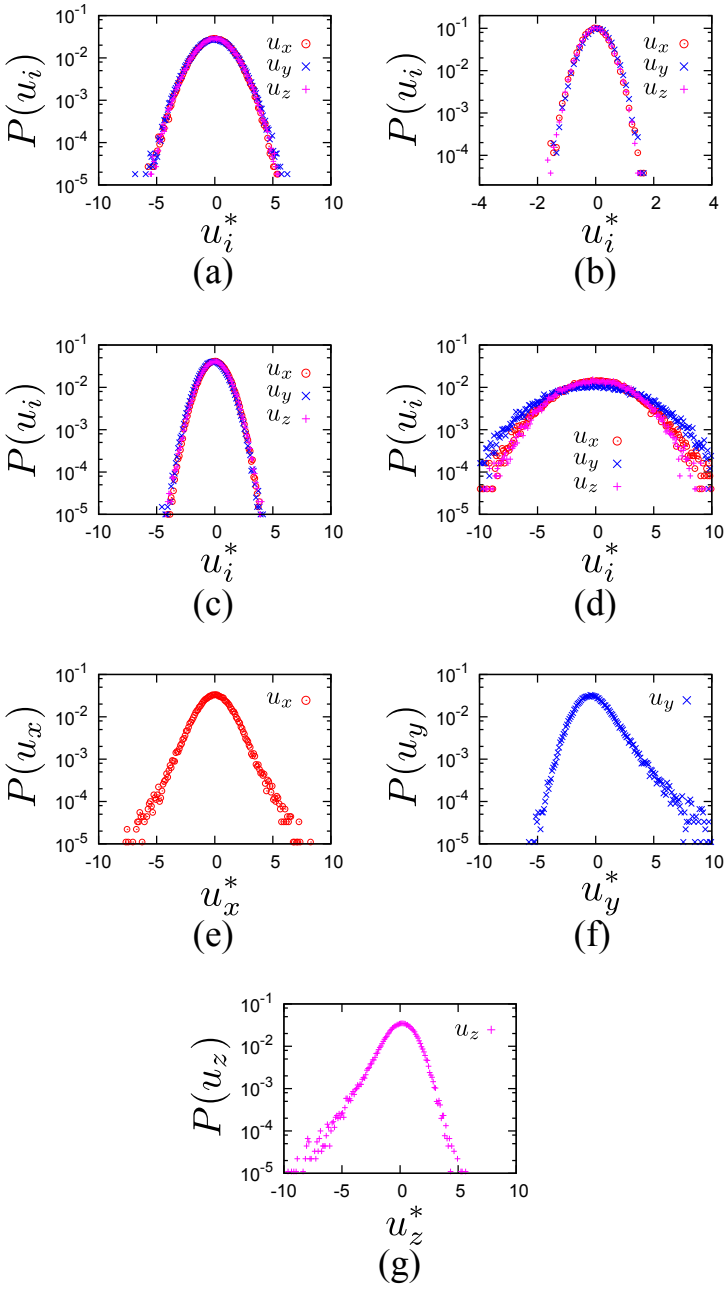

Figure 6.8: (Color online) Velocity distribution functions for various phases: (a) VDFs in the phase Fig. 6.3(a), (b) VDFs in the phase Fig. 6.3(g), (c) VDFs in the dense region of the phase Fig. 6.3(d), (d) VDFs in the dilute region of the phase Fig. 6.3(d), (e) VDF of x-direction in the interface of the phase Fig. 6.3(d), (f) VDF of y-direction in the interface of the phase Fig. 6.3(d), and (g) VDF of z-direction in the interface of the phase Fig. 6.3(d).

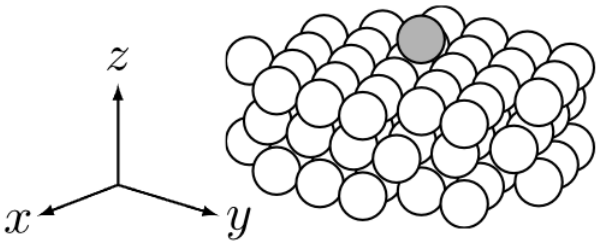

Figure 6.9: A schematic picture of the configuration of a gas particle (gray) and particles in the dense region (white). We assume that the wall particles are composed in a face-centered cubic lattice. We calculate the interaction energy between the gas particle and the wall particles whose distance is less than the cut-off length.

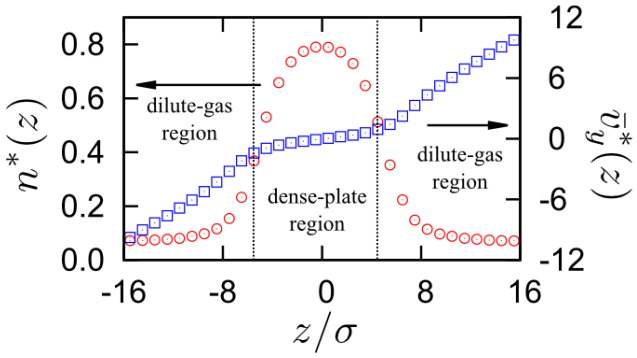

Figure 6.10: (Color online) The density and velocity profiles (in the y-direction) in the plate-gases coexistence phase ($n^* = 0.305$, $\dot{\gamma}^* = 10^{-0.2}$, $\zeta^* = 10^{0.2}$), where $\bar{v}_y^*(z) = \bar{v}_y(z)\sqrt{m/\sigma\varepsilon}$.

with $(i,j)=(0,1)$ and $(1,0)$, where θ is the angle between $\boldsymbol{p}$ and y-axis (in the counterclockwise direction, see Fig. 6.7). Then, we can solve Eq. (6.9) perturbatively as

$$f(p,\theta) = f^{(0,0)}(p) + \epsilon f_1^{(0,1)}(p)\sin\theta + \dot{\gamma}^* f_2^{(1,0)}(p)\sin 2\theta, \tag{6.12}$$

where $f^{(0,0)}$, $f_1^{(0,1)}$ and $f_2^{(1,0)}$ are, respectively, given by

$$f^{(0,0)}(p) = \frac{\kappa^2}{2\pi}\exp\left(-\kappa p\right), \tag{6.13}$$

$$f_1^{(0,1)}(p) = -\frac{A}{6\pi\kappa}p\left(3+\kappa p+\kappa^2 p^2\right)\exp\left(-\kappa p\right), \tag{6.14}$$

$$f_2^{(1,0)}(p) = -\frac{\kappa^2}{8\pi D t_0}p^2\exp\left(-\kappa p\right). \tag{6.15}$$

Here, we have introduced $t_0=(m\sigma^2/\varepsilon)^{1/2}$ and A given by Eq. (D.10). It should be noted that the other terms except for those in Eqs. (6.12)–(6.15) automatically disappear within the linear approximation as in Eq (6.10).

The second, the third and the fourth moments in y' and z'-directions after the rotation by the angle of θ in the counterclockwise direction are, respectively, given by

$$\left\langle p_{y',z'}^2\right\rangle = \frac{3}{\kappa^2}\left(1\mp\frac{5\dot{\gamma}}{2D\kappa^2}\sin 2(\theta-\psi)\right), \tag{6.16}$$

$$\left\langle p_{y'}^3\right\rangle = -\frac{765\epsilon A}{\kappa^6}\sin(\theta-\psi), \tag{6.17}$$

$$\left\langle p_{z'}^3\right\rangle = -\frac{765\epsilon A}{\kappa^6}\cos(\theta-\psi), \tag{6.18}$$

$$\left\langle p_{y',z'}^4\right\rangle = \frac{45}{\kappa^4}\left(1\mp\frac{7\dot{\gamma}}{D\kappa^2}\sin 2(\theta-\psi)\right), \tag{6.19}$$

as shown in Appendix E, where $\left\langle p_{y',z'}^n\right\rangle$ with $n=2$ or 4 represents $\left\langle p_{y'}^n\right\rangle$ for a minus sign and $\left\langle p_{z'}^n\right\rangle$ for a plus sign, respectively. To reproduce the node of the third moment in MD, we phenomenologically introduce the angle ψ and replace θ by $\theta-\psi$ in Eqs. (6.16)–(6.19). Here, we choose $\psi=2\pi/9$ to fit the node position of the third moment. We have not identified the reason why the direction of the node is deviated from the direction at which VDF becomes isotropic.

Now, let us compare Eqs. (6.16)–(6.19) with MD for a set of parameters $(n^*,\dot{\gamma}^*,\zeta^*)=(0.305,10^{-0.2},10^{0.2})$. From the density profile (Fig. 6.10) and the fitting to the second moment and the amplitude of the third moment, we obtain $\epsilon\simeq 0.20$, $\mu\simeq 1.3/\sqrt{m\varepsilon}$, $D=5.2\sqrt{m\varepsilon^3}/\sigma$, and $A\simeq 0.088/m^2\varepsilon^2$. It is surprised that Eqs. (6.16)–(6.19) can approximately reproduce the simulation results as in Fig. 6.11 except for the node positions of the second and the fourth moments.

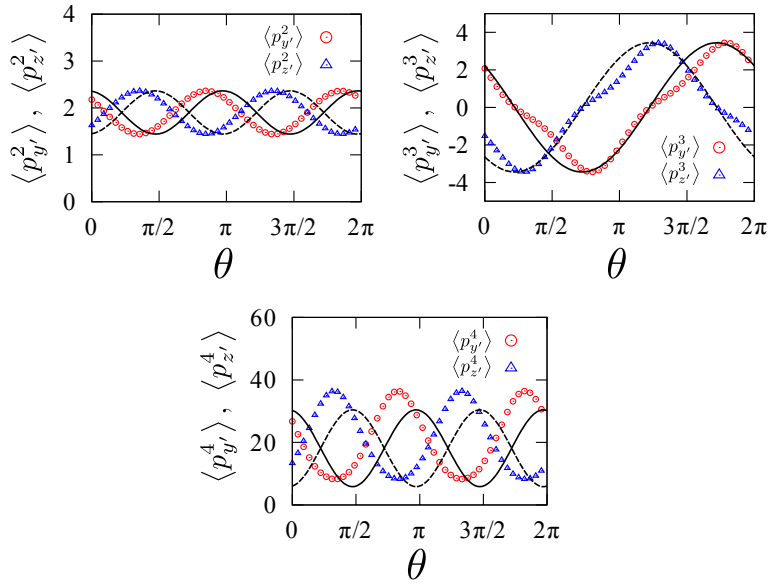

Figure 6.11: (Color online) The second, the third and the fourth moments obtained by MD for $\rho^* = 0.305$, $\dot{\gamma}^* = 10^{-0.2}$, $\zeta^* = 10^{0.2}$ (circle: y'-direction, upper triangle: z'-direction) and those obtained by Eqs. (6.16)–(6.19) (solid line: y'-direction, dashed line: z'-direction).

For the explicit form of VDF, at first, we convert $f(p, \theta)$ to $f(p_y, p_z)$ as in Appendix F:

$$f(p_y, p_z) = \frac{\kappa^2}{2\pi} \exp(-\kappa p) \left[1 + \frac{\epsilon A}{3\kappa^3} \left(3 + \kappa p + \kappa^2 p^2\right) (p_y \sin\psi - p_z \cos\psi) + \frac{\dot{\gamma}}{4D} \left\{ (p_y^2 - p_z^2) \sin 2\psi - 2 p_y p_z \cos 2\psi \right\} \right]. \tag{6.20}$$

We obtain the peculiar velocity distribution function in each direction by integrating Eq. (6.20) with respect to u_z or u_y as

$$P(u_y) = \frac{m\kappa^2}{2\pi} \int_{-\infty}^{\infty} du_z \exp(-m\kappa u) \times \left[1 + \frac{m\epsilon A}{3\kappa^3} \left(3 + m\kappa u + m^2\kappa^2 u^2\right) u_y \sin\psi + \frac{m^2\dot{\gamma}}{4D} (u_y^2 - u_z^2) \sin 2\psi \right], \tag{6.21}$$

$$P(u_z) = \frac{m\kappa^2}{2\pi} \int_{-\infty}^{\infty} du_y \exp\left(-m\kappa u\right) \times \left[1 - \frac{m\epsilon A}{3\kappa^3}\left(3 + m\kappa u + m^2\kappa^2 u^2\right) u_z \cos\psi + \frac{m^2\dot{\gamma}}{4D}(u_y^2 - u_z^2)\sin 2\psi\right], \tag{6.22}$$

where $u = (u_y^2 + u_z^2)^{1/2}$. These expressions semi-quantitatively reproduce VDF observed in our MD as in Fig. 6.12.

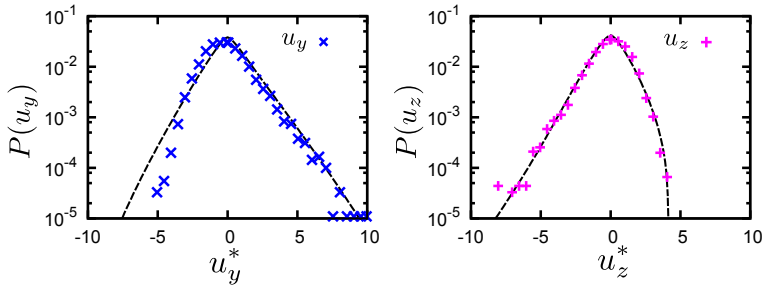

Figure 6.12: (Color online) VDFs in y-direction (left, cross) and z-direction (right, cross) obtained by our MD. The dashed lines in the left and right figures are the results of Eqs. (6.21) and (6.22), respectively.

6.4 Discussion

Let us discuss our results. In Sec. 6.3.1, we do not discuss the time evolution of the granular temperature $T_{\rm g} = (m/3N)\sum_{i=1}^{N} |\boldsymbol{v}_i - \boldsymbol{V}|^2$, where $\boldsymbol{V} = \boldsymbol{V}(\boldsymbol{r}, t)$ is the ensemble average velocity field [144, 145]. The granular temperature abruptly decreases to zero in the cluster phases Fig. 6.3(e)–(i) when a big cluster which absorbs all gas particles appears [146]. To clarify the mechanism of abrupt change of the temperature during clusterings, we will need to study the more detailed dynamics.

In Fig. 6.8, the VDF in a uniformly sheared phase is almost Gaussian. This result seems to be inconsistent with the results for ordinary gases under a uniform shear flow [147], which showed that the VDF differs from Gaussian even in a uniformly sheared phase. In this study, however, we only restrict our interest to small inelastic and weakly sheared cases. This situation validates small deviation from Gaussian.

6.5 Conclusion

We studied cohesive fine powders under a plane shear by controlling the density, the dimensionless shear rate and the dissipation rate. Depending on

these parameters, we found the existence of various distinct steady phases as in Fig. 6.3, and we have drawn the phase diagrams for several densities as in Fig. 6.4. In addition, the shape of clusters depends on the initial condition of velocities of particles as in Fig. 6.5, when the dissipation is strong. We also found that there is a quasi particle-hole symmetry for the shape of clusters in steady states with respect to the density.

We found that the velocity distribution functions near the interface between the dense region and the gas-like dilute region in the dense-plate coexistence phase deviate from the Gaussian as in Fig. 6.8. Introducing a stochastic model and its corresponding the Kramers equation (6.7), we obtain its perturbative VDFs as in Eqs. (6.21) and (6.22), which reproduce the semi-quantitative behavior of VDF observed in MD as in Fig. 6.12. This result suggests that the motion of a gas particle near the interface is subjected to Coulombic friction force whose origin is the activation energy in the dense region.

Chapter 7

Kinetic theory for dilute cohesive granular gases with a square well potential

Abstract

We develop the kinetic theory of dilute cohesive granular gases in which the attractive part is described by a square well potential. We derive the hydrodynamic equations from the kinetic theory with the microscopic expressions for the dissipation rate and the transport coefficients. We check the validity of our theory by performing the DSMC.

7.1 Introduction

As stated in introduction, chapters 3 and 4 as well as the previous chapter 6, the physics of cohesive granular materials is an important research subject. On the other hand, we do not have any systematic theoretical analysis starting from a microscopic basic equation in describing such systems even for our previous studies so far. Therefore, we need to develop the kinetic theory relying on the inelastic Boltzmann equation to describe the hydrodynamic behavior of cohesive dilute granular gases. In this chapter, we analyze modified Haff's law and derive the transport coefficients for the dilute cohesive granular gases in freely cooling processes. For this purpose, we extend the kinetic theory for the inelastic hard core system to the nearly elastic granular gases having the square well potential.

The organization of this chapter is as follows. In the next section, we evaluate the scattering angle for a two-body collision process as a function of the impact parameter and the relative velocity of the colliding pair of particles by solving the Newton equation. In Sec. 7.3 we extend the kinetic theory for hard core granular gases to the gases having the square well potential to

derive the transport coefficients in a set of the hydrodynamic equations. In Sec. 7.4, we compare them with those obtained by the DSMC. In Secs. 7.5 and 7.6, we discuss and summarize our results, respectively. In Appendix G, we explain collision geometries for core collisions and grazing collisions to determine the velocity change during collisions in details. In Appendix H, we briefly explain the procedure to obtain the transport coefficients by using the Chapman-Enskog theory. In Appendices I and J, we calculate the second moment of the collision integral and two Sonine coefficients in terms of the kinetic theory, respectively. In Appendix K, we calculate the explicit expressions of the transport coefficients in the high and low temperature limit.

7.2 Scattering angle for the square well potential

Let us calculate the scattering angle for monodisperse smooth inelastic hard spheres having the square well potential whose mass is m [39, 74, 148–151]. Here, the hard core potential associated with the square well attractive part for the relative distance r between two spheres is given by

$$U(r) = \begin{cases} \infty & (r \le d) \\ -\varepsilon & (d < r \le \lambda d) \\ 0 & (r > \lambda d) \end{cases}, \tag{7.1}$$

where ε and λ are, respectively, the well depth and the well width ratio. We assume that collisions are inelastic only if particles hit the core ($r = d$) characterized by the restitution coefficient e.

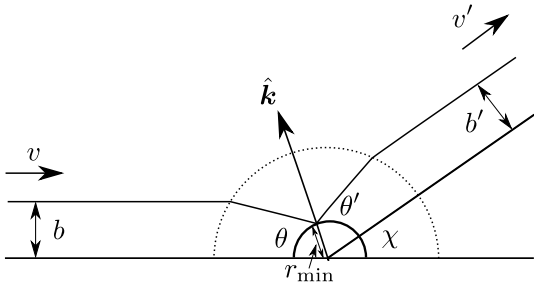

Figure 7.1: A schematic view of a collision process. The dotted line represents the outer edge of the attractive potential.

Let us consider a scattering process in which two particles approach from far away with relative velocity $\boldsymbol{v}$ and leave with the relative velocity $\boldsymbol{v}'$ after the scattering as depicted by Fig. 7.1 in the frame that the target is stationary. The incident angle θ between $\boldsymbol{v}$ and the normal unit vector $\hat{\boldsymbol{k}}$

at the closest distance $r = r_{\rm min}$ between colliding particles is given by

$$\theta = b \int_0^{u_0} \frac{du}{\sqrt{1 - b^2u^2 - \frac{4}{mv^2}U(1/u)}}, \tag{7.2}$$

where $u \equiv 1/r$. Here, $u_0 \equiv 1/r_{\rm min}$ is the smaller one between $1/d$ and the positive solution that the denominator of Eq. (7.2) is equal to zero [152,153], and $\hat{\boldsymbol{k}} = \boldsymbol{r}_{12}/r_{12}$ is a unit vector parallel to $\boldsymbol{r}_{12} = \boldsymbol{r}_1 - \boldsymbol{r}_2$ with the positions $\boldsymbol{r}_1$ and $\boldsymbol{r}_2$ for particles 1 and 2, and $r_{12} = |\boldsymbol{r}_{12}|$. We have also introduced the impact parameter b for the incident process. Because the scattering is inelastic, in general, the impact parameter b' after the scattering and the angle θ' between $\hat{\boldsymbol{k}}$ and $\boldsymbol{v}'$ differ from b and θ, respectively (Fig. 7.1). Let us consider the case for $b > \lambda d$, where Eq. (7.2) reduces to

$$\theta = b \int_0^{1/b} \frac{du}{\sqrt{1 - b^2u^2}} = \frac{\pi}{2} \tag{7.3}$$

under the condition $u_0 = 1/d$. Because the particles do not collide, $\theta' = \theta$, the scattering angle χ is given by

$$\chi = \pi - 2\theta = 0, \quad \sin\frac{\chi}{2} = 0. \tag{7.4}$$

Next, we consider the case for $b \leq \lambda d$ in which Eq. (7.2) can be rewritten as

$$\begin{aligned}\theta =& b \int_0^{1/\lambda d} \frac{du}{\sqrt{1 - b^2u^2}} + b \int_{1/\lambda d}^{u_0} \frac{du}{\sqrt{1 - b^2u^2 + \frac{4\varepsilon}{mv^2}}} \\ =& \arcsin\left(\frac{b}{\lambda d}\right) + b \int_{1/\lambda d}^{u_0} \frac{du}{\sqrt{\nu^2 - b^2u^2}},\end{aligned} \tag{7.5}$$

where we have introduced ν as

$$\nu \equiv \sqrt{1 + \frac{4\varepsilon}{mv^2}}, \tag{7.6}$$

and $u_0 = \min(1/d, \nu/b)$ with the introduction of a function $\min(x, y)$ to select the smaller one between x and y. We note that ν is related to the refractive index [152, 153]. For $b \geq \nu d$, u_0 is given by $u_0 = \nu/b$ and this collision is called a grazing collision [148–150]. From Eq. (7.5), we rewrite θ as

$$\theta = \frac{\pi}{2} + \arcsin\left(\frac{b}{\lambda d}\right) - \arcsin\left(\frac{b}{\nu\lambda d}\right). \tag{7.7}$$

Because the particle does not hit the core, $\theta' = \theta$, the scattering angle χ is given by

$$\chi = \chi^{(0)} = \pi - 2\theta = 2\arcsin\left(\frac{b}{\nu\lambda d}\right) - 2\arcsin\left(\frac{b}{\lambda d}\right). \tag{7.8}$$

Equation (7.8), thus, can be rewritten as

$$\sin\frac{\chi}{2} = \sin\left[\arcsin\left(\frac{b}{\nu\lambda d}\right) - \arcsin\left(\frac{b}{\lambda d}\right)\right]. \tag{7.9}$$

Note that this collision does not exist for $\lambda < \nu$.

Table 7.1: Parameters corresponding to Fig. 7.2.

	(a) hard core (inelastic)	(b) grazing (elastic)	(c) no-collision
b	$b/d < \min(\nu, \lambda)$	$\min(\nu, \lambda) \le b/d < \lambda$	$b/d \ge \lambda$
$\sin\frac{\chi}{2}$	Eq.(7.16)	Eq.(7.9)	Eq.(7.4)

For $b < \nu d$, u_0 is given by $u_0 = 1/d$, and then the particles hit the core of the potential. From Eq. (7.5), we obtain θ:

$$\theta = \arcsin\left(\frac{b}{\lambda d}\right) + \arcsin\left(\frac{b}{\nu d}\right) - \arcsin\left(\frac{b}{\nu\lambda d}\right). \tag{7.10}$$

In this case, the collision is inelastic, and thus, θ' is not equal to θ. From the conservation of the angular momentum $bv = b'v'$, θ' is given by

$$\begin{aligned}\theta' &= \arcsin\left(\frac{b'}{\lambda d}\right) + \arcsin\left(\frac{b'}{\nu' d}\right) - \arcsin\left(\frac{b'}{\nu'\lambda d}\right) \\ &= \arcsin\left(\frac{b}{\lambda d}\right) + \arcsin\left(\frac{b}{\nu d}\right) - \arcsin\left(\frac{b}{\nu\lambda d}\right) \\ &\quad + \epsilon\left(\frac{b\nu^2}{\sqrt{\lambda^2 d^2 - b^2}} + \frac{b}{\sqrt{\nu^2 d^2 b^2}} - \frac{b}{\sqrt{\lambda^2\nu^2 d^2 - b^2}}\right)\cos^2\Theta + \mathcal{O}(\epsilon^2),\end{aligned} \tag{7.11}$$

where we have introduced Θ as

$$\cos\Theta \equiv \frac{\sqrt{\nu^2 d^2 - b^2}}{\nu d} \tag{7.12}$$

(see Appendix G for the derivation) and $\epsilon \equiv 1 - e$. Thus, we obtain the scattering angle χ as

$$\chi = \pi - \theta - \theta' = \chi^{(0)} + \epsilon\chi^{(1)} + \mathcal{O}(\epsilon^2) \tag{7.13}$$

with

$$\chi^{(0)} = \pi - 2\arcsin\left(\frac{b}{\lambda d}\right) - 2\arcsin\left(\frac{b}{\nu d}\right) + 2\arcsin\left(\frac{b}{\nu\lambda d}\right), \tag{7.14}$$

$$\chi^{(1)} = -\left[\frac{b\nu^2}{\sqrt{\lambda^2 d^2 - b^2}} + \frac{b}{\sqrt{\nu^2 d^2 - b^2}} - \frac{b}{\sqrt{\lambda^2\nu^2 d^2 - b^2}}\right]\cos^2\Theta. \tag{7.15}$$

We can rewrite Eq. (7.13) as

$$\sin\frac{\chi}{2} = \sin\frac{\chi^{(0)}}{2} + \frac{1}{2}\epsilon\chi^{(1)}\cos\frac{\chi^{(0)}}{2} + \mathcal{O}(\epsilon^2). \tag{7.16}$$

These results are consistent with the previous study in the elastic limit ($e \to 1$) [148]. We regard the grazing collision as a combination of (ii) entering and (iii) leaving processes from the well [148]. We ignore the trapping process by the attractive potential in the elastic limit (i. e. $\epsilon \to 0$) because colliding particles against hard cores have positive energies and the most of rebounding particles have still positive energies. In other words, if the trapping process is relevant, the inelastic Boltzmann equation is no longer valid. Thus, through the analysis of the inelastic Boltzmann equation we will discuss whether it can be used even for weakly inelastic cohesive granular gases. We summarize the above results in Fig. 7.2 and Table 7.1.

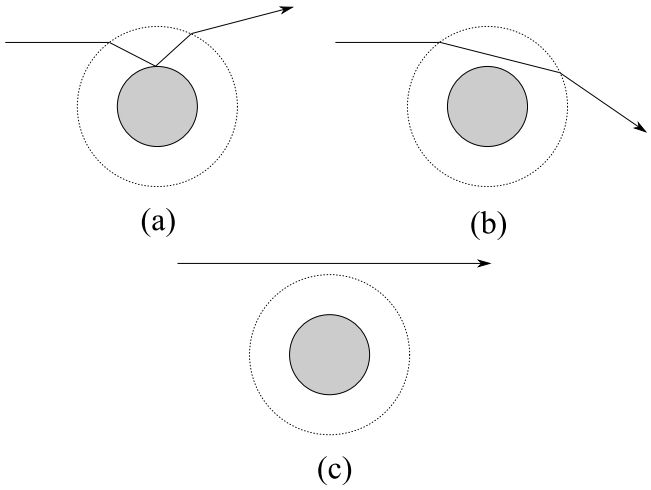

Figure 7.2: Schematic views of dynamic processes between two adjacent particles. There exist three types: (a) collisions via the hard core potential (inelastic), (b) grazing collisions (elastic), and (c) no-collisions.

7.3 kinetic theory and hydrodynamic equations

If we consider a dilute and weakly inelastic homogeneous granular gas, we may use the inelastic Boltzmann equation

$$\left(\frac{\partial}{\partial t} + \boldsymbol{v}_1 \cdot \boldsymbol{\nabla}\right) f(\boldsymbol{r}, \boldsymbol{v}_1, t) = I(f, f), \tag{7.17}$$

where $I(f,f)$ is the collision integral

$$
\begin{aligned}
I(f,f) = &\int d\boldsymbol{v}_2 \int d\hat{\boldsymbol{k}}\Theta(\min(\lambda,\nu)-\tilde{b})|\boldsymbol{v}_{12}\cdot\hat{\boldsymbol{k}}| \\
&\times \left[\chi_e \sigma(\chi, v_{12}'') f(\boldsymbol{r},\boldsymbol{v}_1'',t) f(\boldsymbol{r},\boldsymbol{v}_2'',t) - \sigma(\chi,v_{12}) f(\boldsymbol{r},\boldsymbol{v}_1,t) f(\boldsymbol{r},\boldsymbol{v}_2,t)\right] \\
&+ \int d\boldsymbol{v}_2 \int d\hat{\boldsymbol{k}}\Theta(\tilde{b}-\min(\lambda,\nu))|\boldsymbol{v}_{12}\cdot\hat{\boldsymbol{k}}| \\
&\times \left[\sigma(\chi, v_{12}'') f(\boldsymbol{r},\boldsymbol{v}_1'',t) f(\boldsymbol{r},\boldsymbol{v}_2'',t) - \sigma(\chi,v_{12}) f(\boldsymbol{r},\boldsymbol{v}_1,t) f(\boldsymbol{r},\boldsymbol{v}_2,t)\right].
\end{aligned}
\tag{7.18}
$$

Here we have introduced the step function $\Theta(x) = 1$ for $x > 0$ and $\Theta(x) = 0$ otherwise. Here $v_{12} = |\boldsymbol{v}_{12}|$ with $\boldsymbol{v}_{12} = \boldsymbol{v}_1 - \boldsymbol{v}_2$ with the velocity $\boldsymbol{v}_i$ $(i = 1, 2)$ for i-th particle, $\sigma(\chi, v_{12})$ is the collision cross section between i-th and j-th particles, and $\tilde{b} = b/d$ is a dimensionless collision parameter. The factor χ_e is related to the Jacobian of the transformation between pre-collisional velocities $\boldsymbol{v}_1'', \boldsymbol{v}_2''$ and the velocities after collision $\boldsymbol{v}_1, \boldsymbol{v}_2$ [38, 45, 46, 67]. The first and second terms on the right-hand-side of Eq. (7.18) correspond to inelastic and elastic collisions, respectively. For the sake of later discussion, we explicitly write the relationship between $(\boldsymbol{v}_1'', \boldsymbol{v}_2'')$ and $(\boldsymbol{v}_1, \boldsymbol{v}_2)$

$$
\boldsymbol{v}_1 = \boldsymbol{v}_1'' + \frac{1}{2}\Delta\boldsymbol{v}, \quad \boldsymbol{v}_2 = \boldsymbol{v}_2'' - \frac{1}{2}\Delta\boldsymbol{v}, \tag{7.19}
$$

with

$$
\Delta\boldsymbol{v} = -2\left(1 - \frac{1}{2}\epsilon\nu^2\frac{\cos^2\Theta}{\cos^2\theta}\right)(\boldsymbol{v}_{12}''\cdot\hat{\boldsymbol{k}})\hat{\boldsymbol{k}} + \mathcal{O}(\epsilon^2) \tag{7.20}
$$

for inelastic hard core collisions and

$$
\Delta\boldsymbol{v} = -2(\boldsymbol{v}_{12}''\cdot\hat{\boldsymbol{k}})\hat{\boldsymbol{k}} \tag{7.21}
$$

for elastic grazing collisions (see Appendix G for the derivation). From Eq. (7.20), the explicit form of the factor χ_e is given by

$$
\chi_e = 1 + 2\epsilon\nu^2\frac{\cos^2\Theta}{\cos^2\theta} + \mathcal{O}(\epsilon^2) \tag{7.22}
$$

for inelastic hard core collisions. It should be noted that Eq. (7.22) is consistent with $1/e^2$ for inelastic hard core potential [38, 45, 46, 67], because this can be expanded as $1/e^2 = 1 + 2\epsilon + \mathcal{O}(\epsilon^2)$ in the nearly elastic limit and ν and Θ reduce to $\nu \to 1$ and $\Theta \to \theta$, respectively, in the hard core limit from Eqs. (7.6) and (7.12).

7.3.1 Homogeneous freely cooling

In this subsection, let us determine the velocity distribution function $f(\boldsymbol{v}, t)$ in freely cooling granular gases based on the Boltzmann equation (7.17).

First, we expand the distribution function in terms of Sonine polynomials [**?**, 38, 45, 46, 67] as

$$f^{(0)}(\boldsymbol{v},t) = f_{\rm M}(V)\left[1+\sum_{\ell=1}^{\infty} a_\ell S_\ell\left(\frac{mV^2}{2T(t)}\right)\right], \tag{7.23}$$

where $V = |\boldsymbol{V}| = |\boldsymbol{v}-\boldsymbol{U}|$ is the local velocity fluctuation from the flow velocity $\boldsymbol{U}(\boldsymbol{r},t)$, $f_{\rm M}(V) = n(m/2\pi T)^{3/2}\exp(-mV^2/2T)$ is the Maxwellian at the temperature T and the number density n, and $S_\ell(x) \equiv S_\ell^{(1/2)}(x)$ is the Sonine polynomial:

$$S_\ell^{(j)}(x) = \sum_{k=0}^{\ell} \frac{(-1)^k\Gamma(j+\ell+1)}{\Gamma(j+k+1)(\ell-k)!k!}x^k \tag{7.24}$$

with the Gamma function $\Gamma(x)$. The time evolution of the granular temperature, obtained by the product of the Boltzmann equation with $mv_1^2/2$ and integrating over $\boldsymbol{v}_1$, is written as

$$\frac{dT}{dt} = -\zeta^{(0)}T, \tag{7.25}$$

where we have introduced the cooling rate for the homogeneous gas

$$\zeta^{(0)} = \frac{2}{3}nd^2\sqrt{\frac{2T}{m}}\mathcal{M}_2. \tag{7.26}$$

Here, $\mathcal{M}_2$ is the second moment of the dimensionless collision integral

$$\mathcal{M}_2 = -\int d\boldsymbol{c}_1 c_1^2 \tilde{I}(\tilde{f}^{(0)},\tilde{f}^{(0)}), \tag{7.27}$$

where we have introduced the dimensionless velocity $\boldsymbol{c}_1 = \boldsymbol{v}_1/v_T(t)$ with the thermal velocity $v_T(t) = \sqrt{2T(t)/m}$, the dimensionless collision integral $\tilde{I}(\tilde{f}^{(0)},\tilde{f}^{(0)}) = (v_T^2/n^2d^2)I(f^{(0)},f^{(0)})$, and the dimensionless distribution function $\tilde{f}^{(0)}(\boldsymbol{c}) = (v_T^3/n)f^{(0)}(\boldsymbol{v},t)$. After some manipulation of Eq. (7.27), $\mathcal{M}_2$ can be rewritten as [31, 46]

$$\begin{aligned}\mathcal{M}_2 = -\frac{1}{2}\int d\boldsymbol{c}_1\int d\boldsymbol{c}_2\int d\hat{\boldsymbol{k}}|\boldsymbol{c}_{12}\cdot\hat{\boldsymbol{k}}|\tilde{\sigma}(\chi,c_{12}) \\ \times\tilde{f}^{(0)}(\boldsymbol{c}_1)\tilde{f}^{(0)}(\boldsymbol{c}_2)\Delta[c_1^2+c_2^2]\end{aligned} \tag{7.28}$$

with $\tilde{\sigma}(\chi,c_{12}) = \sigma(\chi,v_{12})/d^2$ and $\phi(c) = \pi^{-3/2}\exp(-c^2)$, and $\Delta\psi(\boldsymbol{c}_i) \equiv \psi(\boldsymbol{c}_i') - \psi(\boldsymbol{c}_i)$. It should be noted that the density keeps constant and the flow velocity is zero in the homogeneous state.

7.3.2 Hydrodynamic equations

In this subsection, let us derive the transport coefficients which appear in a set of hydrodynamic equations. Multiplying the Boltzmann equation (7.17) by 1, $\boldsymbol{v}_1$ and $mv_1^2/2$ and integrating over $\boldsymbol{v}_1$, we obtain the hydrodynamic equations

$$\frac{\partial n}{\partial t} + \boldsymbol{\nabla} \cdot (n\boldsymbol{U}) = 0, \tag{7.29}$$

$$\frac{\partial \boldsymbol{U}}{\partial t} + \boldsymbol{U} \cdot \boldsymbol{\nabla}\boldsymbol{U} + \frac{1}{mn}\boldsymbol{\nabla} \cdot P = 0, \tag{7.30}$$

$$\frac{\partial T}{\partial t} + \boldsymbol{U} \cdot \boldsymbol{\nabla} T + \frac{2}{3n}\left(P : \boldsymbol{\nabla}\boldsymbol{U} + \boldsymbol{\nabla} \cdot \boldsymbol{q}\right) + \zeta T = 0, \tag{7.31}$$

where $n(\boldsymbol{r}, t)$ is the density field, $\boldsymbol{U}(\boldsymbol{r}, t)$ is the flow velocity, and $T(\boldsymbol{r}, t)$ is the granular temperature. The pressure tensor P, the heat flux $\boldsymbol{q}$, and the cooling rate ζ are, respectively, defined as

$$P_{ij} \equiv \int d\boldsymbol{v} D_{ij}(\boldsymbol{V}) f(\boldsymbol{r}, \boldsymbol{v}, t) + nT\delta_{ij}, \tag{7.32}$$

$$\boldsymbol{q} \equiv \int d\boldsymbol{v} \boldsymbol{S}(\boldsymbol{V}) f(\boldsymbol{r}, \boldsymbol{v}, t), \tag{7.33}$$

$$\zeta \equiv -\frac{m}{3nT}\int d\boldsymbol{v} v^2 I(f, f), \tag{7.34}$$

where $D_{ij}(\boldsymbol{V}) \equiv m(V_i V_j - V^2\delta_{ij}/3)$ and $\boldsymbol{S}(\boldsymbol{V}) \equiv (mV^2/2 - 5T/2)\boldsymbol{V}$. We adopt the constitutive equations at the Navier-Stokes order

$$P = p\delta_{ij} - \eta\left(\nabla_i U_j + \nabla_j U_i - \frac{2}{3}\delta_{ij}\boldsymbol{\nabla} \cdot \boldsymbol{U}\right), \tag{7.35}$$

$$\boldsymbol{q} = -\kappa\boldsymbol{\nabla} T - \mu\boldsymbol{\nabla} n, \tag{7.36}$$

where p is the hydrostatic pressure, η is the shear viscosity, κ is the thermal conductivity, and μ is the coefficient proportional to the density gradient.

To obtain the transport coefficients, we adopt the Chapman-Enskog method [39, 46, 67]. Here, we expand the distribution function around Eq. (7.23) as

$$f = f^{(0)} + \delta f^{(1)} + \cdots \tag{7.37}$$

by a small parameter δ corresponding to the gradients of the fields. Similarly, the time derivative of the distribution function is expanded as

$$\frac{\partial}{\partial t} = \frac{\partial^{(0)}}{\partial t} + \delta\frac{\partial^{(1)}}{\partial t} + \cdots. \tag{7.38}$$

We, thus, rewrite the Boltzmann equation (7.17) as

$$\begin{aligned}&\left(\frac{\partial^{(0)}}{\partial t} + \delta\frac{\partial^{(1)}}{\partial t} + \cdots + \delta\boldsymbol{v}_1 \cdot \boldsymbol{\nabla}\right)\left(f^{(0)} + \delta f^{(1)} + \cdots\right)\\ &= I\left[\left(f^{(0)} + \delta f^{(1)} + \cdots\right), \left(f^{(0)} + \delta f^{(1)} + \cdots\right)\right].\end{aligned} \tag{7.39}$$

The equation at the zeroth order of Eq. (7.39) is reduced to

$$\frac{\partial^{(0)}}{\partial t} f^{(0)} = I\left(f^{(0)}, f^{(0)}\right). \tag{7.40}$$

From Eqs (7.29)–(7.31), the zeroth order hydrodynamic equations are, respectively, given by

$$\frac{\partial^{(0)}}{\partial t} n = 0, \quad \frac{\partial^{(0)}}{\partial t} \boldsymbol{U} = 0, \quad \frac{\partial^{(0)}}{\partial t} T = -\zeta^{(0)} T, \tag{7.41}$$

which are equivalent to those obtained in the previous subsection for the homogeneous cooling state. The zeroth order of the pressure tensor and the heat flux are, respectively, given by

$$P_{ij}^{(0)} = nT\delta_{ij}, \quad \boldsymbol{q}^{(0)} = 0. \tag{7.42}$$

The first-order Boltzmann equation becomes

$$\begin{aligned} &\frac{\partial^{(0)}}{\partial t} f^{(1)} + \left(\frac{\partial^{(1)}}{\partial t} + \boldsymbol{v}_1 \cdot \boldsymbol{\nabla}\right) f^{(0)} \\ &= I\left(f^{(0)}, f^{(1)}\right) + I\left(f^{(1)}, f^{(0)}\right). \end{aligned} \tag{7.43}$$

The corresponding first-order hydrodynamic equations are, respectively, given by

$$\begin{aligned} \frac{\partial^{(1)}}{\partial t} n &= -\boldsymbol{\nabla} \cdot (n\boldsymbol{U}), \\ \frac{\partial^{(1)}}{\partial t} \boldsymbol{U} &= -\boldsymbol{U} \cdot \boldsymbol{\nabla} \boldsymbol{U} - \frac{1}{mn} \boldsymbol{\nabla}(nT), \\ \frac{\partial^{(1)}}{\partial t} T &= -\boldsymbol{U} \cdot \boldsymbol{\nabla} T - \frac{2}{3} T \boldsymbol{\nabla} \cdot \boldsymbol{U} - \zeta^{(1)} T, \end{aligned} \tag{7.44}$$

where the first-order dissipation rate $\zeta^{(1)}$ is defined by

$$\zeta^{(1)} = -\frac{2m}{3nT} \int d\boldsymbol{v} v^2 I\left(f^{(0)}, f^{(1)}\right). \tag{7.45}$$

We note that $\zeta^{(1)}$ becomes zero because of the parity of the integral (7.45) [44, 46, 67]. We assume that the distribution function $f^{(0)}$ depends on time and space only via its moments: the density n, the average velocity $\boldsymbol{U}$ and the temperature T as $f^{(0)} = f^{(0)}[\boldsymbol{v}|n, \boldsymbol{U}, T]$. Then we can rewrite the first-order equation (7.43) as

$$\begin{aligned} &\frac{\partial^{(0)} f^{(1)}}{\partial t} + J^{(1)}\left(f^{(0)}, f^{(1)}\right) - \zeta^{(1)} T \frac{\partial f^{(0)}}{\partial T} \\ &= f^{(0)} \left(\boldsymbol{\nabla} \cdot \boldsymbol{U} - \boldsymbol{V} \cdot \boldsymbol{\nabla} n\right) + \frac{\partial f^{(0)}}{\partial T} \left(\frac{2}{3} T \boldsymbol{\nabla} \cdot \boldsymbol{U} - \boldsymbol{V} \cdot \boldsymbol{\nabla} T\right) \\ &\quad + \frac{\partial f^{(0)}}{\partial \boldsymbol{V}} \cdot \left((\boldsymbol{V} \cdot \boldsymbol{\nabla}) \boldsymbol{U} - \frac{1}{mn} \boldsymbol{\nabla} P\right), \end{aligned} \tag{7.46}$$

where

$$J^{(1)}\left(f^{(0)},f^{(1)}\right)=-I\left(f^{(0)},f^{(1)}\right)-I\left(f^{(1)},f^{(0)}\right). \tag{7.47}$$

From the form of the first-order equation (7.43), the solution of this equation is expected to have the form

$$f^{(1)}=\mathcal{A}\cdot\boldsymbol{\nabla}\log T+\mathcal{B}\cdot\boldsymbol{\nabla}\log n+\mathcal{C}_{ij}\nabla_j U_i, \tag{7.48}$$

where the explicit forms of the coefficients $\mathcal{A}$, $\mathcal{B}$, and $\mathcal{C}_{ij}$ are given in Appendix H as Eqs. (H.19), (H.20), and (H.12), respectively. The pressure tensor and the heat flux can be written as

$$P_{ij}^{(1)}=-\eta\left(\nabla_i U_j+\nabla_j U_i-\frac{2}{3}\delta_{ij}\boldsymbol{\nabla}\cdot\boldsymbol{U}\right), \tag{7.49}$$

$$\boldsymbol{q}^{(1)}=-\kappa\boldsymbol{\nabla}T-\mu\boldsymbol{\nabla}n. \tag{7.50}$$

Substituting $f=f^{(0)}+f^{(1)}$ and Eq. (7.49) into Eq. (7.32), we obtain the differential equation for the shear viscosity η with respect to T as

$$-\zeta^{(0)}T\frac{\partial\eta}{\partial T}-\frac{2}{5}nd^2\sqrt{\frac{2T}{m}}\Omega_\eta^e\eta=nT, \tag{7.51}$$

where Ω_η^e is given by

$$\begin{aligned}\Omega_\eta^e=&\int d\boldsymbol{c}_1\int d\boldsymbol{c}_2\int d\hat{\boldsymbol{k}}\tilde{\sigma}(\chi,c_{12})(\boldsymbol{c}_{12}\cdot\hat{\boldsymbol{k}})\phi(c_1)\phi(c_2)\\&\times\left[1+\sum_{\ell=1}^{\infty}a_\ell S_\ell(c_1^2)\right]\tilde{D}_{ij}(\boldsymbol{c}_2)\Delta\left[\tilde{D}_{ij}(\boldsymbol{c}_1)+\tilde{D}_{ij}(\boldsymbol{c}_2)\right]\end{aligned} \tag{7.52}$$

with $\tilde{D}_{ij}=D_{ij}/\varepsilon$. Similarly, substituting Eq. (7.50) into Eq. (7.33), we obtain the differential equations for the thermal conductivity κ and the coefficient μ with respect to T as

$$\frac{\partial}{\partial T}\left(3\zeta^{(0)}\kappa T\right)+\frac{4}{5}\kappa nd^2\sqrt{\frac{2T}{m}}\Omega_\kappa^e=-\frac{15}{2}\frac{nT}{m}\left(1+2a_2\right), \tag{7.53}$$

and

$$-3n\zeta^{(0)}\frac{\partial\mu}{\partial T}-3\kappa\zeta^{(0)}-\frac{4}{5}n^2d^2\sqrt{\frac{2}{mT}}\Omega_\kappa^e\mu=a_2\frac{15}{2}\frac{nT}{m}, \tag{7.54}$$

respectively, where Ω_κ^e is given by

$$\begin{aligned}\Omega_\kappa^e=&\int d\boldsymbol{c}_1\int d\boldsymbol{c}_2\int d\hat{\boldsymbol{k}}\tilde{\sigma}(\chi,c_{12})(\boldsymbol{c}_{12}\cdot\hat{\boldsymbol{k}})\phi(c_1)\phi(c_2)\\&\times\left[1+\sum_{\ell=1}^{\infty}a_\ell S_\ell(c_1^2)\right]\tilde{\boldsymbol{S}}(\boldsymbol{c}_2)\cdot\Delta\left[\tilde{\boldsymbol{S}}(\boldsymbol{c}_1)+\tilde{\boldsymbol{S}}(\boldsymbol{c}_2)\right]\end{aligned} \tag{7.55}$$

with $\tilde{\boldsymbol{S}}=\boldsymbol{S}\sqrt{m/\varepsilon^3}$. It should be noted that Eqs. (7.51), (7.53), and (7.54) are consistent with those in the previous study in the hard core limit [46].

7.3.3 Transport coefficients for the granular gases having the square well potential

In the previous subsection, we have presented the general framework for the second moment (7.28) and the differential equations of the transport coefficients (7.51), (7.53), and (7.54) in dilute granular cohesive granular gases without specification of mutual interactions between grains. In this subsection, let us derive the explicit forms of them for the square well potential outside and the hard core potential inside. Here, we assume that the zero-th order distribution function can be well reproduced by the truncation up to the third order Sonine polynomials [31, 46, 68–70] as

$$\tilde{f}^{(0)}(\boldsymbol{c}) = \phi(c)\left[1 + a_2 S_2(c^2) + a_3 S_3(c^2)\right], \tag{7.56}$$

where a_1 is automatically zero because the first order moment is absorbed in the definition of the zeroth velocity distribution function. In this paper, we only consider the elastic limit $\epsilon \to 0$. In addition, the coefficients a_2 and a_3 can be, respectively, written as the series of ϵ as shown in Appendix I,

$$\begin{cases} a_2 = a_2^{(0)} + \epsilon a_2^{(1)} + \mathcal{O}(\epsilon^2) \\ a_3 = a_3^{(0)} + \epsilon a_3^{(1)} + \mathcal{O}(\epsilon^2) \end{cases}, \tag{7.57}$$

where the coefficients are given by

$$a_2^{(0)} = a_3^{(0)} = 0, \quad a_2^{(1)} = \frac{N_1}{D}, \quad a_3^{(1)} = \frac{N_2}{D} \tag{7.58}$$

with

$$
\begin{aligned}
N_2 =& 2\int_0^\infty dc_{12}\int_0^{\tilde{b}_{\max}} d\tilde{b}\,\tilde{b}(\nu^2-\tilde{b}^2)c_{12}^5(5-c_{12}^2)\exp\left(-\frac{1}{2}c_{12}^2\right)\\
&\times\int_0^\infty dc'_{12}\int_0^\lambda d\tilde{b}'\,\tilde{b}'c_{12}'^7(35-c_{12}'^4)\sin^2\chi^{(0)\prime}\exp\left(-\frac{1}{2}c_{12}'^2\right)\\
&-\int_0^\infty dc_{12}\int_0^{\tilde{b}_{\max}} d\tilde{b}\,\tilde{b}(\nu^2-\tilde{b}^2)c_{12}^5(105-14c_{12}^2-c_{12}^4)\exp\left(-\frac{1}{2}c_{12}^2\right)\\
&\times\int_0^\infty dc'_{12}\int_0^\lambda d\tilde{b}'\,\tilde{b}'c_{12}'^7(7-c_{12}'^2)\sin^2\chi^{(0)\prime}\exp\left(-\frac{1}{2}c_{12}'^2\right), \qquad (7.59)\\
N_3 =& 4\int_0^\infty dc_{12}\int_0^{\tilde{b}_{\max}} d\tilde{b}\,\tilde{b}(\nu^2-\tilde{b}^2)c_{12}^5(105-14c_{12}^2-c_{12}^4)\exp\left(-\frac{1}{2}c_{12}^2\right)\\
&\times\int_0^\infty dc'_{12}\int_0^\lambda d\tilde{b}'\,\tilde{b}'c_{12}'^7\sin^2\chi^{(0)\prime}\exp\left(-\frac{1}{2}c_{12}'^2\right)\\
&-8\int_0^\infty dc_{12}\int_0^{\tilde{b}_{\max}} d\tilde{b}\,\tilde{b}(\nu^2-\tilde{b}^2)c_{12}^5(5-c_{12}^2)\exp\left(-\frac{1}{2}c_{12}^2\right)\\
&\times\int_0^\infty dc'_{12}\int_0^\lambda d\tilde{b}'\,\tilde{b}'c_{12}'^7(7+c_{12}'^2)\sin^2\chi^{(0)\prime}\exp\left(-\frac{1}{2}c_{12}'^2\right), \qquad (7.60)\\
D =& \int_0^\infty dc_{12}\int_0^\lambda d\tilde{b}\,\tilde{b}c_{12}^7\sin^2\chi^{(0)}\exp\left(-\frac{1}{2}c_{12}^2\right)\\
&\times\int_0^\infty dc'_{12}\int_0^\lambda d\tilde{b}'\,\tilde{b}'c_{12}'^7(35-c_{12}'^4)\sin^2\chi^{(0)\prime}\exp\left(-\frac{1}{2}c_{12}'^2\right)\\
&-\int_0^\infty dc_{12}\int_0^\lambda d\tilde{b}\,\tilde{b}c_{12}^7(7-c_{12}^2)\sin^2\chi^{(0)}\exp\left(-\frac{1}{2}c_{12}^2\right)\\
&\times\int_0^\infty dc'_{12}\int_0^\lambda d\tilde{b}'\,\tilde{b}'c_{12}'^7(7+c_{12}'^2)\sin^2\chi^{(0)\prime}\exp\left(-\frac{1}{2}c_{12}'^2\right). \qquad (7.61)
\end{aligned}
$$

Here we have introduced the notation $\chi^{(0)\prime}=\chi^{(0)}(\tilde{b}',c'_{12})$ for simplicity. To obtain these expressions, we have ignored the terms proportional to a_2^2, a_3^2, and a_2a_3 because we are interested in nearly elastic situations. Therefore, from Eq. (7.28), we obtain

$$\mathcal{M}_2=\mathcal{M}_2^{(0)}+\epsilon\mathcal{M}_2^{(1)}+\mathcal{O}(\epsilon^2), \qquad (7.62)$$

where

$$\mathcal{M}_2^{(0)}=0, \qquad (7.63)$$

$$\mathcal{M}_2^{(1)}=\sqrt{2\pi}\int_0^\infty dc_{12}\int_0^{\tilde{b}_{\max}} d\tilde{b}\,\tilde{b}(\nu^2-\tilde{b}^2)c_{12}^5\exp\left(-\frac{1}{2}c_{12}^2\right) \qquad (7.64)$$

with $\tilde{b}_{\max}=\min(\nu(c_{12}),\lambda)$. Substituting Eqs. (7.26) and (7.62) into Eq. (7.25), we obtain the time evolution of the temperature as the solid line

in Fig. 7.3, in which the number density, the restitution coefficient, the potential width ratio, and the initial temperature are, respectively, $nd^3 = 0.05$, $e = 0.99$, $\lambda = 1.5d$, and $T = 10\varepsilon$. When we start from the temperature much higher than the well-depth, the decreases of the temperature obeys Haff's law for hard core systems in the initial stage [12]. As the temperature approaches the well-depth, the rate of temperature decrease is larger than Haff's law. A similar result on the crossover from Haff's law to a faster decrease of the temperature has already been reported by Ref. [96].

Next, let us calculate the transport coefficients. Similar to the previous case, with the dropping the contributions from a_2^2, a_3^2, and $a_2 a_3$, the coefficients Ω_η^e and Ω_κ^e defined in Eqs. (7.52) and (7.55) are, respectively, given by (see Appendix J for the derivation)

$$\begin{cases} \Omega_\eta^e = \Omega_\eta^{e(0)} + \epsilon\, \Omega_\eta^{e(0)} + \mathcal{O}(\epsilon^2) \\ \Omega_\kappa^e = \Omega_\kappa^{e(0)} + \epsilon\, \Omega_\kappa^{e(0)} + \mathcal{O}(\epsilon^2) \end{cases}, \tag{7.65}$$

with

$$\Omega_\eta^{e(0)} = -\frac{\sqrt{2\pi}}{4} \int_0^\infty dc_{12} \int_0^\lambda d\tilde{b}\, \tilde{b} c_{12}^7 \sin^2 \chi^{(0)} \exp\left(-\frac{1}{2} c_{12}^2\right), \tag{7.66}$$

$$\begin{aligned} \Omega_\eta^{e(1)} =& -a_2^{(1)} \frac{\sqrt{2\pi}}{128} \int_0^\infty dc_{12} \int_0^\lambda d\tilde{b}\, \tilde{b} c_{12}^7 \left(63 - 18c_{12}^2 + c_{12}^4\right) \sin^2 \chi^{(0)} \exp\left(-\frac{1}{2} c_{12}^2\right) \\ & - a_3^{(1)} \frac{\sqrt{2\pi}}{1536} \int_0^\infty dc_{12} \int_0^\lambda d\tilde{b}\, \tilde{b} c_{12}^7 \left(693 - 297c_{12}^2 + 33c_{12}^4 - c_{12}^6\right) \sin^2 \chi^{(0)} \exp\left(-\frac{1}{2} c_{12}^2\right) \\ & - \frac{\sqrt{2\pi}}{4} \int_0^\infty dc_{12} \int_0^\lambda d\tilde{b}\, \tilde{b} c_{12}^7 \chi^{(1)} \sin 2\chi^{(0)} \exp\left(-\frac{1}{2} c_{12}^2\right) \\ & + \sqrt{2\pi} \int_0^\infty dc_{12} \int_0^{\tilde{b}_{\max}} d\tilde{b}\, \tilde{b} (\nu^2 - \tilde{b}^2) c_{12}^7 \left(\frac{2}{3} - \sin^2 \frac{\chi^{(0)}}{2}\right) \exp\left(-\frac{1}{2} c_{12}^2\right), \end{aligned} \tag{7.67}$$

$$\Omega_\kappa^{e(0)} = -\frac{\sqrt{2\pi}}{4} \int_0^\infty dc_{12} \int_0^\lambda d\tilde{b}\, \tilde{b} c_{12}^7 \sin^2 \chi^{(0)} \exp\left(-\frac{1}{2} c_{12}^2\right), \tag{7.68}$$

$$
\begin{aligned}
\Omega_\kappa^{e(1)} =& a_2^{(1)} \frac{\sqrt{2\pi}}{128} \int_0^\infty dc_{12} \int_0^\lambda d\tilde{b}\, \tilde{b} c_{12}^7 \left(63 - 18c_{12}^2 + c_{12}^4\right) \sin^2 \chi^{(0)} \exp\left(-\frac{1}{2}c_{12}^2\right) \\
&+ a_3^{(1)} \frac{\sqrt{2\pi}}{1536} \int_0^\infty dc_{12} \int_0^\lambda d\tilde{b}\, \tilde{b} c_{12}^7 \left(693 - 297c_{12}^2 + 33c_{12}^4 - c_{12}^6\right) \sin^2 \chi^{(0)} \exp\left(-\frac{1}{2}c_{12}^2\right) \\
&- \frac{\sqrt{2\pi}}{4} \int_0^\infty dc_{12} \int_0^\lambda d\tilde{b}\, \tilde{b} c_{12}^7 \chi^{(1)} \sin 2\chi^{(0)} \exp\left(-\frac{1}{2}c_{12}^2\right) \\
&+ \sqrt{2\pi} \int_0^\infty dc_{12} \int_0^{\tilde{b}_{\max}} d\tilde{b}\, \tilde{b} (\nu^2 - \tilde{b}^2) c_{12}^7 \cos^2 \frac{\chi^{(0)}}{2} \exp\left(-\frac{1}{2}c_{12}^2\right) \\
&+ \frac{\sqrt{2\pi}}{8} \int_0^\infty dc_{12} \int_0^{\tilde{b}_{\max}} d\tilde{b}\, \tilde{b} (\nu^2 - \tilde{b}^2) c_{12}^5 \left(25 - 11c_{12}^2\right) \exp\left(-\frac{1}{2}c_{12}^2\right).
\end{aligned} \tag{7.69}
$$

It should be noted that the zeroth order of these quantities, Eqs. (7.66) and (7.68), are the exactly same as the ones obtained by the previous study [148].

Let us perturbatively solve the differential equation of the shear viscosity (7.51) with respect to the small parameter ϵ. We expand the shear viscosity as

$$
\eta = \eta^{(0)} + \epsilon \eta^{(1)} + \mathcal{O}(\epsilon^2). \tag{7.70}
$$

From Eqs. (7.62), (7.65), and (7.70), we rewrite the differential equation of the shear viscosity (7.51) as

$$
\begin{aligned}
&- \frac{2}{3} n d^2 \sqrt{\frac{2T}{m}} \left(\epsilon \mathcal{M}_2^{(1)} + \cdots\right) T \frac{\partial}{\partial T} \left(\eta^{(0)} + \epsilon \eta^{(1)} + \cdots\right) \\
&- \frac{2}{5} n d^2 \sqrt{\frac{2T}{m}} \left(\Omega_\eta^{e(0)} + \epsilon\, \Omega_\eta^{e(0)} + \cdots\right) \left(\eta^{(0)} + \epsilon \eta^{(1)} + \cdots\right) \\
&= nT.
\end{aligned} \tag{7.71}
$$

Solving the zeroth and first order of this equation, we obtain

$$
\eta^{(0)} = -\frac{5}{2d^2} \sqrt{\frac{mT}{2}} \frac{1}{\Omega_\eta^{e(0)}}, \tag{7.72}
$$

$$
\eta^{(1)} = -\left(\frac{\Omega_\eta^{e(1)}}{\Omega_\eta^{e(0)}} + \frac{5}{3} \frac{\mathcal{M}_2^{(1)} T}{\Omega_\eta^{e(0)}} \frac{\partial}{\partial T}\right) \eta^{(0)}. \tag{7.73}
$$

Similarly, the thermal conductivity κ and the coefficient μ are, respectively, given by

$$
\kappa = \kappa^{(0)} + \epsilon \kappa^{(1)} + \mathcal{O}(\epsilon^2), \tag{7.74}
$$

$$
\mu = \mu^{(0)} + \epsilon \mu^{(1)} + \mathcal{O}(\epsilon^2) \tag{7.75}
$$

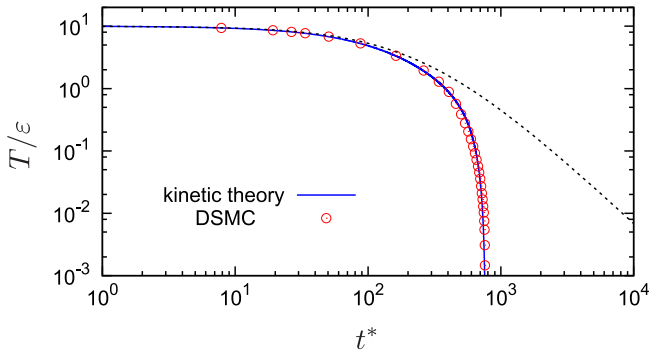

Figure 7.3: (Color online) The time evolution of the granular temperature for $nd^3 = 0.05$, $\lambda = 1.5$, and $e = 0.99$ obtained by the kinetic theory (blue solid line) and that by the DSMC (red open circles), where $t^* = t\sqrt{\varepsilon/m}/d$ and the initial temperature is set to be 10ε. The dotted line represents Haff's law for inelastic hard core spheres in which each particle has the diameter d.

with

$$\kappa^{(0)} = -\frac{75}{16d^2}\sqrt{\frac{2T}{m}}\frac{1}{\Omega_\kappa^{e(0)}}, \tag{7.76}$$

$$\kappa^{(1)} = -\frac{\Omega_\kappa^{e(1)}}{\Omega_\kappa^{e(0)}}\kappa^{(0)} - \frac{75}{8d^2}\sqrt{\frac{2T}{m}}\frac{a_2^{(1)}}{\Omega_\kappa^{e(0)}} - \frac{5}{2d^2}\frac{1}{\sqrt{T}\Omega_\kappa^{e(0)}}\frac{\partial}{\partial T}\left(\mathcal{M}_2^{(1)}\kappa^{(0)}T^{3/2}\right), \tag{7.77}$$

$$\mu^{(0)} = 0, \tag{7.78}$$

$$\mu^{(1)} = -\frac{5}{2n}\frac{\mathcal{M}_2^{(1)}\kappa^{(0)}T}{\Omega_\kappa^{e(0)}} - \frac{75}{8nd^2}\sqrt{\frac{T^3}{2m}}\frac{a_2^{(1)}}{\Omega_\kappa^{e(0)}}. \tag{7.79}$$

We note that the zeroth order terms of these transport coefficients, Eqs. (7.72) and (7.76) are identical to those obtained by the previous studies [148].

We obtain the expressions of the transport coefficients as Eqs. (7.62), (7.70), (7.74), and (7.75). The above procedure is not practically efficient to perform the hydrodynamic simulation because we need to calculate the double integrals at every step. To reduce the calculation cost, we compare the results with high and low temperature expansions. From the calculation in Appendix K, we can obtain the explicit expressions of the dissipation rate and the transport coefficients as in Table 7.2. As a final remark in this section, we note that our results up to a_2 order in Eq. (7.56) are almost identical to those up to a_3 in the elastic limit. This ensures that the expansion around the Maxwellian gives well converged results by Eq. (7.56).

Table 7.2: High temperature expansion of each quantity and low temperature expansion of the second moment up to first order of ε/T and ϵ.

$$\mathcal{M}_2 = 2\sqrt{2\pi}\epsilon\left(1+\frac{\varepsilon}{T}\right) \quad (T\to\infty), \quad \mathcal{M}_2 = 2\sqrt{2\pi}\epsilon\left(1+\lambda^2\frac{\varepsilon}{T}\right) \quad (T\to 0)$$

$$\Omega_\eta^e = -4\sqrt{2\pi}\left[1+\epsilon\frac{11}{1280}-\frac{\varepsilon}{T}\frac{\lambda-1}{96}\left\{2(15\lambda^4+15\lambda^3+2\lambda^2+2\lambda+2)\right.\right.$$
$$\left.\left.+3\lambda^2(\lambda+1)(5\lambda^2-1)\log\frac{\lambda-1}{\lambda+1}\right\}\right],$$

$$\Omega_\kappa^e = -4\sqrt{2\pi}\left[1+\epsilon\frac{1989}{1280}-\frac{\varepsilon}{T}\frac{\lambda-1}{96}\left\{2(15\lambda^4+15\lambda^3+2\lambda^2+2\lambda+2)\right.\right.$$
$$\left.\left.+3\lambda^2(\lambda+1)(5\lambda^2-1)\log\frac{\lambda-1}{\lambda+1}\right\}\right],$$

$$\eta = \frac{5}{16d^2}\sqrt{\frac{mT}{\pi}}\left[1+\epsilon\frac{1567}{3840}+\frac{\varepsilon}{T}\frac{\lambda-1}{96}\left\{2(15\lambda^4+15\lambda^3+2\lambda^2+2\lambda+2)\right.\right.$$
$$\left.\left.+3\lambda^2(\lambda+1)(5\lambda^2-1)\log\frac{\lambda-1}{\lambda+1}\right\}\right],$$

$$\kappa = \frac{75}{64d^2}\sqrt{\frac{T}{\pi m}}\left[1+\epsilon\frac{539}{1280}+\frac{\varepsilon}{T}\frac{\lambda-1}{96}\left\{2(15\lambda^4+15\lambda^3+2\lambda^2+2\lambda+2)\right.\right.$$
$$\left.\left.+3\lambda^2(\lambda+1)(5\lambda^2-1)\log\frac{\lambda-1}{\lambda+1}\right\}\right],$$

$$\mu = \epsilon\frac{1185}{1024nd^2}\sqrt{\frac{T^3}{\pi m}}.$$

7.4 Comparison with the numerical results

To check the validity of the kinetic theory, we compare the transport coefficients derived from the kinetic theory in the previous section with those obtained by the DSMC, which is known as the accurate numerical method to solve the Boltzmann equation [123–125, 131]. We note that stochastic treatment of collisions via DSMC ensures the system uniform, which is suitable to measure the transport coefficients.

7.4.1 Cooling coefficient

In this subsection, we check the time evolution of the granular temperature for homogeneous cooling state and the second moment $\mathcal{M}_2$. We prepare monodisperse N particles in a cubic box with the linear system size L. We distribute particles at random as an initial condition, where the initial velocity distribution obeys Maxwellian with the temperature $T = 10\varepsilon$. Figure 7.3 shows the time evolution of the temperature obtained by the DSMC and Eq. (7.25), in which the number of particles, the system size, the number density, the potential width, and the restitution coefficient are, respectively, $N = 12,500$, $L = 50d$, $nd^3 = 0.05$ $\lambda = 1.5d$, and $e = 0.99$. The time evolution obtained by the kinetic theory fairly agrees with that by the DSMC. Figure 7.4 shows the comparison of the second moment $\mathcal{M}_2$ obtained by the kinetic theory with that by the DSMC, which is also consistent each other, where $\mathcal{M}_2$ at high temperature limit is identical to that for the hard core system with the diameter d.

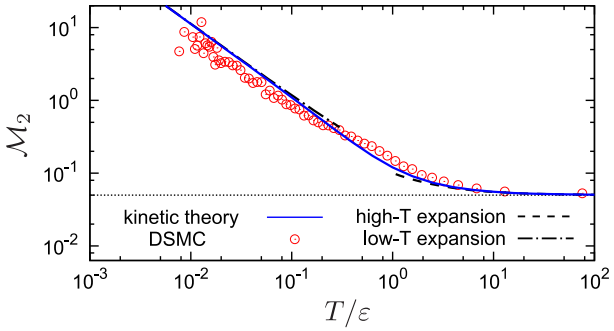

Figure 7.4: (Color online) The granular temperature dependence of the second moment $\mathcal{M}_2$ obtained by the DSMC (red open circles) and that by the kinetic theory up to a_3 order (blue solid line), where T^* is the dimensionless temperature defined by $T^* = T/\varepsilon$. The dotted line represents $\mathcal{M}_2$ for the hard core system with the diameter d. The dashed (dot-dashed) line represents $\mathcal{M}_2$ obtained from the high (low) temperature expansion.

7.4.2 Shear viscosity

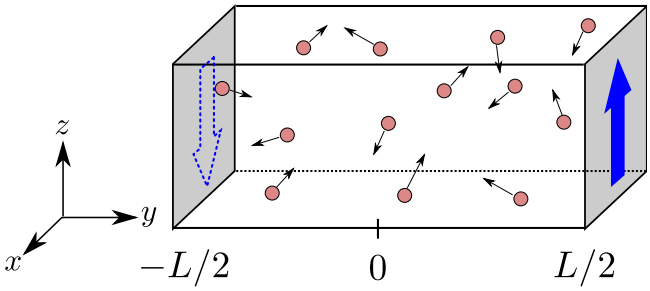

Figure 7.5: (Color online) A schematic view of our setup to measure the shear viscosity. The walls at $y = L/2$ ($y = -L/2$) move to positive (negative) z-direction, respectively.

Let us compare the result of the shear viscosity by the kinetic theory with that by the DSMC in this subsection. The particles are distributed at random and the velocity distribution satisfies Maxwellian at the initial condition. Then, we apply the shear with the aid of the Lees-Edwards walls at $y = \pm L/2$, whose z-component is $\pm V_{\rm wall}$. In the initial stage, the energy injection from shear is not balanced with the energy dissipation. Then, as time goes on, the system reaches a nonequilibrium steady state. In this stage, we calculate the shear viscosity defined by

$$\eta = -\lim_{t\to\infty} \frac{P_{xy}}{\dot{\gamma}}, \tag{7.80}$$

where $\dot{\gamma}$ is a bulk shear rate defined by the gradient of the flow velocity U_z and P_{xy} can be measured by the DSMC. To suppress the boundary effects, we measure $\dot{\gamma}$ in the range $-L/4 \le y \le L/4$, that is, $\dot{\gamma} = (U_z|_{y=L/4} - U_z|_{y=-L/4})/(L/2)$. Although the Newtonian shear viscosity should be measured by a relaxation process from the initial perturbation for the homogeneous cooling system [128, 154, 155], this method is hard to reduce numerical errors. It is also noted that the Newtonian viscosity is known to be identical to the steady state shear viscosity in the elastic limit [58], which is the reason why we adopt the above setup. Figure 7.6 shows the comparison of the shear viscosity obtained by the kinetic theory with that by the DSMC, in which the number of particles, the system size, the number density, the potential width, and the restitution coefficient are, respectively, $L = 3,000d$, $nd^3 = 0.01$ $\lambda = 2.5d$, and $e = 0.99$. Similar to the case of $\mathcal{M}_2$, the shear viscosity obtained by the DSMC is identical to that of the kinetic theory for the hard core system of the diameter d in the high temperature limit. We cannot measure the shear viscosity below $T \simeq 10^{-1}\varepsilon$ because the system is heat up by the shear even if we start from a lower

temperature. The first order solution of the kinetic theory with respect to ϵ also deviates from the zeroth order solution below this temperature, which suggests that the hydrodynamic description is no longer valid in this regime. This may correspond to the limitation of the inelastic Boltzmann equation, where the trapping processes cannot be ignored even in the elastic limit.

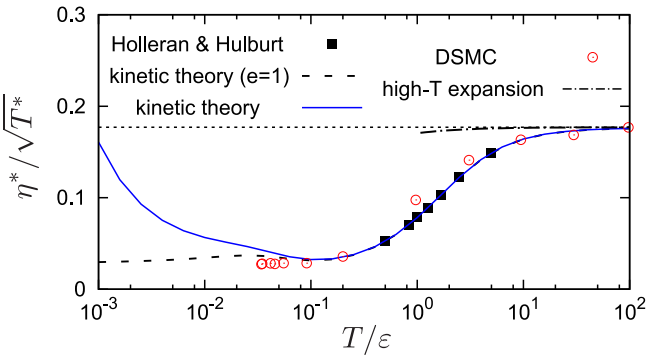

Figure 7.6: (Color online) Granular temperature dependence of the shear viscosity obtained by the DSMC (red open circles), that by the elastic kinetic theory (black solid squares in the previous study [148] and black dashed line), and that by the kinetic theory (blue solid line), where η^* is the dimensionless shear viscosity defined by $\eta^* = \eta d^2/\sqrt{m\varepsilon}$. The dotted line represents the shear viscosity for the hard core system of the diameter d. The dot-dashed line represents the shear viscosity obtained from the high temperature expansion.

7.4.3 Thermal conductivity

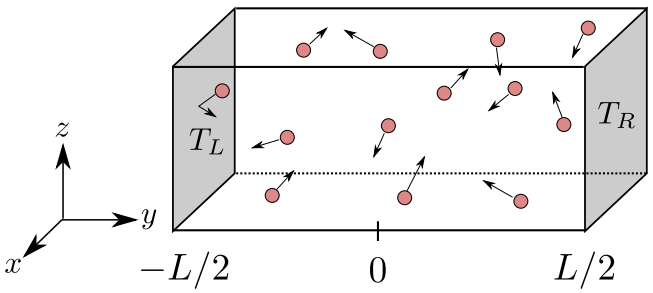

Figure 7.7: (Color online) A schematic view of our setup to measure the thermal conductivity. The temperature of the left (right) side wall is kept at $T_{\rm L}$ ($T_{\rm R}$).

Third, we compare the thermal conductivity by the kinetic theory with

that by the DSMC. Although the heat flux contains the term proportional to the density gradient, we ignore its contribution because the term disappears in the elastic limit $e \to 1$ as in Eq. (7.78). To obtain the thermal conductivity from the DSMC, we solve the heat equation under a confined geometry shown in Fig. 7.7, where the temperature at the left (right) wall at $y = -L/2$ ($y = L/2$) keeps $T_{\rm L}$ ($T_{\rm R}$) [156–158]. In the steady state, because hydrodynamic variables depend only on y, the heat equation (7.31) is reduced to

$$\frac{2}{3n}\frac{d}{dy}q_y = \zeta T, \quad q_y = -\kappa\frac{d}{dy}T. \tag{7.81}$$

Let us nondimensionalize the quantities using the mass m, the system size L, and the well depth ε as

$$n = \frac{n^*}{L^3}, \quad y = Ly^*, \quad T = \varepsilon T^*, \tag{7.82}$$

$$p = \frac{\varepsilon}{L^3}p^*, \quad \mathcal{M}_2 = \left(\frac{d}{L}\right)\mathcal{M}_2^*, \quad \kappa' = \frac{1}{m^{1/2}L^2}\kappa'^*. \tag{7.83}$$

Thus, we rewrite the heat equation as

$$\frac{d^2}{dy^{*2}}\theta = -3\gamma^2\theta^{-1/3} \tag{7.84}$$

with $\theta = T^{*3/2}$ and $\gamma^2 = (1/\sqrt{2})p^{*2}\mathcal{M}_2^*/\kappa'^*$. By multiplying $d\theta/dy^*$ in both sides of Eq. (7.84) and integrating the equation from $y^* = 0$ to y^*, we obtain

$$\frac{d\theta}{dy^*} = \pm\frac{1}{\sqrt{C - 9\gamma^2\theta^{2/3}}}, \tag{7.85}$$

where C is given by $C = \theta_0'^2 + 9\gamma^2\theta_0^{2/3}$ with $\theta_0 = \theta|_{y^*=0}$ and $\theta_0' = d\theta/dy^*|_{y^*=0}$. Here, we consider the system that the temperature at $y = -L/2$ is lower than that at $y = L/2$, in which the plus sign is selected in Eq. (7.85). Under this condition, the solution of Eq. (7.85) has the following form

$$y^* = \frac{\theta_0^{1/3}}{2\gamma}\left[-\Theta\sqrt{\beta^2 - \Theta^2} + \beta^2\arctan\left(\frac{\Theta}{\sqrt{\beta^2 - \Theta^2}}\right)\right.$$
$$\left. + \sqrt{\beta^2 - 1} - \beta^2\arctan\left(\frac{1}{\sqrt{\beta^2 - 1}}\right)\right], \tag{7.86}$$

where $\beta = \{(\theta'^2/9\gamma^2\theta_0^{2/3}) + 1\}^{1/2}$ and $\Theta = (\theta/\theta_0)^{1/3}$.

To obtain κ' from the DSMC, we numerically evaluate γ from the comparison of the temperature profile (7.86) with that by the DSMC in the range $-L/5 \le y \le L/10$ as in Fig. 7.8. It should be noted that we omit the

data near the walls to suppress the boundary effects. Using the estimated γ and the simulation results θ_0, θ_0', and $\mathcal{M}_2$ in the homogeneous freely cooling, we estimate κ' in terms of the DSMC. Here, the number of particles, the system size, the number density, the potential width, and the restitution coefficient are, respectively, $L = 3,000d$, $nd^3 = 0.01$ $\lambda = 2.5d$, and $e = 0.99$. Figure 7.9 shows the results of the DSMC and the kinetic theory, which is similar to that for η. The heat conductivity in the high temperature limit of DSMC is identical to that for the hard core system of the diameter d as indicated by the kinetic theory. We note that the profile of the temperature described by Eq. (7.86) cannot be achieved below $T \simeq 10^{-1}\varepsilon$. In addition, the deviation between the zeroth and the first oder solutions with respect to ϵ appear below $T \simeq 10^{-1}\varepsilon$ as in the case of the viscosity.

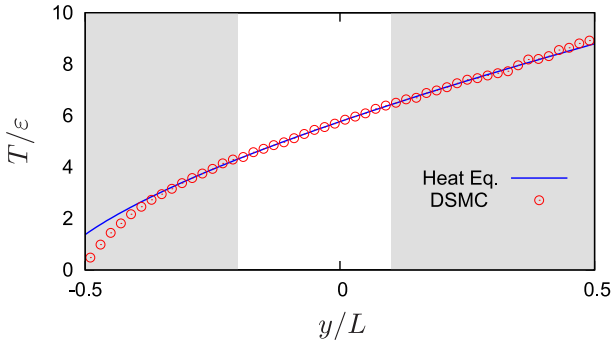

Figure 7.8: (Color online) The solution of the heat equation (blue solid line) and the temperature profile obtained by the DSMC (red open circles). We choose γ to fit the DSMC result in the range $-L/5 \leq y \leq L/10$.

7.5 Discussion

In this chapter, we have obtained the transport coefficients as a function of the granular temperature. The transport coefficients in high temperature limit are identical to those for the hard core system with the diameter d. Let us consider this reason. As explained in Sec. 7.2, the collision is an inelastic for $b < \min(\nu d, \lambda d)$ and an elastic grazing collision for $\min(\nu d, \lambda d) < b < \lambda d$. The value of $\nu = \sqrt{1 + 4\varepsilon/(mv^2)}$ converges to 1 in high temperature limit. On the other hand, grazing collisions only change the directions of colliding particles and the kinetic energy is kept unchanged. Therefore, the energy change by collisions in high temperature limit is identical to that for the hard core system of the diameter d.

Below $T \simeq 10^{-1}\varepsilon$, the first order solutions of the transport coefficients with respect to ϵ deviate from the zeroth order solutions. Moreover, the first

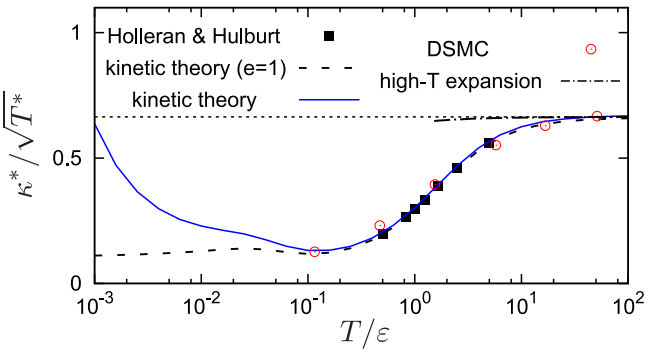

Figure 7.9: (Color online) The temperature dependence of the thermal conductivity obtained by the DSMC (red open circles), that by the elastic kinetic theory (black solid squares in the previous study [148] and black dashed line), and that by the kinetic theory (blue solid line), where κ^* is the dimensionless thermal conductivity defined by $\kappa^* = \kappa d^2\sqrt{m/\varepsilon}$. The dotted line represents the thermal conductivity for the hard core system of the diameter d.The dot-dashed line represents the shear viscosity obtained from the high temperature expansion.

order solutions diverge as T^{-1} in the low temperature limit. This is because ν diverges as

$$\nu = \sqrt{1 + \frac{2\varepsilon}{Tc_{12}^2}} \sim T^{-1/2} \tag{7.87}$$

in the low temperature limit. This indicates that the hydrodynamic description in terms of the perturbation method is no longer valid for low temperature, where the trapping process cannot be ignored.

Murphy and Subramaniam [96] studied the homogeneous cooling state for a system of particles having an inelastic hard core associated with van der Waals potential. They obtained that the time evolution of the granular temperature obeys the Haff's law in the initial stage and decreases faster as time goes on, then approaches to the Haff's law for $e = 0$. They considered that the particles aggregate after the collision when two particles have small kinetic energy with compared to the potential well keeping the potential contribution after the coalescence. Although we do not consider the aggregation process, the time evolution of the granular temperature in Fig. 7.3 is similar to their result. We will study the effects of aggregation to complete our analysis in near future.

It should be noted that the diffusion coefficient can be evaluated by $\Omega^{(1,1)*}$ defined by Eq. (L.4) in Appendix L. The evaluation of the diffusion coefficient by the event-driven MD is inconsistent with the theoretical prediction, but this inconsistency comes from the acceleration of particles

trapped in the well region for MD which is not included in the theory. We will have to solve this problem by improving the theoretical treatment.

In this chapter, we have only focused on the dilute system, in which the density dependence of the transport coefficients does not appear. To derive the transport coefficients for denser systems is our future work.

7.6 Conclusion

In this chapter, we have developed the kinetic theory for dilute cohesive granular gases having the square well potential to derive the hydrodynamic equations using the Champan-Enskog theory for the inelastic Boltzmann equation. We have obtained the second moment $\mathcal{M}_2$ of the collision integral and the transport coefficients for this system. We have found that they are identical to those for hard core gases at high temperature and the hydrodynamic description is no longer valid at low temperature. We have also performed DSMC simulation to check the validity of the kinetic theory and found that all results of DSMC are consistent with those obtained by the kinetic theory.

Chapter 8

Summary

In this thesis, we have studied transport phenomena of cohesive granular particles numerically and theoretically. In chapter 6, we have studied the spatial patterns under a plane shear by controlling the density, the dimensionless shear rate, and the dissipation rate. We found the existence of various distinct steady phases depending on these parameters. We have also drawn the phase diagrams for several fixed densities. In addition, the shape of clusters depends on the initial condition of velocities of particles, when the dissipation is strong. We have also found that there is a quasi particle-hole symmetry for the shape of clusters in steady states. We have found that the VDF near the interface between the dense region and the gas region in the dense-plate coexistence phase deviates from the Gaussian function. Introducing a stochastic model and its corresponding Kramers equation, we have obtained its perturbative VDF, which reproduces the semi-quantitative behavior of the VDF observed in MD simulations. This result suggests that the motion of a gas particle near the interface is subjected to Coulombic friction force whose origin is the activation energy in the dense region.

In chapter 7, we have developed the kinetic theory based on the inelastic Boltzmann equation for the cohesive granular particles. We have derived the expression of the second moment of the collision integral and the transport phenomena for a system of hard core particles having a square well potential. We have found that the results are identical to those for hard core gases at high temperature, but hydrodynamic description is no longer valid at low temperature. We have also performed DSMC simulation and checked the validity of the kinetic theory.

In this thesis, we do not consider the aggregation process among cohesive grains, which cannot be ignored for low temperature regime as shown in chapter 7. This effect will be treated to complete our analysis in near future. In addition, we may need to consider the effect of a liquid-gas phase transition as shown in chapter 4, which cannot be included in the framework of the present kinetic theory. For a sheared system, we need to consider a

different base state to construct a theory, in which shear thickening behavior [159] is expected similar to a dry system. A extension to a moderately dense case is also our future work. When the density is higher, we need to construct a different theory, such as that by Ref. [57].

Acknowledgement

I would like to express my deepest appreciation to Prof. Hisao Hayakawa, who is my supervisor, for his continuous encouragement, kind and suggestive advice on my research including writing up this thesis as well as his intensive discussion with me. I also gratefully thank Prof. Kuniyasu Saitoh, who is my collaborator, for his helpful comments as well as his kind and technical advice on my research since I have joined Prof. Hayakawa's group. I would like to thank all members including former members of Prof. Hayakawa's group, in particular, Dr. Kiyoshi Kanazawa, Mr. Tomohiko G. Sano, Dr. Ryosuke Yoshii, and Dr. Koshiro Suzuki for their kind advice and fruitful discussion on research. I am also grateful to all supporting staffs of Yukawa Institute for Theoretical Physics (YITP) and Division of Physics and Astronomy, Graduate School of Science, Kyoto University for their kindness and hospitality.

I am grateful to Prof. Takahiro Hatano, Prof. Michio Otsuki, Prof. Ko Okumura, Prof. Hiroaki Katsuragi, Prof. Ooshida Takeshi, Prof. Tetsuo Yamaguchi, Prof. Takenobu Nakamura Dr. Masamichi J. Miyama, and people in the granular material community for their advice and fruitful discussion. I also thank Prof. Meheboob Alam for fruitful discussion to initiate the project of kinetic theory in the initial stage during his stay in YITP and my stay in Jawaharlal Nehru Centre for Advanced Scientific Research (JNCASR). I wish to express sincere gratitude to Prof. Andrés Santos for his continuous encouragement and kind advice on the kinetic theory. I also thanks Mr. Masanari Hattori and Prof. Shingo Kosuge for their kind explanation on the simulation method. I appreciate Prof. Vicente Garzó and Prof. Francisco Vega Reyes for their suggestive advice on the kinetic theory.

I thank the bilateral international exchange program (BIEP) of the Global COE program, which enables me to stay at JNCASR and collaborate with Prof. Alam. I am also grateful to Japan Student Services Organization (JASSO), which enables me to continue study at graduate school.

Finally, I thank my family for their support of my life.

Appendix A

Results of the physical boundary condition

In this Appendix, we present the results of our simulations under the flat boundary condition which is one of the typical physical boundaries to clarify the influence of the boundary condition. We prepare flat walls at $z = \pm L/2$, moving at velocities $\pm\dot{\gamma}L/2$ in y-direction, respectively. When a particle with a velocity (v_x, v_y, v_z) hits the walls at $z = \pm L/2$, the velocity is changed as $(v_x, \pm\dot{\gamma}L/2 - v_y, -v_z)$ after the collision, respectively. The phase diagram of the system for the physical boundary for $n^* = 0.305$ is presented in Fig. A.1. We have obtained three steady phases such as the uniformly sheared phase, the coexistence phase between dense-plate and gas regions, and the dense-plate cluster phase. The phase diagram is almost same as the corresponding one under the Lees-Edwards boundary condition (see Figs. 6.4(d)). This can be understood as follows: if two particles at the symmetric positions with respect to the origin of the system simultaneously collide the walls at $z = L/2$ and $-L/2$, the pair of velocities after collisions is same as that after passing across the boundaries at $z = \pm L/2$ for the system under the Lees-Edwards boundary condition. This is realized after the averaging over the collisions. Thus, the flat boundary condition is essentially equivalent to the Lees-Edwards boundary condition.

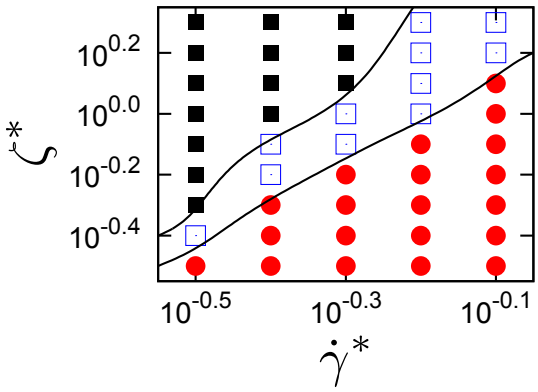

Figure A.1: (Color online) Phase diagram under the flat boundary condition for $n^* = 0.305$, uniformly sheared state (red filled circle, Fig. 6.3(a)), coexistence of a dense-plate and gases (blue open square, Fig. 6.3(d)), and an isolated dense-plate (black filled square, Fig. 6.3(g)).

Appendix B

Calculation of Coulombic friction constant

In this appendix, we try to illustrate the existence of Coulombic friction force for the motion of a tracer particle near the interface. Let us consider a situation that a gas particle hits and slides on the wall formed by the particles in the dense region (see Fig. 6.9). If the kinetic energy of the gas particle is less than the potential energy formed by the particles in the dense region, it should be trapped in the potential well. Therefore, the motion of the gas particle is restricted near the interface. In this case, we can write the N-body distribution function near the interface $\rho(\mathbf{\Gamma}, t)$ by using the distribution function in the equilibrium system as [136, 160–162]

$$\rho(\mathbf{\Gamma}, t) = \rho_{\rm eq}(\mathbf{\Gamma}) \exp\left[\int_0^t d\tau \Omega(-\tau, \mathbf{\Gamma}, \dot{\gamma}_l, \zeta)\right], \tag{B.1}$$

where $\mathbf{\Gamma} = \{\boldsymbol{r}_i, \boldsymbol{p}_i\}_{i=1}^N$, $\rho_{\rm eq}(\mathbf{\Gamma})$ is the equilibrium distribution function at time $t = 0$, and

$$\begin{aligned}\Omega(t, \mathbf{\Gamma}, \dot{\gamma}, \zeta) =& -\beta\dot{\gamma}V\sigma_{yz}(t, \mathbf{\Gamma}, \dot{\gamma}, \zeta) \\ & - 2\beta\mathcal{R}(t, \mathbf{\Gamma}, \dot{\gamma}, \zeta) - \Lambda(t, \mathbf{\Gamma}, \dot{\gamma}, \zeta),\end{aligned} \tag{B.2}$$

with

$$\sigma_{\alpha\beta}(t, \mathbf{\Gamma}, \dot{\gamma}, \zeta) = \sum_i \left\{ \frac{p_{i,\alpha}p_{i,\beta}}{m} - \sum_{j\neq i} r_{i,\alpha}\frac{\partial U^{\rm LJ}(r_{ij})}{\partial r_{i,\beta}} + \sum_{j\neq i} r_{i,\alpha}F_\beta^{\rm vis}(\boldsymbol{r}_{ij}, \boldsymbol{v}_{ij}) \right\}, \tag{B.3}$$

$$\mathcal{R}(t, \mathbf{\Gamma}, \dot{\gamma}, \zeta) = \frac{\zeta}{4}\sum_{i\neq j}\Theta(\sigma - r_{ij})(\boldsymbol{v}_{ij}\cdot\hat{\boldsymbol{r}}_{ij})^2, \tag{B.4}$$

$$\Lambda(t,\mathbf{\Gamma},\dot{\gamma},\zeta) = -\frac{\zeta}{m}\sum_{i\neq j}\Theta(\sigma - r_{ij}), \tag{B.5}$$

$$F_\beta^{\rm vis}(\boldsymbol{r}_{ij},\boldsymbol{v}_{ij}) = -\zeta\Theta(\sigma - r_{ij})(\boldsymbol{v}_{ij}\cdot\hat{\boldsymbol{r}}_{ij})\frac{r_{ij,\beta}}{r_{ij}}. \tag{B.6}$$

Here, we have introduced the inverse granular temperature $\beta = 1/T$ and the local shear rate $\dot{\gamma}_l$ in the interface region. If the dissipation is small and the shear rate is not large, we may assume that $\Omega(-t) \simeq -\beta\dot{\gamma}V\sigma_{yz}^{\rm mf}(-t)$, where $\sigma_{yz}^{\rm mf}$ is the mean field yz component of the stress tensor. We also assume that the stress tensor decays exponentially as $\sigma_{yz}^{\rm mf}(-t) \simeq \sigma_{yz}^{\rm mf}(0)\exp(-|t|/\tau_0)$ [136], where τ_0 is the relaxation time of the stress tensor. From these relationships, we may use the approximate expression

$$\rho(\mathbf{\Gamma},t) \simeq \prod_{i=1}^{N_l}\frac{1}{Z^{\rm mf}}\exp\left[-\beta\left(H^{\rm mf} - \Delta E_i\right)\right]\exp\left(-\beta\tau_0\dot{\gamma}_l V_l\sigma_{yz}^{\rm mf}(0)\right), \tag{B.7}$$

where $H^{\rm mf}$ and ΔE_i, are respectively, the mean field Hamiltonian per particle in the interface and the energy fluctuation of the particle i which may be the activation energy from the local trap. Here N_l and V_l are, respectively, the number of particles and the volume in the interface region and $Z^{\rm mf} = \int d\boldsymbol{r}d\boldsymbol{p}\exp(-\beta H^{\rm mf})$. There are two characteristic time scales $\dot{\gamma}^{-1}$ and $\dot{\gamma}_l^{-1}$ corresponding to the uniform region and the interface between dense and dilute regions. Because the time scale is obtained from the average over the distribution function (B.7) or the local mean field distribution, the relationship between $\dot{\gamma}^{-1}$ and $\dot{\gamma}_l^{-1}$ is expected to be

$$\dot{\gamma}_l^{-1} = \dot{\gamma}^{-1}\exp\left[\beta(\Delta E - \tau_0\dot{\gamma}_l V_l\sigma_{yz}^{\rm mf}(0))\right], \tag{B.8}$$

where we have eliminated the suffix i for the particle. This equation can be rewritten as

$$\sigma_{yz}^{\rm mf}(0) = \frac{1}{\tau_0\dot{\gamma}_l V_l}\left(\Delta E + T\ln\frac{\dot{\gamma}_l}{\dot{\gamma}}\right). \tag{B.9}$$

Therefore, we may estimate Coulombic friction constant as

$$\mu = \frac{\sigma_{yz}^{\rm mf}(0)}{P} = \frac{1}{\tau_0\dot{\gamma}_l PV_l}\left(\Delta E + T\ln\frac{\dot{\gamma}_l}{\dot{\gamma}}\right), \tag{B.10}$$

where $P \simeq 0.90\varepsilon/\sigma^3$, $V_l \simeq 4.3\sigma^3$, $\Delta E \simeq 3.5\varepsilon$ and $\dot{\gamma}_l \simeq 0.83(\varepsilon/m\sigma^2)^{1/2}$ at the interface for a set of parameters $(n^*,\dot{\gamma}^*,\zeta^*) = (0.305, 10^{-0.2}, 10^{0.2})$. In this expression, we cannot determine the relaxation time τ_0 from the simulation, which is estimated to reproduce the average value of the second moment with the aid of Eq. (6.16).

Appendix C

Detailed calculation of the viscous heating term

In this appendix, let us calculate the average of the viscous heating term by using the distribution function near the interface. From Eq. (B.7), we can rewrite the distribution function with the aid of Eq. (B.3) as

$$\rho(\mathbf{\Gamma}, t) \approx \frac{1}{Z} \prod_{i=1}^{N_l} \exp\left[-\beta\left(\frac{\boldsymbol{p}_i^2}{2m} + \tau_0 \dot{\gamma}_l V_l \frac{p_{i,y} p_{i,z}}{m}\right)\right], \tag{C.1}$$

where $Z = \int \prod_{i=1}^{N_l} d\boldsymbol{r}_i d\boldsymbol{p}_i \exp[-\beta(\boldsymbol{p}_i^2/2m + \tau_0 \dot{\gamma}_l V_l p_{i,y} p_{i,z}/m)]$. Then $\langle p_y p_z \rangle$ is given by

$$\begin{aligned}
\langle p_y p_z \rangle &= \int d\mathbf{\Gamma} p_{i,y} p_{i,z} \rho(\mathbf{\Gamma}, t) \\
&\propto \int_{-\infty}^{\infty} dp_{i,y} \int_{-\infty}^{\infty} dp_{i,z} p_{i,y} p_{i,z} \exp\left[-\beta\left(\frac{\boldsymbol{p}_i^2}{2m} + \tau_0 \dot{\gamma}_l V_l \frac{p_{i,y} p_{i,z}}{m}\right)\right] \\
&= \int_0^{\infty} dp \int_0^{2\pi} d\theta p^3 \sin\theta \cos\theta \exp\left[-\beta\left(\frac{p^2}{2m} + \frac{\tau_0 \dot{\gamma}_l V_l}{m} p^2 \sin\theta \cos\theta\right)\right] \\
&= -\frac{\pi}{2} \int_0^{\infty} dp p^3 \exp\left(-\frac{\beta p^2}{2m}\right) I_1\left(\frac{\beta \tau_0 \dot{\gamma}_l V_l}{2m} p^2\right),
\end{aligned} \tag{C.2}$$

where $I_1(x)$ is the modified Bessel function of the first kind [**?**]. Because $I_1(x)$ is positive for $x > 0$, Eq. (C.2) ensures that the viscous heating term $-\dot{\gamma} \langle p_y p_z \rangle$ is always positive near the interface.

Appendix D

A perturbative solution of the Kramers equation

In this appendix, let us solve the Kramers equation (6.9) perturbatively to obtain the steady VDF. Later, we compare this solution with the result of MD.

At first, we adopt the following three assumptions. The first assumption is that the distribution function is independent of both x and y, the coordinates horizontal to the interface. We also assume that the distribution function f depends on z, vertical to the interface, through the density and the granular temperature:

$$\frac{\partial f}{\partial z} = \frac{\partial f}{\partial n}\frac{dn}{dz} + \frac{\partial f}{\partial T}\frac{dT}{dz}. \tag{D.1}$$

Second, we assume that the changes of the density and the granular temperature near the interface can be characterized by the interface width λ as

$$\frac{dn}{dz} \simeq -\frac{n_0}{\lambda}, \quad \frac{dT}{dz} \simeq \frac{T_0}{\lambda}, \tag{D.2}$$

where $n_0 = n(z_0) = (n_l + n_g)/2$, $T_0 = T(z_0) = (T_l + T_g)/2$. Here, n_l and T_l are the density and the granular temperature in the dense region, and n_g and T_g are those in the dilute region, respectively. Third, we also assume that the interface width λ is much longer than the diameter of the particles σ, i.e. $\epsilon \equiv \sigma/\lambda \ll 1$. From these assumptions, $\partial f/\partial z$ may be rewritten as

$$\frac{\partial f}{\partial z} \simeq -\epsilon\left(\frac{n_0}{\sigma}\frac{\partial}{\partial n} - \frac{T_0}{\sigma}\frac{\partial}{\partial T}\right) f. \tag{D.3}$$

To solve Eq. (6.9), we adopt the perturbative expression Eq. (6.10). Equation (6.9), thus, reduces to the following three equations: for the zeroth

order,

$$-\kappa\frac{\partial}{\partial \boldsymbol{p}}\cdot\left(\frac{\boldsymbol{p}}{|\boldsymbol{p}|}f^{(0,0)}\right)-\Delta_{\boldsymbol{p}}f^{(0,0)}=0, \tag{D.4}$$

for the first order of ϵ,

$$-\frac{p_z}{mD}\left(\frac{n_0}{\sigma}\frac{\partial}{\partial n}-\frac{T_0}{\sigma}\frac{\partial}{\partial T}\right)f^{(0,0)}-\kappa\frac{\partial}{\partial \boldsymbol{p}}\cdot\left(\frac{\boldsymbol{p}}{|\boldsymbol{p}|}f^{(0,1)}\right)-\Delta_{\boldsymbol{p}}f^{(0,1)}=0, \tag{D.5}$$

and for the first order of $\dot{\gamma}^*$,

$$-\frac{p_z}{D}\frac{\partial f^{(0,0)}}{\partial p_y}-\kappa\frac{\partial}{\partial \boldsymbol{p}}\cdot\left(\frac{\boldsymbol{p}}{|\boldsymbol{p}|}f^{(1,0)}\right)-\Delta_{\boldsymbol{p}}f^{(1,0)}=0. \tag{D.6}$$

The solution of Eq. (D.4) is given by

$$f^{(0,0)}=C_1\exp(-\kappa p)+C_2\exp(-\kappa p)\mathrm{Ei}\left(\kappa p\right), \tag{D.7}$$

where $\mathrm{Ei}(x)$ is the exponential integral $\mathrm{Ei}(x)\equiv-\int_{-x}^{\infty}(e^{-t}/t)dt$ [163], and C_1 and C_2 are the normalization constants. Here, we set $C_2=0$ because $\mathrm{Ei}(x)$ becomes infinite at $x=0$, and $C_1=\kappa^2/2\pi$ to satisfy the normalization condition without the shear and the density gradient. Using Eq. (D.7), Equations (D.5) and (D.6) can be represented in the polar coordinates as

$$\begin{aligned}&A\left(p^2-\frac{2}{\lambda}p\right)f^{(0,0)}\sin\theta\\&=\kappa\left(\frac{1}{p}+\frac{\partial}{\partial p}\right)f^{(0,1)}+\left(\frac{\partial^2}{\partial p^2}+\frac{1}{p}\frac{\partial}{\partial p}+\frac{1}{p^2}\frac{\partial^2}{\partial\theta^2}\right)f^{(0,1)},\end{aligned} \tag{D.8}$$

and

$$\begin{aligned}&\frac{\kappa}{2Dt_0}pf^{(0,0)}\sin 2\theta\\&=\kappa\left(\frac{1}{p}+\frac{\partial}{\partial p}\right)f^{(1,0)}+\left(\frac{\partial^2}{\partial p^2}+\frac{1}{p}\frac{\partial}{\partial p}+\frac{1}{p^2}\frac{\partial^2}{\partial\theta^2}\right)f^{(1,0)},\end{aligned} \tag{D.9}$$

where we have introduced A as

$$A=\frac{n_0}{m\sigma D}\frac{\partial\kappa}{\partial n}-\frac{T_0}{m\sigma D}\frac{\partial\kappa}{\partial T}. \tag{D.10}$$

To solve Eqs. (D.8) and (D.9), we adopt the expansions for $f^{(i,j)}(p,\theta)=\sum_{n=1}^{\infty}f_n^{(i,j)}(p)\sin(n\theta)$ with $(i,j)=(0,1)$ and $(1,0)$ [143]. Equation (D.8) for each n reduces to the following equations: for $n=1$,

$$\begin{aligned}&\frac{A\kappa^2}{2\pi}\left(p^2-\frac{2}{\kappa}p\right)\exp(-\kappa p)\\&=\kappa\left(\frac{1}{p}+\frac{\partial}{\partial p}\right)f_1^{(0,1)}+\left(\frac{\partial^2}{\partial p^2}+\frac{1}{p}\frac{\partial}{\partial p}-\frac{1}{p^2}\right)f_1^{(0,1)},\end{aligned} \tag{D.11}$$

and for $n \neq 1$,

$$0 = \kappa \left(\frac{1}{p} + \frac{\partial}{\partial p} \right) f_n^{(0,1)} + \left(\frac{\partial^2}{\partial p^2} + \frac{1}{p} \frac{\partial}{\partial p} - \frac{n^2}{p^2} \right) f_n^{(0,1)}. \tag{D.12}$$

The solutions of Eqs. (D.11) and (D.12) are, respectively, given by

$$\begin{aligned} f_1^{(0,1)} =& \frac{C_{11}}{p} + C_{12} \frac{1 + \kappa p}{\kappa^2 p} \\ & - \frac{A}{6\pi} \frac{6 + 6\kappa p + 3\kappa^2 p^2 + \kappa^3 p^3 + \kappa^4 p^4}{\kappa^3 p} \exp(-\kappa p), \end{aligned} \tag{D.13}$$

and

$$\begin{aligned} f_n^{(0,1)} =& C_{n1} (\kappa p)^n \exp(-\kappa p) U(n, 2n+1, \kappa p) \\ & + C_{n2} (\kappa p)^n \exp(-\kappa p) L_{-n}^{2n}(\kappa p), \end{aligned} \tag{D.14}$$

for $n \neq 1$, where $U(a, b, x)$ and $L_a^b(x)$ are, respectively, the confluent hypergeometric function and Laguerre's bi-polynomial [163], and the normalization constants C_{n1} and C_{n2} $(n = 1, 2, \cdots)$ will be determined later. Similarly, Equation (D.9) for each n reduces to the following equations: for $n = 2$,

$$\begin{aligned} & \frac{\kappa^3}{4\pi D t_0} p \exp(-\kappa p) \\ & = \kappa \left(\frac{1}{p} + \frac{\partial}{\partial p} \right) f_2^{(1,0)} + \left(\frac{\partial^2}{\partial p^2} + \frac{1}{p} \frac{\partial}{\partial p} - \frac{4}{p^2} \right) f_2^{(1,0)}, \end{aligned} \tag{D.15}$$

and for $n \neq 2$,

$$0 = \kappa \left(\frac{1}{p} + \frac{\partial}{\partial p} \right) f_n^{(1,0)} + \left(\frac{\partial^2}{\partial p^2} + \frac{1}{p} \frac{\partial}{\partial p} - \frac{n^2}{p^2} \right) f_n^{(1,0)}. \tag{D.16}$$

The solutions of Eqs. (D.15) and (D.16) are, respectively, given by

$$\begin{aligned} f_2^{(1,0)} =& C_{23} \frac{3 - \kappa p}{p^2} + C_{24} \frac{6 + 4\kappa p + \kappa^2 p^2}{\kappa^4 p^2} \exp(-\kappa p) \\ & + \frac{1}{8\pi D t_0} \frac{72 + 48\kappa p + 12\kappa^2 p^2 - \kappa^4 p^4}{\kappa^2 p^2} \exp(-\kappa p), \end{aligned} \tag{D.17}$$

and

$$\begin{aligned} f_n^{(1,0)} =& C_{n3} (\kappa p)^n \exp(-\kappa p) U(n, 2n+1, \kappa p) \\ & + C_{n4} (\kappa p)^n \exp(-\kappa p) L_{-n}^{2n}(\kappa p), \end{aligned} \tag{D.18}$$

for $n \neq 2$, where the normalization constants C_{n3} and C_{n4} $(n = 1, 2, \cdots)$ will be determined later.

Here, let us determine the normalization constants $C_{n1}, \cdots, C_{n4}$ ($n = 1, 2, \cdots$). The distributions $f_n^{(0,1)}$ and $f_n^{(1,0)}$ should be finite at $p = 0$ and approach zero for large p. Therefore, we obtain

$$\begin{aligned} &C_{11} = 0, \quad C_{12} = \frac{A}{\pi\kappa}, \quad C_{23} = 0, \quad C_{24} = -\frac{3\kappa^2}{2\pi D t_0}, \\ &C_{n1} = 0, \quad C_{n2} = 0 \quad (n \neq 1), \\ &C_{n3} = 0, \quad C_{n4} = 0 \quad (n \neq 2). \end{aligned} \tag{D.19}$$

From these results, we obtain

$$f(p, \theta) = f^{(0,0)} + \epsilon f_1^{(0,1)} \sin\theta + \dot{\gamma}^* f_2^{(1,0)} \sin 2\theta, \tag{D.20}$$

where $f^{(0,0)}$, $f_1^{(0,1)}$ and $f_2^{(1,0)}$ are, respectively, given by

$$f^{(0,0)}(p) = \frac{\kappa^2}{2\pi} \exp(-\kappa p), \tag{D.21}$$

$$f_1^{(0,1)}(p) = -\frac{A}{6\pi\kappa} p(3 + \kappa p + \kappa^2 p^2) \exp(-\kappa p), \tag{D.22}$$

$$f_2^{(1,0)}(p) = -\frac{\kappa^2}{8\pi D t_0} p^2 \exp(-\kappa p). \tag{D.23}$$

Appendix E

Detailed calculations of various moments

In this appendix, we calculate the n-th moments of $p_{y'}$ and $p_{z'}$ using the distribution function obtained in Appendix D. From the definition of the moment, n-th moment of an arbitrary function $G(\boldsymbol{p})$ is given by

$$\langle G^n \rangle = \int d\boldsymbol{p}\, G^n(p,\varphi) f(p,\varphi). \tag{E.1}$$

We rotate the coordinate the coordinate (y,z) by θ counterclockwise and introduce the new Cartesian coordinate (y',z') as in Fig. 6.7. From this definition, we obtain the n-th moments of $p_{y'}$, for $n=2$,

$$\begin{aligned}\langle p_{y'}^2 \rangle =& \int_0^\infty dp \int_0^{2\pi} d\varphi p^3 \cos^2(\varphi-\theta) \\ & \times \left[f^{(0,0)}(p) + \epsilon f_1^{(0,1)}(p)\sin\varphi + \dot{\gamma}^* f_2^{(1,0)}(p)\sin 2\varphi \right] \\ =& \frac{3}{\kappa^2}\left(1 - \frac{5\dot{\gamma}}{2D\kappa^2}\sin 2\theta\right),\end{aligned} \tag{E.2}$$

for $n=3$,

$$\begin{aligned}\langle p_{y'}^3 \rangle =& \int_0^\infty dp \int_0^{2\pi} d\varphi p^4 \cos^3(\varphi-\theta) \\ & \times \left[f^{(0,0)}(p) + \epsilon f_1^{(0,1)}(p)\sin\varphi + \dot{\gamma}^* f_2^{(1,0)}(p)\sin 2\varphi \right] \\ =& -\frac{765\epsilon A}{\kappa^7}\sin\theta,\end{aligned} \tag{E.3}$$

and for $n = 4$,

$$\begin{aligned}\left\langle p_{y'}^4 \right\rangle =& \int_0^\infty dp \int_0^{2\pi} d\varphi p^5 \cos^4(\varphi - \theta) \\ & \times \left[f^{(0,0)}(p) + \epsilon f_1^{(0,1)}(p) \sin\varphi + \dot{\gamma}^* f_2^{(1,0)}(p) \sin 2\varphi \right] \\ =& \frac{45}{\kappa^4} \left(1 - \frac{7\dot{\gamma}}{D\kappa^2} \sin 2\theta \right). \end{aligned} \tag{E.4}$$

Similarly, we can calculate the each moment of $p_{z'}$ so that we obtain Eqs. (6.16)–(6.19).

Appendix F

Velocity distribution function for each direction

In this appendix, we derive the velocity distribution function in the Cartesian coordinate (y, z) at first, and calculate the velocity distribution functions in y and z-directions. The velocity distribution function in the polar coordinates (p, θ) is given by Eq. (6.12), where we replace θ by $\theta - \psi$ as in Eqs. (6.16)–(6.19), which can be converted into the form in Cartesian coordinate as

$$\begin{aligned} f(p_y, p_z) =& \frac{\kappa^2}{2\pi} \exp(-\kappa p) \left[1 - \frac{\epsilon A}{3\kappa^3} p(3 + \kappa p + \kappa^2 p^2) \sin(\theta - \psi) - \frac{\dot{\gamma}}{4D} p^2 \sin 2(\theta - \psi) \right] \\ =& \frac{\kappa^2}{2\pi} \exp(-\kappa p) \left[1 + \frac{\epsilon A}{3\kappa^3} (3 + \kappa p + \kappa^2 p^2)(p_y \sin\psi - p_z \cos\psi) \right. \\ & \left. + \frac{\dot{\gamma}}{4D} \left\{ (p_y^2 - p_z^2) \sin 2\psi - 2 p_y p_z \cos 2\psi \right\} \right], \end{aligned} \tag{F.1}$$

where $p = \sqrt{p_y^2 + p_z^2}$. Next, let us calculate the velocity distribution functions in y and z directions. In this paper, we focus on the VDF for the fluctuation velocity, which is defined by the deviation from the average velocity. Therefore, we can replace p_y and p_z by mu_y and mu_z in Eq. (F.1). The velocity distribution function in y-direction, $P(u_y)$, is given by integrating Eq. (F.1) with respect to u_z as

$$\begin{aligned} P(u_y) =& \int_{-\infty}^{\infty} d(mu_z) f(mu_y, mu_z) \\ =& \frac{m\kappa^2}{2\pi} \int_{-\infty}^{\infty} du_z \exp(-m\kappa u) \\ & \times \left[1 + \frac{m\epsilon A}{3\kappa^3} \left(3 + m\kappa u + m^2 \kappa^2 u^2 \right) u_y \sin\psi + \frac{m^2 \dot{\gamma}}{4D} (u_y^2 - u_z^2) \sin 2\psi \right], \end{aligned} \tag{F.2}$$

where $u = \sqrt{u_y^2 + u_z^2}$. Similarly, we can calculate the velocity distribution function in z-direction $P(p_z)$ as

$$\begin{aligned} P(u_z) =& \int_{-\infty}^{\infty} d(mu_y) f(mu_y, mu_z) \\ =& \frac{m\kappa^2}{2\pi} \int_{-\infty}^{\infty} du_y \exp\left(-m\kappa u\right) \\ & \times \left[1 - \frac{m\epsilon A}{3\kappa^3} \left(3 + m\kappa u + m^2\kappa^2 u^2\right) u_z \cos\psi + \frac{m^2\dot{\gamma}}{4D}(u_y^2 - u_z^2) \sin 2\psi\right]. \end{aligned} \tag{F.3}$$

Appendix G

Collision geometry for the square well potential

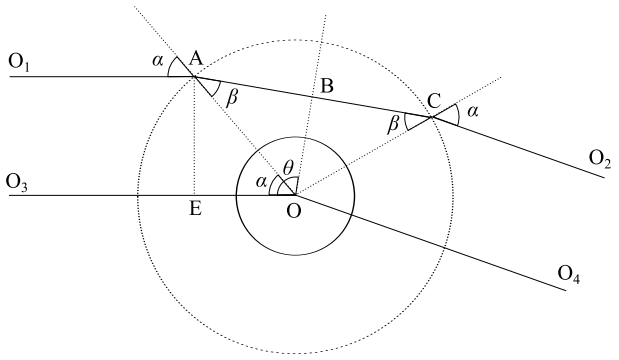

Figure G.1: Collision geometry for a grazing collision. Two particles approach from O_1 and leave for O_2. The solid and dotted circles represent the hard core (radius d) and the outer edge of the potential (radius λd), respectively.

In this appendix, let us explain the collision geometry scattered by the square well potential. First, we consider the case for a grazing collision as in Fig. G.1 in the frame that the target is stationary. Let us consider the process that two particles approach from far away with relative velocity $\boldsymbol{v}$ from O_1. When the incident particle enters the well at the point A, the relative velocity changes because of the conservation of the energy and the angular momentum, whose speed inside the well is given by νv. At the point A, the relative velocity perpendicular to OA is conserved, that is, $v \sin\alpha = \nu v \sin\beta$ is satisfied [152]. The change of the velocity parallel to

OA is given by

$$\begin{aligned}\nu v\cos\beta - v\cos\alpha &= \nu v\sqrt{1-\frac{1}{\nu^2}\sin^2\alpha} - v\cos\alpha \\ &= \left(\sqrt{\nu^2-\sin^2\alpha} - \cos\alpha\right) v, \end{aligned} \tag{G.1}$$

which means that the velocity change $\Delta\boldsymbol{v}_{\mathrm{A}}$ at the point A satisfies

$$\Delta\boldsymbol{v}_{\mathrm{A}} = -\left(\sqrt{\nu^2-\sin^2\alpha} - \cos\alpha\right) v\hat{\boldsymbol{r}}_{\mathrm{A}} \tag{G.2}$$

with the unit vector $\hat{\boldsymbol{r}}_{\mathrm{A}} = (\cos(\pi-\alpha), \sin(\pi-\alpha))^{\mathrm{T}}$ parallel to OA. We note that the minus sign in Eq. (G.2) comes from the fact that the velocity change is opposite direction to $\hat{\boldsymbol{r}}_{\mathrm{A}}$.

Similarly, the component of the velocity change parallel to OC at the point C is given by $(\cos\alpha - \sqrt{\nu^2-\sin^2\alpha})v$, which means that the velocity change $\Delta\boldsymbol{v}_{\mathrm{C}}$ at the point C becomes

$$\Delta\boldsymbol{v}_{\mathrm{C}} = -\left(\sqrt{\nu^2-\sin^2\alpha} - \cos\alpha\right) v\hat{\boldsymbol{r}}_{\mathrm{C}} \tag{G.3}$$

with the unit vector $\hat{\boldsymbol{r}}_{\mathrm{C}} = (\cos(\pi-2\theta+\alpha), \sin(\pi-2\theta+\alpha))^{\mathrm{T}}$.

From Eqs. (G.2) and (G.3), the velocity change $\Delta\boldsymbol{v}$ during this grazing collision becomes

$$\begin{aligned}\Delta\boldsymbol{v} &= \Delta\boldsymbol{v}_{\mathrm{A}} + \Delta\boldsymbol{v}_{\mathrm{C}} \\ &= -2\left(\sqrt{\nu^2-\sin^2\alpha} - \cos\alpha\right) \\ &\qquad \times v\cos(\theta-\alpha)\begin{pmatrix}\cos(\pi-\theta)\\ \sin(\pi-\theta)\end{pmatrix}. \end{aligned} \tag{G.4}$$

From Eq. (7.7) and $\alpha = \arcsin(\mathrm{AE}/\mathrm{OA}) = \arcsin(b/\lambda d)$, the following relationships are satisfied:

$$\cos(\theta-\alpha) = \cos\left(\frac{\pi}{2} - \arcsin\frac{b}{\nu\lambda d}\right) = \frac{b}{\nu\lambda d}, \tag{G.5}$$

$$\begin{aligned}\cos\theta &= \sin\left(\arcsin\frac{b}{\nu\lambda d} - \arcsin\frac{b}{\lambda d}\right) \\ &= \sin\left(\arcsin\frac{b}{\nu\lambda d}\right)\cos\left(\arcsin\frac{b}{\lambda d}\right) \\ &\quad - \cos\left(\arcsin\frac{b}{\nu\lambda d}\right)\sin\left(\arcsin\frac{b}{\lambda d}\right) \\ &= \frac{b}{\nu\lambda^2 d^2}\left(\sqrt{\lambda^2 d^2 - b^2} - \sqrt{\nu^2\lambda^2 d^2 - b^2}\right), \end{aligned} \tag{G.6}$$

and

$$\begin{aligned}&\sqrt{\nu^2-\sin^2\alpha}-\cos\alpha\\&=\frac{1}{\lambda d}\left(\sqrt{\nu^2\lambda^2d^2-b^2}-\sqrt{\lambda^2d^2-b^2}\right).\end{aligned}\tag{G.7}$$

From these equations, we can rewrite Eq. (G.4) as

$$\begin{aligned}\Delta\boldsymbol{v}&=2v\cos\theta\begin{pmatrix}\cos(\pi-\theta)\\\sin(\pi-\theta)\end{pmatrix}\\&=-2v\cos(\pi-\theta)\begin{pmatrix}\cos(\pi-\theta)\\\sin(\pi-\theta)\end{pmatrix}\\&=-2(\boldsymbol{v}\cdot\hat{\boldsymbol{k}})\hat{\boldsymbol{k}},\end{aligned}\tag{G.8}$$

with the unit vector $\hat{\boldsymbol{k}}=(\cos(\pi-\theta),\sin(\pi-\theta))^{\mathrm{T}}$.

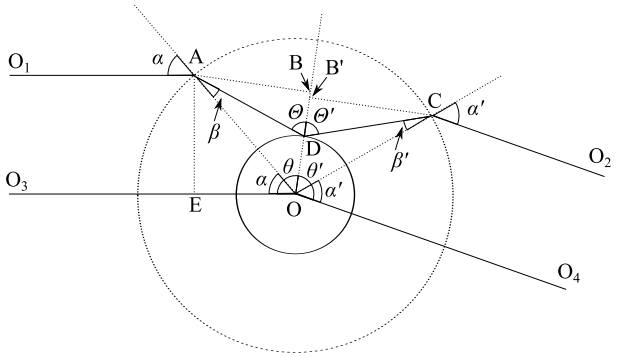

Figure G.2: Collision geometry for a core collision. Two particles approach from O_1 and leave for O_2.The solid and dotted lines represent the hard core (radius d) and the outer edge of the potential (radius λd), respectively.

Next, let us consider the case for a hard core collision as in Fig. G.2. In this case, an inelastic collision takes place at the point D. To calculate the energy dissipation at the point D, we consider the angle Θ between the relative velocity of the particle and OB. From $\mathrm{AB}=\lambda d\sin(\theta-\alpha)$, $\mathrm{BD}=\mathrm{OB}-\mathrm{OD}=(\lambda\cos(\theta-\alpha)-1)d$, we can write Θ as

$$\tan\Theta=\frac{\mathrm{AD}}{\mathrm{BD}}=\frac{\lambda\sin(\theta-\alpha)}{\lambda\cos(\theta-\alpha)-1}.\tag{G.9}$$

From Eq. (7.10), $\cos(\theta-\alpha)$ and $\sin(\theta-\alpha)$ are, respectively, given by

$$\begin{aligned}\cos(\theta-\alpha) &= \cos\left(\arcsin\frac{b}{\nu d}-\arcsin\frac{b}{\nu\lambda d}\right)\\ &= \frac{1}{\nu^2\lambda d^2}\left(\sqrt{\nu^2d^2-b^2}\sqrt{\nu^2\lambda^2d^2-b^2}+b^2\right), \qquad \text{(G.10)}\\ \sin(\theta-\alpha) &= \sin\left(\arcsin\frac{b}{\nu d}-\arcsin\frac{b}{\nu\lambda d}\right)\\ &= \frac{1}{\nu^2\lambda d^2}\left(\sqrt{\nu^2\lambda^2d^2-b^2}-\sqrt{\nu^2d^2-b^2}\right), \qquad \text{(G.11)}\end{aligned}$$

and substituting Eqs. (G.10) and (G.11) into Eq. (G.9), we obtain

$$\tan\Theta = \frac{b}{\sqrt{\nu^2d^2-b^2}}, \qquad \text{(G.12)}$$

or, equivalently, Eq. (7.12). From this, we can calculate the change Δv^2 after the collision at the point B as

$$\begin{aligned}\Delta v^2 &= -(1-e^2)\nu^2v^2\cos^2\Theta\\ &= -(1-e^2)v^2\left(\nu^2-\frac{b^2}{d^2}\right). \qquad \text{(G.13)}\end{aligned}$$

Correspondingly, the change of relative velocity $\Delta\boldsymbol{v}$ is given by

$$\begin{aligned}\Delta\boldsymbol{v} &= -\left[(\boldsymbol{v}\cdot\hat{\boldsymbol{k}})+\sqrt{(\boldsymbol{v}\cdot\hat{\boldsymbol{k}})^2-(1-e^2)\nu^2v^2\cos^2\Theta}\right]\hat{\boldsymbol{k}}\\ &= -2\left[1-\frac{1}{2}\epsilon\nu^2\frac{\cos^2\Theta}{\cos^2\theta}\right](\boldsymbol{v}\cdot\hat{\boldsymbol{k}})\hat{\boldsymbol{k}}+\mathcal{O}(\epsilon^2), \qquad \text{(G.14)}\end{aligned}$$

which reduces to $\Delta\boldsymbol{v}=-2(\boldsymbol{v}\cdot\hat{\boldsymbol{k}})\hat{\boldsymbol{k}}$ in the elastic limit.

Appendix H

Chapman-Enskog expansion

In this Appendix, let us explain the outline of the Chapman-Enskog theory [44, 46]. As explained in chapter 7, the zeroth order distribution function, $f^{(0)}$, is determined by Eq. (7.40) in the form Eq. (7.23) [31]. The first order distribution $f^{(1)}$, satisfies Eq. (7.46), which can be rewritten as

$$\begin{aligned}&\frac{\partial^{(0)} f^{(1)}}{\partial t} + J^{(1)}\left(f^{(0)}, f^{(1)}\right) - \zeta^{(1)} T \frac{\partial f^{(0)}}{\partial T} \\ &= \boldsymbol{A}\cdot\boldsymbol{\nabla}\log T + \boldsymbol{B}\cdot\boldsymbol{\nabla}\log n + C_{ij}\nabla_j U_i,\end{aligned} \tag{H.1}$$

where the coefficients $\boldsymbol{A}$, $\boldsymbol{B}$, and C_{ij} are, respectively, given by

$$\begin{aligned}\boldsymbol{A}(\boldsymbol{V}) &= \frac{1}{2}\boldsymbol{V}\frac{\partial}{\partial \boldsymbol{V}}\cdot\left(\boldsymbol{V} f^{(0)}\right) - \frac{T}{m}\frac{\partial}{\partial \boldsymbol{V}} f^{(0)} \\ &= \boldsymbol{V}\left[\frac{T}{m}\left(\frac{mV^2}{2T} - 1\right)\frac{1}{V}\frac{\partial}{\partial V} + \frac{3}{2}\right] f^{(0)},\end{aligned} \tag{H.2}$$

$$\begin{aligned}\boldsymbol{B}(\boldsymbol{V}) &= -\boldsymbol{V} f^{(0)} - \frac{T}{m}\frac{\partial}{\partial \boldsymbol{V}} f^{(0)} \\ &= -\boldsymbol{V}\left(\frac{T}{m}\frac{1}{V}\frac{\partial}{\partial V} + 1\right) f^{(0)},\end{aligned} \tag{H.3}$$

$$\begin{aligned}C_{ij}(\boldsymbol{V}) &= \frac{\partial}{\partial V_i}\left(V_j f^{(0)}\right) - \frac{1}{3}\delta_{ij}\frac{\partial}{\partial \boldsymbol{V}}\cdot\left(\boldsymbol{V} f^{(0)}\right) \\ &= \left(V_i V_j - \frac{1}{3}\delta_{ij} V^2\right)\frac{1}{V}\frac{\partial f^{(0)}}{\partial V}.\end{aligned} \tag{H.4}$$

From Eq. (H.1), $f^{(1)}$ is expected to have the form

$$f^{(1)} = \mathcal{A}\cdot\boldsymbol{\nabla}\log T + \mathcal{B}\cdot\boldsymbol{\nabla}\log n + \mathcal{C}_{ij}\nabla_j U_i. \tag{H.5}$$

The relationships between the coefficients $\mathcal{A}$, $\mathcal{B}$, $\mathcal{C}_{ij}$ and $\boldsymbol{A}$, $\boldsymbol{B}$, C_{ij} are, respectively, obtained by substituting the solution Eq. (H.5) into Eq. (H.1)

as:

$$-T\frac{\partial}{\partial T}\left(\zeta^{(0)}\mathcal{A}\right)+J^{(1)}\left(f^{(0)},\mathcal{A}\right)=\boldsymbol{A}, \tag{H.6}$$

$$-\zeta^{(0)}T\frac{\partial\mathcal{B}}{\partial T}-\zeta^{(0)}\mathcal{A}+J^{(1)}\left(f^{(0)},\mathcal{B}\right)=\boldsymbol{B}, \tag{H.7}$$

$$-\zeta^{(0)}T\frac{\partial\mathcal{C}_{ij}}{\partial T}+J^{(1)}\left(f^{(0)},\mathcal{C}_{ij}\right)=C_{ij}, \tag{H.8}$$

where we have used $\zeta^{(1)}=0$ because the coefficient C_{ij} is traceless.

Substituting Eq. (H.5) into Eq. (7.32) with the aid of Eqs. (7.42) and (7.49), we obtain

$$\int d\boldsymbol{V}D_{ij}(\boldsymbol{V})\mathcal{C}_{kl}(\boldsymbol{V})\nabla_l U_k=-\eta\left(\nabla_i U_j+\nabla_j U_i-\frac{2}{3}\delta_{ij}\boldsymbol{\nabla}\cdot\boldsymbol{U}\right). \tag{H.9}$$

Therefore, the shear viscosity η is given by

$$\eta=-\frac{1}{10}\int d\boldsymbol{V}D_{ij}(\boldsymbol{V})\mathcal{C}_{ji}(\boldsymbol{V}). \tag{H.10}$$

Substituting Eq. (7.56) into Eq. (H.4), we obtain the explicit form of $C_{ij}(\boldsymbol{V})$ as

$$C_{ij}(\boldsymbol{V})=-\frac{1}{T}D_{ij}(\boldsymbol{V})\left\{1+\sum_{\ell}\left[S_\ell(c^2)+S_{\ell-1}^{(3/2)}(c^2)\right]\right\}f_{\rm M}(V). \tag{H.11}$$

This form and Eq. (H.8) leads to

$$\mathcal{C}_{ij}(\boldsymbol{V})=\frac{\mathcal{C}_1}{T}D_{ij}(\boldsymbol{V})f_{\rm M}(V), \tag{H.12}$$

where $\mathcal{C}_1$ is a constant. Substituting Eq. (H.12) into Eq. (H.10), we obtain $\mathcal{C}_1=-\eta/(nT)$.

Similarly, substituting $f^{(1)}$ into Eq. (7.33) with the aid of Eqs. (7.42) and (7.50), we obtain

$$\left\{\frac{1}{T}\int d\boldsymbol{V}S_i(\boldsymbol{V})\mathcal{A}_j(\boldsymbol{V})\right\}\nabla_j T=-\kappa\nabla_i T, \tag{H.13}$$

$$\left\{\frac{1}{n}\int d\boldsymbol{V}S_i(\boldsymbol{V})\mathcal{B}_j(\boldsymbol{V})\right\}\nabla_j n=-\mu\nabla_i n. \tag{H.14}$$

Therefore, we, respectively, obtain the thermal conductivity and the coefficient μ as

$$\kappa=-\frac{1}{3T}\int d\boldsymbol{V}\boldsymbol{S}(\boldsymbol{V})\cdot\mathcal{A}(\boldsymbol{V}), \tag{H.15}$$

$$\mu=-\frac{1}{3n}\int d\boldsymbol{V}\boldsymbol{S}(\boldsymbol{V})\cdot\mathcal{B}(\boldsymbol{V}). \tag{H.16}$$

Substituting Eq. (7.56) into Eqs. (H.2) and (H.3), we obtain the explicit forms of $\boldsymbol{A}(\boldsymbol{V})$ and $\boldsymbol{B}(\boldsymbol{V})$ as

$$\begin{aligned}\boldsymbol{A}(\boldsymbol{V}) =& \boldsymbol{V}\left\{S_1^{(3/2)}(c^2)\left[1+a_2\left(S_2^{(3/2)}(c^2)-\frac{3}{2}\right)\right]\right. \\ &\left.+\sum_{\ell=3}^{\infty}a_\ell\left[S_1^{(3/2)}(c^2)S_\ell(c^2)+(1-c^2)S_{\ell-1}^{(3/2)}(c^2)\right]\right\}f_{\mathrm{M}}(V),\end{aligned} \tag{H.17}$$

$$\boldsymbol{B}(\boldsymbol{V}) = \sum_{\ell} a_\ell \boldsymbol{V} S_{\ell-1}^{(3/2)}(c^2) f_{\mathrm{M}}(V). \tag{H.18}$$

Equations (H.6) and (H.7) leads to

$$\mathcal{A} = -\frac{\mathcal{A}_1}{T}\boldsymbol{S}(\boldsymbol{V})f_{\mathrm{M}}(V), \tag{H.19}$$

$$\mathcal{B} = -\frac{\mathcal{B}_1}{T}\boldsymbol{S}(\boldsymbol{V})f_{\mathrm{M}}(V), \tag{H.20}$$

where $\mathcal{A}_1$ and $\mathcal{B}_1$ are constants. Substituting Eqs. (H.2) and (H.3) into Eq. (H.15) and (H.16), respectively, and integrating over $\boldsymbol{V}$, we obtain $\mathcal{A}_1 = 2m\kappa/5nT$ and $\mathcal{B}_1 = 2m\mu/5T^2$.

Let us determine the explicit forms of the transport coefficients. Multiplying Eq. (H.8) by $D_{ij}(\boldsymbol{V}_1)$ and integrate over $\boldsymbol{V}_1$, we obtain

$$\begin{aligned}&10\zeta^{(0)}T\frac{\partial\eta}{\partial T}+\int d\boldsymbol{V}_1 D_{ij}(\boldsymbol{V}_1)J^{(1)}\left(f^{(0)},\mathcal{C}_{ij}\right) \\ &=\int d\boldsymbol{V}_1 D_{ij}(\boldsymbol{V}_1)C_{ij}(\boldsymbol{V}_1).\end{aligned} \tag{H.21}$$

The second term on the left-hand-side of Eq. (H.21) is written as

$$\int d\boldsymbol{V}_1 D_{ij}(\boldsymbol{V})J^{(1)}\left(f^{(0)},\mathcal{C}_{ij}\right) = 4\eta n d^2\sqrt{\frac{2T}{m}}\Omega_\eta^e, \tag{H.22}$$

where Ω_η^e is defined as Eq. (7.52). Similarly, the right-hand-side of Eq. (H.21) satisfies

$$\int d\boldsymbol{V}_1 D_{ij}(\boldsymbol{V})C_{ij}(\boldsymbol{V}_1) = 10nT. \tag{H.23}$$

Therefore, Eq. (H.21) is reduced to Eq. (7.51). The perturbative solution of Eq. (7.51) with respect to the small inelasticity is given by Eq. (7.70).

Similarly, we derive the differential equation for the thermal conductivity κ. Multiplying Eq. (H.6) by $\boldsymbol{S}(\boldsymbol{V}_1)/T$ and integrating over $\boldsymbol{V}_1$, we obtain

$$\begin{aligned}&\frac{\partial}{\partial T}\left(3\zeta^{(0)}\kappa T\right)+\frac{1}{T}\int d\boldsymbol{V}_1\boldsymbol{S}(\boldsymbol{V}_1)J^{(1)}\left(f^{(0)},\mathcal{A}\right) \\ &=\frac{1}{T}\int d\boldsymbol{V}_1\boldsymbol{S}(\boldsymbol{V}_1)\cdot\boldsymbol{A}(\boldsymbol{V}_1).\end{aligned} \tag{H.24}$$

The second term on the left-hand-side of Eq. (H.24) is written as

$$\frac{1}{T}\int d\boldsymbol{V}_1 \boldsymbol{S}(\boldsymbol{V}_1) J^{(1)}\left(f^{(0)}, \mathcal{A}\right) = \frac{4}{5}\kappa n d^2 \sqrt{\frac{2T}{m}}\Omega_\kappa^e, \tag{H.25}$$

where Ω_κ^e is given by Eq. (7.55). The right-hand-side on Eq. (H.24) satisfies

$$\frac{1}{T}\int d\boldsymbol{V}_1 \boldsymbol{S}(\boldsymbol{V}_1)\cdot\boldsymbol{A}(\boldsymbol{V}_1) = -\frac{15}{2}\frac{nT}{m}\left(1+2a_2\right). \tag{H.26}$$

It should be noted that terms proportional to a_n ($n \geq 3$) vanish due to the orthogonality of the Sonine polynomials. Therefore, Eq. (H.24) is reduced to Eq. (7.53). The solution of Eq. (7.53) is given by Eq. (7.74).

Similarly, multiplying Eq. (H.7) by $\boldsymbol{S}(\boldsymbol{V}_1)/T$ and integrating over $\boldsymbol{V}_1$, the coefficient μ is given by Eq. (7.75).

Appendix I

Determination of a_2 and a_3

In this appendix, we determine the coefficients a_2 and a_3 using the moments of the dimensionless collision integrals [68–70]. It is useful to introduce the basic integral [46]

$$J_{k,l,m,n,p,\alpha} \equiv \int d\boldsymbol{C} \int d\boldsymbol{c}_{12} \int d\hat{\boldsymbol{k}} \tilde{\sigma}(\chi, c_{12}, \xi) |\boldsymbol{c}_{12} \cdot \hat{\boldsymbol{k}}|^{1+\alpha} \times \phi(C)\phi(c_{12}) C^k c_{12}^l (\boldsymbol{C} \cdot \boldsymbol{c}_{12})^m (\boldsymbol{C} \cdot \hat{\boldsymbol{k}})^n (\boldsymbol{c}_{12} \cdot \hat{\boldsymbol{k}})^p, \tag{I.1}$$

with $\boldsymbol{C} = (\boldsymbol{c}_1 + \boldsymbol{c}_2)/2$. This is rewritten as

$$\begin{aligned} J_{k,l,m,n,p,\alpha} =& 2^{-(k+m+n-1)/2} \Gamma\left(\frac{k+m+n+3}{2}\right) \pi^{-1/2} \sum_{j=0}^{n} \binom{n}{j} \left[1 + (-1)^j\right] \\ & \times \frac{\Gamma\left(\frac{1+j}{2}\right)}{\Gamma\left(\frac{2+j}{2}\right)} \int_0^\pi d\Theta \sin^{j+1}\Theta \cos^{m+n-j}\Theta \\ & \times \int_0^\infty dc_{12} \int_0^\infty d\tilde{b}\, \tilde{b} c_{12}^{l+m+p+\alpha+3} \\ & \times \sin^{n+p-j}\frac{\chi}{2} \left|\sin\frac{\chi}{2}\right|^\alpha \cos^j\frac{\chi}{2} \exp\left(-\frac{1}{2}c_{12}^2\right). \end{aligned} \tag{I.2}$$

For $\alpha = 0$ and $n = 0$, 1 and 2, Eq. (I.2) reduces to

$$\begin{aligned} J_{k,l,m,0,p,0} =& \frac{2^{-(k+m-3)/2}}{m+1} \left[1 + (-1)^m\right] \Gamma\left(\frac{k+m+3}{2}\right) \\ & \times \int_0^\infty dc_{12} \int_0^\infty d\tilde{b}\, \tilde{b} c_{12}^{l+m+p+3} \sin^p\frac{\chi}{2} \exp\left(-\frac{1}{2}c_{12}^2\right), \end{aligned} \tag{I.3}$$

$$J_{k,l,m,1,p,0} = \frac{2^{-(k+m-2)/2}}{m+2}\left[1-(-1)^m\right]\Gamma\left(\frac{k+m+4}{2}\right) \times \int_0^\infty dc_{12}\int_0^\infty d\tilde{b}\,\tilde{b}c_{12}^{l+m+p+3}\sin^{p+1}\frac{\chi}{2}\exp\left(-\frac{1}{2}c_{12}^2\right), \tag{I.4}$$

$$J_{k,l,m,2,p,0} = \frac{2^{-(k+m-1)/2}}{(m+1)(m+3)}\left[1+(-1)^m\right]\Gamma\left(\frac{k+m+5}{2}\right) \times \int_0^\infty dc_{12}\int_0^\infty d\tilde{b}\,\tilde{b}c_{12}^{l+m+p+3}\sin^{p}\frac{\chi}{2}\left(1+m\sin^2\frac{\chi}{2}\right)\exp\left(-\frac{1}{2}c_{12}^2\right), \tag{I.5}$$

respectively. These integrals recover the previous results in the hard core limit [46]. In this paper, we only consider the nearly elastic case $1-e \ll 1$. We assume that the coefficients a_2 and a_3 are proportional to $1-e$. When we use the truncated distribution function Eq. (7.56), we rewrite the n-th moment $\mathcal{M}_p = -\int d\boldsymbol{c}_1 c_1^p \tilde{I}(\tilde{f}^{(0)}, \tilde{f}^{(0)})$ $(p \in \mathbb{N})$ as

$$\mathcal{M}_p = -\frac{1}{2}\int d\boldsymbol{C}d\boldsymbol{c}_{12}d\hat{\boldsymbol{k}}\tilde{\sigma}(\chi, c_{12}, \xi)|\boldsymbol{c}_{12}\cdot\hat{\boldsymbol{k}}|\phi(c_1)\phi(c_2)(\boldsymbol{c}_{12}\cdot\hat{\boldsymbol{k}})^2 \times \left[1+a_2(S_2(c_1^2)+S_2(c_2^2))+a_3(S_3(c_1^2)+S_3(c_2^2))\right]\Delta\left(c_1^p+c_2^p\right), \tag{I.6}$$

where, we have ignored the terms proportional to a_2^2, a_3^2, and a_2a_3, because they are the order of $(1-e)^2$. The explicit forms of $\Delta(c_1^p+c_2^p)$ for $p=2$, 4, and 6 are, respectively, given by

$$\Delta(c_1^2+c_2^2) = -\epsilon\Theta(\tilde{b}_{\max}-\tilde{b})\nu^2\frac{\cos^2\Theta}{\cos^2\theta}(\boldsymbol{c}_{12}\cdot\hat{\boldsymbol{k}})^2+\mathcal{O}(\epsilon^2), \tag{I.7}$$

$$\begin{aligned}\Delta(c_1^4+c_2^4) =& -8(\boldsymbol{C}\cdot\boldsymbol{c}_{12})(\boldsymbol{C}\cdot\hat{\boldsymbol{k}})(\boldsymbol{c}_{12}\cdot\hat{\boldsymbol{k}})+8(\boldsymbol{C}\cdot\hat{\boldsymbol{k}})^2(\boldsymbol{c}_{12}\cdot\hat{\boldsymbol{k}})^2 \\ &+\epsilon\,\Theta(\tilde{b}_{\max}-\tilde{b})\nu^2\frac{\cos^2\Theta}{\cos^2\theta}\Big[-2C^2(\boldsymbol{c}_{12}\cdot\hat{\boldsymbol{k}})^2-\frac{1}{2}c_{12}^2(\boldsymbol{c}_{12}\cdot\hat{\boldsymbol{k}})^2 \\ &\quad +4(\boldsymbol{C}\cdot\boldsymbol{c}_{12})(\boldsymbol{C}\cdot\hat{\boldsymbol{k}})(\boldsymbol{c}_{12}\cdot\hat{\boldsymbol{k}})-8(\boldsymbol{C}\cdot\hat{\boldsymbol{k}})^2(\boldsymbol{c}_{12}\cdot\hat{\boldsymbol{k}})^2\Big] \\ &+\mathcal{O}(\epsilon^2),\end{aligned} \tag{I.8}$$

$$
\begin{aligned}
\Delta(c_1^6+c_2^6) =& -24C^2(\boldsymbol{C}\cdot\boldsymbol{c}_{12})(\boldsymbol{C}\cdot\hat{\boldsymbol{k}})(\boldsymbol{c}_{12}\cdot\hat{\boldsymbol{k}})+24C^2(\boldsymbol{C}\cdot\hat{\boldsymbol{k}})^2(\boldsymbol{c}_{12}\cdot\hat{\boldsymbol{k}})^2\\
&-6c_{12}^2(\boldsymbol{C}\cdot\boldsymbol{c}_{12})(\boldsymbol{C}\cdot\hat{\boldsymbol{k}})(\boldsymbol{c}_{12}\cdot\hat{\boldsymbol{k}})+6c_{12}^2(\boldsymbol{C}\cdot\hat{\boldsymbol{k}})^2(\boldsymbol{c}_{12}\cdot\hat{\boldsymbol{k}})^2\\
&+\epsilon\,\Theta(\tilde{b}_{\max}-\tilde{b})\nu^2\frac{\cos^2\Theta}{\cos^2\theta}\Big[3C^4(\boldsymbol{c}_{12}\cdot\hat{\boldsymbol{k}})^2+\frac{3}{2}C^2c_{12}^2(\boldsymbol{c}_{12}\cdot\hat{\boldsymbol{k}})^2\\
&\quad-12C^2(\boldsymbol{C}\cdot\boldsymbol{c}_{12})(\boldsymbol{C}\cdot\hat{\boldsymbol{k}})(\boldsymbol{c}_{12}\cdot\hat{\boldsymbol{k}})+24C^2(\boldsymbol{C}\cdot\hat{\boldsymbol{k}})^2(\boldsymbol{c}_{12}\cdot\hat{\boldsymbol{k}})^2\\
&\quad+\frac{3}{16}c_{12}^4(\boldsymbol{c}_{12}\cdot\hat{\boldsymbol{k}})^2-3c_{12}^2(\boldsymbol{C}\cdot\boldsymbol{c}_{12})(\boldsymbol{C}\cdot\hat{\boldsymbol{k}})(\boldsymbol{c}_{12}\cdot\hat{\boldsymbol{k}})\\
&\quad+6c_{12}^2(\boldsymbol{C}\cdot\hat{\boldsymbol{k}})^2(\boldsymbol{c}_{12}\cdot\hat{\boldsymbol{k}})^2+3(\boldsymbol{C}\cdot\boldsymbol{c}_{12})^2(\boldsymbol{c}_{12}\cdot\hat{\boldsymbol{k}})^2\\
&\quad-12(\boldsymbol{C}\cdot\boldsymbol{c}_{12})(\boldsymbol{C}\cdot\hat{\boldsymbol{k}})(\boldsymbol{c}_{12}\cdot\hat{\boldsymbol{k}})^3+12(\boldsymbol{C}\cdot\hat{\boldsymbol{k}})^2(\boldsymbol{c}_{12}\cdot\hat{\boldsymbol{k}})^4\Big]\\
&+\mathcal{O}(\epsilon^2). \qquad \text{(I.9)}
\end{aligned}
$$

Then, we explicitly write $\mathcal{M}_2$, $\mathcal{M}_4$, and $\mathcal{M}_6$ as

$$
\begin{cases}
\mathcal{M}_2=\sqrt{2\pi}\,(S_1+a_2S_2+a_3S_3)\,,\\
\mathcal{M}_4=\sqrt{2\pi}\,(T_1+a_2T_2+a_3T_3)\,,\\
\mathcal{M}_6=\sqrt{2\pi}\,(D_1+a_2D_2+a_3D_3)\,,
\end{cases} \qquad \text{(I.10)}
$$

where

$$
S_1=\epsilon\int_0^\infty dc_{12}\int_0^{\tilde{b}_{\max}}d\tilde{b}\,\tilde{b}(\nu^2-\tilde{b}^2)c_{12}^5\exp\left(-\frac{1}{2}c_{12}^2\right)+\mathcal{O}(\epsilon^2), \qquad \text{(I.11)}
$$

$$
\begin{aligned}
S_2=&\epsilon\frac{1}{16}\int_0^\infty dc_{12}\int_0^{\tilde{b}_{\max}}d\tilde{b}\,\tilde{b}(\nu^2-\tilde{b}^2)c_{12}^5(15-10c_{12}^2+c_{12}^4)\exp\left(-\frac{1}{2}c_{12}^2\right)\\
&+\mathcal{O}(\epsilon^2), \qquad \text{(I.12)}
\end{aligned}
$$

$$
\begin{aligned}
S_3=&\epsilon\frac{1}{192}\int_0^\infty dc_{12}\int_0^{\tilde{b}_{\max}}d\tilde{b}\,\tilde{b}(\nu^2-\tilde{b}^2)c_{12}^5(105-105c_{12}^2+21c_{12}^4-c_{12}^6)\exp\left(-\frac{1}{2}c_{12}^2\right)\\
&+\mathcal{O}(\epsilon^2), \qquad \text{(I.13)}
\end{aligned}
$$

$$
T_1=\epsilon\frac{1}{2}\int_0^\infty dc_{12}\int_0^{\tilde{b}_{\max}}d\tilde{b}\,\tilde{b}(\nu^2-\tilde{b}^2)c_{12}^5(5+c_{12}^2)\exp\left(-\frac{1}{2}c_{12}^2\right)+\mathcal{O}(\epsilon^2), \qquad \text{(I.14)}
$$

$$
\begin{aligned}
T_2=&\frac{1}{4}\int_0^\infty dc_{12}\int_0^{\lambda}d\tilde{b}\,\tilde{b}c_{12}^7\sin^2\chi^{(0)}\exp\left(-\frac{1}{2}c_{12}^2\right)\\
&+\epsilon\left[\frac{1}{32}\int_0^\infty dc_{12}\int_0^{\tilde{b}_{\max}}d\tilde{b}\,\tilde{b}(\nu^2-\tilde{b}^2)c_{12}^5(-25-23c_{12}^2-5c_{12}^4+c_{12}^6)\exp\left(-\frac{1}{2}c_{12}^2\right)\right.\\
&\quad+\int_0^\infty dc_{12}\int_0^{\tilde{b}_{\max}}d\tilde{b}\,\tilde{b}(\nu^2-\tilde{b}^2)c_{12}^7\sin^2\frac{\chi^{(0)}}{2}\exp\left(-\frac{1}{2}c_{12}^2\right)\\
&\quad\left.+\frac{1}{4}\int_0^\infty dc_{12}\int_0^{\lambda}d\tilde{b}\,\tilde{b}c_{12}^7\chi^{(1)}\sin^2 2\chi^{(1)}\exp\left(-\frac{1}{2}c_{12}^2\right)\right]\\
&+\mathcal{O}(\epsilon^2), \qquad \text{(I.15)}
\end{aligned}
$$

$$
\begin{aligned}
T_3 =& \frac{1}{16}\int_0^\infty dc_{12}\int_0^\lambda d\tilde{b}\,\tilde{b}c_{12}^7(7-c_{12}^2)\sin^2\chi^{(0)}\exp\left(-\frac{1}{2}c_{12}^2\right)\\
&+\epsilon\left[\frac{1}{384}\int_0^\infty dc_{12}\int_0^{\tilde{b}_{\max}} d\tilde{b}\,\tilde{b}(\nu^2-\tilde{b}^2)c_{12}^5\right.\\
&\qquad\times(-525-168c_{12}^2-6c_{12}^4+16c_{12}^6-c_{12}^8)\exp\left(-\frac{1}{2}c_{12}^2\right)\\
&\quad+\frac{1}{4}\int_0^\infty dc_{12}\int_0^{\tilde{b}_{\max}} d\tilde{b}\,\tilde{b}(\nu^2-\tilde{b}^2)c_{12}^7(7-c_{12}^2)\sin^2\frac{\chi^{(0)}}{2}\exp\left(-\frac{1}{2}c_{12}^2\right)\\
&\quad\left.+\frac{1}{16}\int_0^\infty dc_{12}\int_0^\lambda d\tilde{b}\,\tilde{b}c_{12}^7(7-c_{12}^2)\chi^{(1)}\sin^2 2\chi^{(1)}\exp\left(-\frac{1}{2}c_{12}^2\right)\right]\\
&+\mathcal{O}(\epsilon^2),
\end{aligned}
\tag{I.16}
$$

$$
\begin{aligned}
D_1 =& \epsilon\frac{3}{16}\int_0^\infty dc_{12}\int_0^{\tilde{b}_{\max}} d\tilde{b}\,\tilde{b}(\nu^2-\tilde{b}^2)c_{12}^5(35+14c_{12}^2+c_{12}^4)\exp\left(-\frac{1}{2}c_{12}^2\right)\\
&+\mathcal{O}(\epsilon^2),
\end{aligned}
\tag{I.17}
$$

$$
\begin{aligned}
D_2 =& \frac{3}{16}\int_0^\infty dc_{12}\int_0^\lambda d\tilde{b}\,\tilde{b}c_{12}^7(7+c_{12}^2)\sin^2\chi^{(0)}\exp\left(-\frac{1}{2}c_{12}^2\right)\\
&+\epsilon\left[\frac{3}{256}\int_0^\infty dc_{12}\int_0^{\tilde{b}_{\max}} d\tilde{b}\,\tilde{b}(\nu^2-\tilde{b}^2)c_{12}^5\right.\\
&\qquad\times(-595-252c_{12}^2-18c_{12}^4+4c_{12}^6+c_{12}^8)\exp\left(-\frac{1}{2}c_{12}^2\right)\\
&\quad+\frac{3}{4}\int_0^\infty dc_{12}\int_0^{\tilde{b}_{\max}} d\tilde{b}\,\tilde{b}(\nu^2-\tilde{b}^2)c_{12}^7(7-c_{12}^2)\sin^2\frac{\chi^{(0)}}{2}\exp\left(-\frac{1}{2}c_{12}^2\right)\\
&\quad+\frac{3}{2}\int_0^\infty dc_{12}\int_0^{\tilde{b}_{\max}} d\tilde{b}\,\tilde{b}(\nu^2-\tilde{b}^2)c_{12}^9\sin^4\frac{\chi^{(0)}}{2}\exp\left(-\frac{1}{2}c_{12}^2\right)\\
&\quad\left.+\frac{3}{16}\int_0^\infty dc_{12}\int_0^\lambda d\tilde{b}\,\tilde{b}c_{12}^7(7+c_{12}^2)\chi^{(1)}\sin^2 2\chi^{(0)}\exp\left(-\frac{1}{2}c_{12}^2\right)\right]\\
&+\mathcal{O}(\epsilon^2),
\end{aligned}
\tag{I.18}
$$

$$
\begin{aligned}
D_3 =& \frac{3}{64}\int_0^\infty dc_{12}\int_0^\lambda d\tilde{b}\,\tilde{b}c_{12}^7(35-c_{12}^4)\sin^2\chi^{(0)}\exp\left(-\frac{1}{2}c_{12}^2\right)\\
&+\epsilon\left[\frac{1}{1024}\int_0^\infty dc_{12}\int_0^{\tilde{b}_{\max}} d\tilde{b}\,\tilde{b}(\nu^2-\tilde{b}^2)c_{12}^5\right.\\
&\qquad\times(-5145-1785c_{12}^2+798c_{12}^4+22c_{12}^6+7c_{12}^8-c_{12}^{10})\exp\left(-\frac{1}{2}c_{12}^2\right)\\
&\quad+\frac{3}{16}\int_0^\infty dc_{12}\int_0^{\tilde{b}_{\max}} d\tilde{b}\,\tilde{b}(\nu^2-\tilde{b}^2)c_{12}^7(35-14c_{12}^2+c_{12}^4)\sin^2\frac{\chi^{(0)}}{2}\exp\left(-\frac{1}{2}c_{12}^2\right)\\
&\quad+\frac{3}{8}\int_0^\infty dc_{12}\int_0^{\tilde{b}_{\max}} d\tilde{b}\,\tilde{b}(\nu^2-\tilde{b}^2)c_{12}^9(7-c_{12}^2)\sin^4\frac{\chi^{(0)}}{2}\exp\left(-\frac{1}{2}c_{12}^2\right)\\
&\quad\left.+\frac{3}{64}\int_0^\infty dc_{12}\int_0^\lambda d\tilde{b}\,\tilde{b}c_{12}^7(35-c_{12}^4)\chi^{(1)}\sin^2 2\chi^{(0)}\exp\left(-\frac{1}{2}c_{12}^2\right)\right]\\
&+\mathcal{O}(\epsilon^2).
\end{aligned}
\tag{I.19}
$$

Here, we only show the lowest order of each term. Here, $\mathcal{M}_4$ and $\mathcal{M}_6$ are, respectively, related to $\mathcal{M}_2$, the fourth moment $\langle c^4\rangle$ and the sixth moment $\langle c^6\rangle$ as

$$
\begin{cases}
\dfrac{4}{3}\mathcal{M}_2\langle c^4\rangle=\mathcal{M}_4\\
2\mathcal{M}_2\langle c^6\rangle=\mathcal{M}_6
\end{cases}
.
\tag{I.20}
$$

Substituting Eqs. (I.10) into Eq. (I.20) with $\langle c^4\rangle = (15/4)(1+a_2)$ and $\langle c^6\rangle = (105/8)(1+3a_2-a_3)$, we obtain the simultaneous equations with respect to a_2 and a_3 as

$$
\begin{cases}
(5S_1+5S_2-T_2)\,a_2+(5S_3-T_3)\,a_3=T_1-5S_1\\
\left(\dfrac{315}{4}S_1+\dfrac{105}{4}S_2-D_2\right)a_2+\left(-\dfrac{105}{4}S_1+\dfrac{105}{4}S_3-D_3\right)a_3=D_1-\dfrac{105}{4}S_1
\end{cases}
.
\tag{I.21}
$$

These equations can be solved easily and the explicit forms of a_2 and a_3 up to ϵ order are given by Eqs. (7.57)–(7.61). Thus, we explicitly write $\mathcal{M}_2$,

$\mathcal{M}_4$, and $\mathcal{M}_6$ up to the first order of ϵ as

$$\mathcal{M}_2 = \epsilon\sqrt{2\pi}\int_0^\infty dc_{12}\int_0^{\tilde{b}_{\max}} d\tilde{b}\,\tilde{b}(\nu^2-\tilde{b}^2)c_{12}^5\exp\left(-\frac{1}{2}c_{12}^2\right)+\mathcal{O}(\epsilon^2), \quad \text{(I.22)}$$

$$\begin{aligned}\mathcal{M}_4 =\epsilon\Bigg[&\frac{\sqrt{2\pi}}{2}(1-e)\int_0^\infty dc_{12}\int_0^{\tilde{b}_{\max}} d\tilde{b}\,\tilde{b}(\nu^2-\tilde{b}^2)c_{12}^5\left(5+c_{12}^2\right)\exp\left(-\frac{1}{2}c_{12}^2\right)\\ &+a_2^{(1)}\frac{\sqrt{2\pi}}{4}\int_0^\infty dc_{12}\int_0^{\lambda} d\tilde{b}\,\tilde{b}c_{12}^7\sin^2\chi^{(0)}\exp\left(-\frac{1}{2}c_{12}^2\right)\\ &+a_3^{(1)}\frac{\sqrt{2\pi}}{16}\int_0^\infty dc_{12}\int_0^{\lambda} d\tilde{b}\,\tilde{b}c_{12}^7\left(7-c_{12}^2\right)\sin^2\chi^{(0)}\exp\left(-\frac{1}{2}c_{12}^2\right)\Bigg]\\ &+\mathcal{O}(\epsilon^2),\end{aligned} \quad \text{(I.23)}$$

$$\begin{aligned}\mathcal{M}_6 =\epsilon\Bigg[&\frac{3\sqrt{2\pi}}{16}(1-e)\int_0^\infty dc_{12}\int_0^{\tilde{b}_{\max}} d\tilde{b}\,\tilde{b}(\nu^2-\tilde{b}^2)c_{12}^5\left(35+14c_{12}^2+c_{12}^4\right)\exp\left(-\frac{1}{2}c_{12}^2\right)\\ &+a_2^{(1)}\frac{3\sqrt{2\pi}}{16}\int_0^\infty dc_{12}\int_0^{\lambda} d\tilde{b}\,\tilde{b}c_{12}^7\left(7+c_{12}^2\right)\sin^2\chi^{(0)}\exp\left(-\frac{1}{2}c_{12}^2\right)\\ &+a_3^{(1)}\frac{3\sqrt{2\pi}}{64}\int_0^\infty dc_{12}\int_0^{\lambda} d\tilde{b}\,\tilde{b}c_{12}^7\left(35-c_{12}^4\right)\sin^2\chi^{(0)}\exp\left(-\frac{1}{2}c_{12}^2\right)\Bigg]\\ &+\mathcal{O}(\epsilon^2).\end{aligned} \quad \text{(I.24)}$$

Appendix J

Calculation of Ω_η^e and Ω_κ^e

In this appendix, we calculate the quantities Ω_η^e and Ω_κ^e in Eqs. (7.52) and (7.55). From the definition, $\tilde{D}_{ij}(\boldsymbol{c}) = c_i c_j - c^2\delta_{ij}/3$, $\tilde{D}_{ij}(\boldsymbol{c}_2)\Delta\left[\tilde{D}_{ij}(\boldsymbol{c}_1) + \tilde{D}_{ij}(\boldsymbol{c}_2)\right]$ is rewritten as

$$
\begin{aligned}
&\tilde{D}_{ij}(\boldsymbol{c}_2)\Delta\left[\tilde{D}_{ij}(\boldsymbol{c}_1) + \tilde{D}_{ij}(\boldsymbol{c}_2)\right] \\
=&\left(c_{2i}c_{2j} - \frac{1}{3}\delta_{ij}c_2^2\right)\left[c'_{1i}c'_{1j} + c'_{2i}c'_{2j} - c_{1i}c_{1j} - c_{2i}c_{2j} - \frac{1}{3}\delta_{ij}\left(c_1'^2 + c_2'^2 - c_1^2 - c_2^2\right)\right] \\
=&c_{12}^2(\boldsymbol{C}\cdot\hat{\boldsymbol{k}})(\boldsymbol{c}_{12}\cdot\hat{\boldsymbol{k}}) - \frac{1}{2}c_{12}^2(\boldsymbol{c}_{12}\cdot\hat{\boldsymbol{k}})^2 - 2(\boldsymbol{C}\cdot\boldsymbol{c}_{12})(\boldsymbol{C}\cdot\hat{\boldsymbol{k}})(\boldsymbol{c}_{12}\cdot\hat{\boldsymbol{k}}) \\
&+ (\boldsymbol{C}\cdot\boldsymbol{c}_{12})(\boldsymbol{c}_{12}\cdot\hat{\boldsymbol{k}})^2 + 2(\boldsymbol{C}\cdot\hat{\boldsymbol{k}})^2(\boldsymbol{c}_{12}\cdot\hat{\boldsymbol{k}})^2 - 2(\boldsymbol{C}\cdot\hat{\boldsymbol{k}})(\boldsymbol{c}_{12}\cdot\hat{\boldsymbol{k}})^3 + \frac{1}{2}(\boldsymbol{c}_{12}\cdot\hat{\boldsymbol{k}})^4 \\
&+ \epsilon\,\Theta(\tilde{b}_{\max} - \tilde{b})\nu^2\frac{\cos^2\Theta}{\cos^2\theta}\left[\frac{1}{3}C^2(\boldsymbol{c}_{12}\cdot\hat{\boldsymbol{k}})^2 - \frac{1}{2}c_{12}^2(\boldsymbol{C}\cdot\hat{\boldsymbol{k}})(\boldsymbol{c}_{12}\cdot\hat{\boldsymbol{k}})\right. \\
&\qquad + \frac{1}{3}c_{12}^2(\boldsymbol{c}_{12}\cdot\hat{\boldsymbol{k}})^2 + (\boldsymbol{C}\cdot\boldsymbol{c}_{12})(\boldsymbol{C}\cdot\hat{\boldsymbol{k}})(\boldsymbol{c}_{12}\cdot\hat{\boldsymbol{k}}) - \frac{5}{6}(\boldsymbol{C}\cdot\boldsymbol{c}_{12})(\boldsymbol{c}_{12}\cdot\hat{\boldsymbol{k}})^2 \\
&\qquad \left. - 2(\boldsymbol{C}\cdot\hat{\boldsymbol{k}})^2(\boldsymbol{c}_{12}\cdot\hat{\boldsymbol{k}})^2 + 2(\boldsymbol{C}\cdot\hat{\boldsymbol{k}})(\boldsymbol{c}_{12}\cdot\hat{\boldsymbol{k}})^3 - \frac{1}{2}(\boldsymbol{c}_{12}\cdot\hat{\boldsymbol{k}})^4\right] \\
&+ \mathcal{O}(\epsilon^2).
\end{aligned}
\tag{J.1}
$$

Substituting this result into Eq. (7.52), we obtain Eq. (7.65).

For Ω_κ^e, we rewrite $\tilde{\boldsymbol{S}}(\boldsymbol{c}_2)\cdot\Delta\left[\tilde{\boldsymbol{S}}(\boldsymbol{c}_1)+\tilde{\boldsymbol{S}}(\boldsymbol{c}_2)\right]$ as

$$
\begin{aligned}
&\tilde{\boldsymbol{S}}(\boldsymbol{c}_2)\cdot\Delta\left[\tilde{\boldsymbol{S}}(\boldsymbol{c}_1)+\tilde{\boldsymbol{S}}(\boldsymbol{c}_2)\right]\\
=&\left(c_2^2-\frac{5}{2}\right)\left[\left(\boldsymbol{c}_1'\cdot\boldsymbol{c}_2\right)c_1'^2+\left(\boldsymbol{c}_2'\cdot\boldsymbol{c}_2\right)c_2'^2-\left(\boldsymbol{c}_1\cdot\boldsymbol{c}_2\right)c_1^2-\left(\boldsymbol{c}_2\cdot\boldsymbol{c}_2\right)c_2^2\right]\\
=&C^2c_{12}^2(\boldsymbol{C}\cdot\hat{\boldsymbol{k}})(\boldsymbol{c}_{12}\cdot\hat{\boldsymbol{k}})-4C^2(\boldsymbol{C}\cdot\boldsymbol{c}_{12})(\boldsymbol{C}\cdot\hat{\boldsymbol{k}})(\boldsymbol{c}_{12}\cdot\hat{\boldsymbol{k}})+C^2(\boldsymbol{C}\cdot\boldsymbol{c}_{12})(\boldsymbol{c}_{12}\cdot\hat{\boldsymbol{k}})^2\\
&+4C^2(\boldsymbol{C}\cdot\hat{\boldsymbol{k}})^2(\boldsymbol{c}_{12}\cdot\hat{\boldsymbol{k}})^2-2C^2(\boldsymbol{C}\cdot\hat{\boldsymbol{k}})(\boldsymbol{c}_{12}\cdot\hat{\boldsymbol{k}})^3+\frac{1}{4}c_{12}^4(\boldsymbol{C}\cdot\hat{\boldsymbol{k}})(\boldsymbol{c}_{12}\cdot\hat{\boldsymbol{k}})\\
&-2c_{12}^2(\boldsymbol{C}\cdot\boldsymbol{c}_{12})(\boldsymbol{C}\cdot\hat{\boldsymbol{k}})(\boldsymbol{c}_{12}\cdot\hat{\boldsymbol{k}})+\frac{1}{4}c_{12}^2(\boldsymbol{C}\cdot\boldsymbol{c}_{12})(\boldsymbol{c}_{12}\cdot\hat{\boldsymbol{k}})^2+c_{12}^2(\boldsymbol{C}\cdot\hat{\boldsymbol{k}})^2(\boldsymbol{c}_{12}\cdot\hat{\boldsymbol{k}})^2\\
&-\frac{1}{2}c_{12}^2(\boldsymbol{C}\cdot\hat{\boldsymbol{k}})(\boldsymbol{c}_{12}\cdot\hat{\boldsymbol{k}})^3-\frac{5}{2}c_{12}^2(\boldsymbol{C}\cdot\hat{\boldsymbol{k}})(\boldsymbol{c}_{12}\cdot\hat{\boldsymbol{k}})+4(\boldsymbol{C}\cdot\boldsymbol{c}_{12})^2(\boldsymbol{C}\cdot\hat{\boldsymbol{k}})(\boldsymbol{c}_{12}\cdot\hat{\boldsymbol{k}})\\
&-(\boldsymbol{C}\cdot\boldsymbol{c}_{12})^2(\boldsymbol{c}_{12}\cdot\hat{\boldsymbol{k}})^2-4(\boldsymbol{C}\cdot\boldsymbol{c}_{12})(\boldsymbol{C}\cdot\hat{\boldsymbol{k}})^2(\boldsymbol{c}_{12}\cdot\hat{\boldsymbol{k}})^2\\
&+2(\boldsymbol{C}\cdot\boldsymbol{c}_{12})(\boldsymbol{C}\cdot\hat{\boldsymbol{k}})(\boldsymbol{c}_{12}\cdot\hat{\boldsymbol{k}})^3+10(\boldsymbol{C}\cdot\boldsymbol{c}_{12})(\boldsymbol{C}\cdot\hat{\boldsymbol{k}})(\boldsymbol{c}_{12}\cdot\hat{\boldsymbol{k}})\\
&-\frac{5}{2}(\boldsymbol{C}\cdot\boldsymbol{c}_{12})(\boldsymbol{c}_{12}\cdot\hat{\boldsymbol{k}})^2-10(\boldsymbol{C}\cdot\hat{\boldsymbol{k}})^2(\boldsymbol{c}_{12}\cdot\hat{\boldsymbol{k}})^2+5(\boldsymbol{C}\cdot\hat{\boldsymbol{k}})(\boldsymbol{c}_{12}\cdot\hat{\boldsymbol{k}})^3\\
&+\epsilon\,\Theta(\tilde{b}_{\max}-\tilde{b})\nu^2\frac{\cos^2\Theta}{\cos^2\theta}\left[-C^4(\boldsymbol{c}_{12}\cdot\hat{\boldsymbol{k}})^2-\frac{1}{2}C^2c_{12}^2(\boldsymbol{C}\cdot\hat{\boldsymbol{k}})(\boldsymbol{c}_{12}\cdot\hat{\boldsymbol{k}})\right.\\
&\quad-\frac{1}{4}C^2c_{12}^2(\boldsymbol{c}_{12}\cdot\hat{\boldsymbol{k}})^2+2C^2(\boldsymbol{C}\cdot\boldsymbol{c}_{12})(\boldsymbol{C}\cdot\hat{\boldsymbol{k}})(\boldsymbol{c}_{12}\cdot\hat{\boldsymbol{k}})+C^2(\boldsymbol{C}\cdot\boldsymbol{c}_{12})(\boldsymbol{c}_{12}\cdot\hat{\boldsymbol{k}})^2\\
&\quad-4C^2(\boldsymbol{C}\cdot\hat{\boldsymbol{k}})^2(\boldsymbol{c}_{12}\cdot\hat{\boldsymbol{k}})^2+2C^2(\boldsymbol{C}\cdot\hat{\boldsymbol{k}})(\boldsymbol{c}_{12}\cdot\hat{\boldsymbol{k}})+\frac{5}{2}C^2(\boldsymbol{c}_{12}\cdot\hat{\boldsymbol{k}})^2\\
&\quad-\frac{1}{8}c_{12}^4(\boldsymbol{C}\cdot\hat{\boldsymbol{k}})(\boldsymbol{c}_{12}\cdot\hat{\boldsymbol{k}})+c_{12}^2(\boldsymbol{C}\cdot\boldsymbol{c}_{12})(\boldsymbol{C}\cdot\hat{\boldsymbol{k}})(\boldsymbol{c}_{12}\cdot\hat{\boldsymbol{k}})-c_{12}^2(\boldsymbol{C}\cdot\hat{\boldsymbol{k}})^2(\boldsymbol{c}_{12}\cdot\hat{\boldsymbol{k}})^2\\
&\quad+\frac{1}{2}c_{12}^2(\boldsymbol{C}\cdot\hat{\boldsymbol{k}})(\boldsymbol{c}_{12}\cdot\hat{\boldsymbol{k}})^3+\frac{5}{4}c_{12}^2(\boldsymbol{C}\cdot\hat{\boldsymbol{k}})(\boldsymbol{c}_{12}\cdot\hat{\boldsymbol{k}})-2(\boldsymbol{C}\cdot\boldsymbol{c}_{12})^2(\boldsymbol{C}\cdot\hat{\boldsymbol{k}})(\boldsymbol{c}_{12}\cdot\hat{\boldsymbol{k}})\\
&\quad+4(\boldsymbol{C}\cdot\boldsymbol{c}_{12})(\boldsymbol{C}\cdot\hat{\boldsymbol{k}})^2(\boldsymbol{c}_{12}\cdot\hat{\boldsymbol{k}})^2-2(\boldsymbol{C}\cdot\boldsymbol{c}_{12})(\boldsymbol{C}\cdot\hat{\boldsymbol{k}})(\boldsymbol{c}_{12}\cdot\hat{\boldsymbol{k}})^3\\
&\quad\left.-5(\boldsymbol{C}\cdot\boldsymbol{c}_{12})(\boldsymbol{C}\cdot\hat{\boldsymbol{k}})(\boldsymbol{c}_{12}\cdot\hat{\boldsymbol{k}})+10(\boldsymbol{C}\cdot\hat{\boldsymbol{k}})^2(\boldsymbol{c}_{12}\cdot\hat{\boldsymbol{k}})^2-5(\boldsymbol{C}\cdot\hat{\boldsymbol{k}})(\boldsymbol{c}_{12}\cdot\hat{\boldsymbol{k}})^3\right]\\
&+\mathcal{O}(\epsilon^2).
\end{aligned}
\tag{J.2}
$$

Substituting this into Eq. (7.55), we obtain Eq. (7.65) after the long and tedious calculation.

Appendix K

High and low temperature expansions

We can evaluate the explicit forms of the transport coefficients in terms of high temperature expansion. We can also evaluate the dissipation rate $\mathcal{M}_2$ as a low temperature expansion, though it diverges in the low temperature limit.

First, we discuss the high temperature expansion. From Eq. (7.6), we expand ν as

$$\nu = \sqrt{1 + \frac{2\varepsilon}{Tc_{12}^2}} = 1 + \frac{\varepsilon}{T}\frac{1}{c_{12}^2} + \mathcal{O}\left(\left(\frac{\varepsilon}{T}\right)^2\right), \tag{K.1}$$

for $T/\varepsilon \gg 1$. Substituting Eq. (K.1) into Eq. (7.62), we expand $\mathcal{M}_2$ in terms of the small parameter ε/T as

$$\mathcal{M}_2^{(0)} = 0, \quad \mathcal{M}_2^{(1)} = \mathcal{M}_2^{(1,0)} + \frac{\varepsilon}{T}\mathcal{M}_2^{(1,1)} + \mathcal{O}\left(\left(\frac{\varepsilon}{T}\right)^2\right) \tag{K.2}$$

with

$$\mathcal{M}_2^{(1,0)} = 2\sqrt{2\pi}, \quad \mathcal{M}_2^{(1,1)} = 2\sqrt{2\pi}. \tag{K.3}$$

Similarly, Ω_η^e and Ω_κ^e are, respectively, expanded as

$$\Omega_\eta^{e(0)} = \Omega_\eta^{e(0,0)} + \frac{\varepsilon}{T}\Omega_\eta^{e(0,1)} + \mathcal{O}\left(\left(\frac{\varepsilon}{T}\right)^2\right), \tag{K.4}$$

$$\Omega_\eta^{e(1)} = \Omega_\eta^{e(1,0)} + \mathcal{O}\left(\frac{\varepsilon}{T}\right), \tag{K.5}$$

$$\Omega_\kappa^{e(0)} = \Omega_\kappa^{e(0,0)} + \frac{\varepsilon}{T}\Omega_\kappa^{e(0,1)} + \mathcal{O}\left(\left(\frac{\varepsilon}{T}\right)^2\right), \tag{K.6}$$

$$\Omega_\kappa^{e(1)} = \Omega_\kappa^{e(1,0)} + \mathcal{O}\left(\frac{\varepsilon}{T}\right) \tag{K.7}$$

with

$$\Omega_\eta^{e(0,0)} = -4\sqrt{2\pi}, \quad \Omega_\eta^{e(1,0)} = -\frac{11\sqrt{2\pi}}{320}, \tag{K.8}$$

$$\Omega_\eta^{e(0,1)} = \frac{\sqrt{2\pi}}{24}(\lambda-1)\left\{2(15\lambda^4+15\lambda^3+2\lambda^2+2\lambda+2)\right. \\ \left. +3\lambda^2(\lambda+1)(5\lambda^2-1)\log\frac{\lambda-1}{\lambda+1}\right\}, \tag{K.9}$$

$$\Omega_\kappa^{e(0,0)} = -4\sqrt{2\pi}, \quad \Omega_\kappa^{e(1,0)} = -\frac{1989\sqrt{2\pi}}{320}, \tag{K.10}$$

$$\Omega_\kappa^{e(0,1)} = \frac{\sqrt{2\pi}}{24}(\lambda-1)\left\{2(15\lambda^4+15\lambda^3+2\lambda^2+2\lambda+2)\right. \\ \left. +3\lambda^2(\lambda+1)(5\lambda^2-1)\log\frac{\lambda-1}{\lambda+1}\right\}. \tag{K.11}$$

Next, let us calculate the expansions of the transport coefficients. Substituting Eqs. (K.2)–(K.5) into Eqs. (7.72) and (7.73), we expand η as

$$\eta^{(0)} = \eta^{(0,0)} + \frac{\varepsilon}{T}\eta^{(0,1)} + \mathcal{O}\left(\left(\frac{\varepsilon}{T}\right)^2\right), \tag{K.12}$$

$$\eta^{(1)} = \eta^{(1,0)} + \mathcal{O}\left(\frac{\varepsilon}{T}\right) \tag{K.13}$$

with

$$\eta^{(0,0)} = \frac{5}{16d^2}\sqrt{\frac{mT}{\pi}}, \quad \eta^{(1,0)} = \frac{1567}{3840}\eta^{(0,0)}, \tag{K.14}$$

$$\eta^{(0,1)} = \eta^{(0,0)}\frac{\lambda-1}{96}\left\{2(15\lambda^4+15\lambda^3+2\lambda^2+2\lambda+2)\right. \\ \left. +3\lambda^2(\lambda+1)(5\lambda^2-1)\log\frac{\lambda-1}{\lambda+1}\right\}. \tag{K.15}$$

Similarly, κ and μ are, respectively, expanded as

$$\kappa^{(0)} = \kappa^{(0,0)} + \frac{\varepsilon}{T}\kappa^{(0,1)} + \mathcal{O}\left(\left(\frac{\varepsilon}{T}\right)^2\right), \tag{K.16}$$

$$\kappa^{(1)} = \kappa^{(1,0)} + \mathcal{O}\left(\frac{\varepsilon}{T}\right), \tag{K.17}$$

$$\mu^{(0)} = 0, \quad \mu^{(1)} = \mu^{(1,0)} + \mathcal{O}\left(\frac{\varepsilon}{T}\right) \tag{K.18}$$

with

$$\kappa^{(0,0)} = \frac{75}{64d^2}\sqrt{\frac{T}{\pi m}}, \quad \kappa^{(1,0)} = \frac{539}{1280}\kappa^{(0,0)}, \tag{K.19}$$

$$\kappa^{(0,1)} = \kappa^{(0,0)}\frac{\lambda-1}{96}\left\{2(15\lambda^4+15\lambda^3+2\lambda^2+2\lambda+2)\right.$$
$$\left.+3\lambda^2(\lambda+1)(5\lambda^2-1)\log\frac{\lambda-1}{\lambda+1}\right\}, \tag{K.20}$$

$$\mu^{(1,0)} = \frac{1185}{1024nd^2}\sqrt{\frac{T^3}{\pi m}}. \tag{K.21}$$

Let us also calculate the low temperature expansion of $\mathcal{M}_2$. From Eq. (7.6), we expand ν as

$$\nu = \frac{\sqrt{2}}{c_{12}}\sqrt{\frac{\varepsilon}{T}} + \frac{\sqrt{2}c_{12}}{4}\frac{T}{\varepsilon} + \mathcal{O}\left(\left(\frac{T}{\varepsilon}\right)^3\right). \tag{K.22}$$

Substituting Eq. (K.22) into Eq. (7.62), we can expand $\mathcal{M}_2$ in terms of the small parameter T/ε as

$$\mathcal{M}_2^{(0)} = 0, \quad \mathcal{M}_2^{(1)} = \frac{\varepsilon}{T}\mathcal{M}_{2,0}^{(1,-1)} + \mathcal{M}_{2,0}^{(1,0)} + \mathcal{O}\left(\sqrt{\frac{T}{\varepsilon}}\right) \tag{K.23}$$

with

$$\mathcal{M}_{2,0}^{(1,-1)} = 2\sqrt{2\pi}\lambda^2, \quad \mathcal{M}_{2,0}^{(1,0)} = 2\sqrt{2\pi}. \tag{K.24}$$

Appendix L

Relationship between Omega integrals and the transport coefficients

Let us introduce two dimensionless integrals $\Omega^{(\ell)*}$ and $\Omega^{(\ell,s)*}$ (ℓ, s: integer) [39, 150] as follows:

$$\Omega^{(\ell)*} \equiv \frac{2}{1-\frac{1}{2}\frac{1+(-1)^\ell}{1+\ell}} \int_0^\infty d\tilde{b}\, \tilde{b}(1-\cos^\ell \chi), \tag{L.1}$$

$$\Omega^{(\ell,s)*} \equiv \frac{1}{(s+1)!2^{s+1}} \int_0^\infty dc_{12} c_{12}^{2s+3} \Omega^{(\ell)*} \exp\left(-\frac{1}{2}c_{12}^2\right). \tag{L.2}$$

For $(\ell, s) = (1, 1)$ and $(2, 2)$, Eqs. (L.1) and (L.2) reduce to

$$\Omega^{(1)*} = 4\int_0^\infty d\tilde{b}\, \tilde{b} \sin^2 \frac{\chi}{2}, \tag{L.3}$$

$$\Omega^{(1,1)*} = \frac{1}{2}\int_0^\infty dc_{12} \int_0^\infty d\tilde{b}\, \tilde{b} c_{12}^5 \sin^2 \frac{\chi}{2} \exp\left(-\frac{1}{2}c_{12}^2\right), \tag{L.4}$$

$$\Omega^{(2)*} = 3\int_0^\infty d\tilde{b}\, \tilde{b} \sin^2 \chi, \tag{L.5}$$

$$\Omega^{(2,2)*} = \frac{1}{16}\int_0^\infty dc_{12} \int_0^\infty d\tilde{b}\, \tilde{b} c_{12}^7 \sin^2 \chi \exp\left(-\frac{1}{2}c_{12}^2\right). \tag{L.6}$$

Eqs. (L.4) and (L.6) are related to the transport coefficients as

$$D = \frac{3}{8d^2}\sqrt{\frac{mT}{\pi}} \frac{1}{\rho\Omega^{(1,1)*}}, \tag{L.7}$$

$$\eta = \frac{5}{16d^2}\sqrt{\frac{mT}{\pi}} \frac{1}{\Omega^{(2,2)*}}, \tag{L.8}$$

$$\kappa = \frac{75}{64d^2}\sqrt{\frac{mT}{\pi}} \frac{1}{\Omega^{(2,2)*}}, \tag{L.9}$$

for monodisperse particles, where D is the diffusion coefficient. Let us compare the results from the kinetic theory and those from the event-driven MD simulation. We have performed the event-driven MD simulation for $N = 1,250$, $L = 150d$, $\lambda = 2.5$, and $e = 1$. Figure L.1 shows the comparison of the diffusion coefficient of a tracer particle with that obtained by the kinetic theory with the aid of Eqs. (L.4) and (L.7), where the theoretical prediction is inconsistent with the result of MD. From Fig. L.2, a snapshot of our simulation, we can find that some pairs of particles are forming "molecules" which contain some particles within the range of the interactions. This means that aggregation processes proceed as times goes on and we cannot keep the system uniform even in the elastic limit $e \simeq 1$. The existence of aggregation processes suggests that the initial state in which all particles are out of the potential range is in a highly nonequilibrium situation. Moreover, it is hard to measure the kinetic temperature corresponding to the kinetic energy because particles are accelerated in the potential well. Therefore, we need to innovate the theoretical framework to treat such a system by taking into account the aggregation processes for the description of the diffusion process.

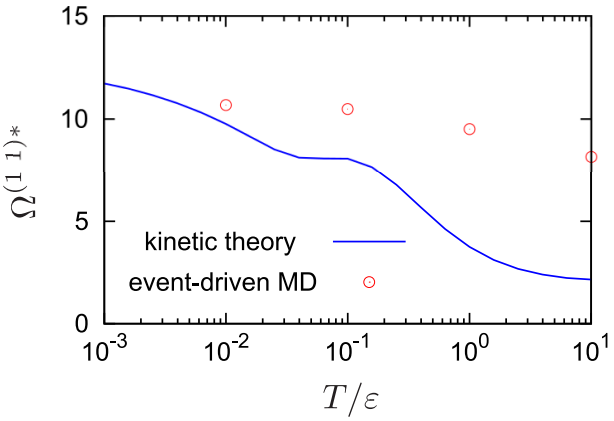

Figure L.1: The comparison between $\Omega^{(1,1)*}$ by the kinetic theory and that of the event-driven MD simulation for $N = 1,250$, $L = 150d$, $\lambda = 2.5$, and $e = 1$.

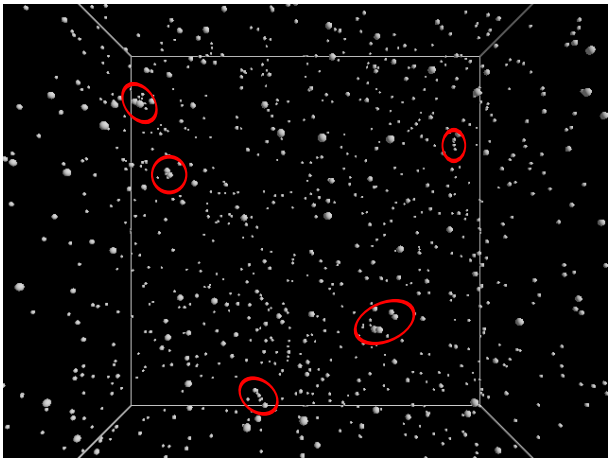

Figure L.2: The snapshot of the event-driven MD simulation at $t = 200(md^2/\varepsilon)^{1/2}$ for $N = 1,250$, $L = 150d$, $\lambda = 2.5$, and $e = 1$.

Bibliography

[1] H. M. Jaeger, S. R. Nagel, and R. P. Behringer, Rev. Mod. Phys. **68**, 1259–1273 (1999).

[2] F. Gerl and A. Zippelius, Phys. Rev. E **59**, 2361–2372 (1999).

[3] H. Hayakawa and H. Kuninaka, Chem. Eng. Sci. **57**, 239–252 (2002).

[4] A. Awasthi, S. C. Hendy, P. Zoontjens, and S. A. Brown, Phys. Rev. Lett. **97**, 186103 (2006).

[5] N. V. Brilliantov, N. Albers, F. Spahn, and T. Pöschel, Phys. Rev. E **76**, 051302 (2007).

[6] M. Suri and T. Dumitrică, Phys. Rev. B **78**, 081405 (2008).

[7] H. Kuninaka and H. Hayakawa, Phys. Rev. E **79**, 031309 (2009).

[8] K. Saitoh, A. Bodrova, H. Hayakawa, and N. V. Brilliantov, Phys. Rev. Lett. **105**, 238001 (2010).

[9] H. Kuninaka and H. Hayakawa, Phys. Rev. E **86**, 051302 (2012).

[10] H. Tanaka, K. Wada, T. Suyama, and S. Okuzumi, Prog. Theor. Phys. Supp. **195**, 101–113 (2012).

[11] R. Murakami and H. Hayakawa, Phys. Rev. E **89**, 012205 (2014).

[12] P. K. Haff, J. Fluid Mech. **134**, 401–430 (1983).

[13] I. Goldhirsch and G. Zanetti, Phys. Rev. Lett. **70**, 1619–1622 (1993).

[14] I. Goldhirsch, M-L. Tan, and G. Zanetti, J. Sci. Comput. **8**, 1–40 (1993).

[15] S. McNamara and W. R. Young, Phys. Fluids **4**, 496–504 (1992).

[16] S. McNamara and W. R. Young, Phys. Fluids **5**, 34–45 (1996).

[17] S. McNamara and W. R. Young, Phys. Rev. E **50**, R28–R31 (1994).

[18] S. McNamara and W. R. Young, Phys. Rev. E **53**, 5089–5100 (1996).

[19] S. B. Savage, J. Fluid Mech. **241**, 109–123 (1992).

[20] M. Alam and P. R. Nott, J. Fluid Mech. **377**, 99–136 (1998).

[21] J. J. Brey and M. J. Ruiz-Montero, Comp. Phys. Commun. **121–122**, 278–283 (1999).

[22] S. A. Hill and G. F. Mazenko, Phys. Rev. E **67**, 061302 (2003).

[23] V. Garzó, Phys. Rev. E **73**, 021304 (2006).

[24] K. Saitoh and H. Hayakawa, Granul. Matter **13**, 697–711 (2011).

[25] K. Saitoh and H. Hayakawa, Phys. Fluids **25**, 070606 (2013).

[26] P. Shukla and M. Alam, Phys. Rev. Lett. **103**, 068001 (2009).

[27] P. Shukla and M. Alam, J. Fluid Mech. **666**, 204–253 (2011).

[28] P. Shukla and M. Alam, J. Fluid Mech. **672**, 147–195 (2011).

[29] P. Shukla and M. Alam, J. Fluid Mech. **718**, 131–180 (2013).

[30] S. E. Esipov and T. Pöschel, J. Stat. Phys. **86**, 1385–1395 (1997).

[31] T. P. C. van Noije and M. H. Ernst, Granul. Matter **1**, 57–64 (1998).

[32] W. Losert, D. G. W. Cooper, J. Delour, A. Kudrolli, and J. P. Gollub, Chaos **9**, 682–690 (1999).

[33] F. Rouyer and N. Menon, Phys. Rev. Lett. **85**, 3676–3679 (2000).

[34] I. Goldhirsch and M - L. Tan, Phys. Fluids **8**, 1752–1763 (1996).

[35] K. C. Vijayakumar and M. Alam, Phys. Rev. E **75**, 051306 (2007).

[36] M. Alam and V. K. Chikkadi, J. Fluid Mech. **653**, 175–219 (2010).

[37] C. K. K. Lun, J. Fluid Mech. **233**, 539–559 (1991).

[38] A. Goldshtein and M. Shapiro, J. Fluid Mech. **282**, 75–114 (1995).

[39] S. Chapman and T. G. Cowling, "The Mathematical Theory of Non-uniform Gases Third Edition" (Cambridge University Press, Cambridge, 1970).

[40] S. B. Savage and D. J. Jeffrey, J. Fluid Mech. **110**, 255–272 (1981).

[41] J. T. Jenkins and S. B. Savage, J. Fluid Mech. **130**, 187–202 (1983).

[42] C. K. W. Lun, S. B. Savage, D. J. Jeffrey, and N. Chepurniy, J. Fluid Mech. **140**, 223–256 (1984).

[43] J. T. Jenkins and M. W. Richman, Phys. Fluids **28**, 3485–3494 (1985).

[44] J. J. Brey, J. W. Dufty, C. S. Kim, and A. Santos, Phys. Rev. E **58**, 4638–4653 (1998).

[45] M. Huthmann, J. A. G. Orza, and R. Brito, Granul. Matter **2**, 189–199 (2000).

[46] N. V. Brilliantov and T. Pöschel, "Kinetic Theory of Granular Gases" (Oxford University Press, New York, 2004).

[47] V. Garzó and J. W. Dufty, Phys. Rev. E **59**, 5895–5911 (1999).

[48] H. Grad, Comm. Pure Appl. Math. **2**, 331–407 (1949).

[49] J. T. Jenkins and M. W. Richman, Arch. Ration. Mech. An. **87**, 355–377 (1985).

[50] V. Garzó, in *Proceedings of RAREFIED GAS DYNAMICS: 28the International Symposium on Rarefied Gas Dynamics 2012*, edited by M. Mareschal and A. Santos, AIP Conf. Proc. No. 1501 (AIP, New York, 2005), p. 1031.

[51] J. T. Jenkins and M. W. Richman, J. Fluid Mech. **192**, 313–328 (1988).

[52] M. Tij, E. E. Tahiri, J. M. Montanero, V. Garzó, A. Santos, and J. W. Dufty, J. Stat. Phys. **103**, 1035–1068 (2001).

[53] N. Sela and I. Goldhirsch, J. Fluid Mech. **361**, 41–74 (1998).

[54] R. Ramírez, D. Risso, R. Soto, and P. Cordero, Phys. Rev. E **62**, 2521–2530 (2000).

[55] N. Mitarai and H. Nakanishi, Phys. Rev. E **75**, 031305 (2007).

[56] S. Chialvo and S. Sundaresan, Phys. Fluids **25**, 070603 (2013).

[57] K. Suzuki and H. Hayakawa, Phys. Rev. Lett. **115**, 098001 (2015).

[58] A. Santos, V. Garzó, and J. W. Dufty, Phys. Rev. E **69**, 061303 (2004).

[59] J. F. Lutsko, Phys. Rev. E **73**, 021302 (2006).

[60] N. Brilliantov, P. L. Krapivsky, A. Bodrova, F. Spahn, H. Hayakawa, V. Stadnichuk, and J. Schmidt, Proc. Natl. Acad. Sci. **112**, 9536–9541 (2015).

[61] V. Stadnichuk, A. Bodrova, and N. Brilliantov, Int. J. Mod. Phys. B **29**, 1550208 (2015).

[62] A. Castellanos, Adv. Phys. **54**, 263–376 (2005).

[63] S. Herminghaus, "Wet Granular Matter A Truly Complex Fluid" (World Scientific, Singapore, 2013).

[64] S. Herminghaus, Adv. Phys. **54**, 221–261 (2005).

[65] N. Mitarai and F. Nori, Adv. Phys. **55**, 1–45 (2006).

[66] S. Ogawa, in *Proceedings of the U.S.-Japan Seminar on Continuum Mechanical and Statistical Approaches in the Mechanics of Granular Materials*, edited by S. C. Cowin and M. Satake (Gakujitsu Bunken Fukyu-kai, Tokyo, 1978), p.208–217.

[67] N. V. Brilliantov and T. Pöschel, Phys. Rev. E **67**, 061304 (2003).

[68] N. V. Brilliantov and T. Pöschel, Europhys. Lett. **74**, 424–430 (2006), N. V. Brilliantov and T. Pöschel, Europhys. Lett. **75**, 188 (2006) (Erratum).

[69] A. Santos and J. M. Montanero, Granul. Matter **11**, 157–168 (2009).

[70] M. G. Chamorro, F. Vega Reyes, and V. Garzó, J. Stat. Mech. O07013 (2013).

[71] J. J. Brey, M. J. Ruiz-Montero, P. Maynar, and M. I. García de Soria, J. Phys.: Condens. Matter **17**, S2489–S2502 (2005).

[72] R. Brito and M. H. Ernst, Europhys. Lett. **43**, 497–502 (1998).

[73] T. P. C. van Noije and M. H. Ernst, Phys. Rev. E **61**, 1765–1782 (2000).

[74] P. M. Resibois and M. De Leener, "Classical Kinetic Theory of Fluids" (John Wiley & Sons Inc., New York, 1977).

[75] H. Krupp, Adv. Colloid Interface Sci. **1**, 111–239 (1967).

[76] J. Visser, Powder Technol. **58**, 1–10 (1989).

[77] J. M. Valverde, A. Santos, A. Ramos, and P. K. Watson, Phys. Rev. E **62**, 6851–6860 (2000).

[78] J. Tomas, Particul. Sci. Technol. **19**, 95–110 (2001).

[79] J. Tomas, Granul. Matter **6**, 75–86 (2004).

[80] J. Tomas, Chem. Eng. Sci. **62**, 1997–2010 (2007).

[81] F. Cansell, C. Aymonier, and A. Loppinet-Serani, Curr. Opin. Solid State Mater. Sci. **7**, 331 (2003).

[82] H.-J. Butt, B. Cappella, and M. Kappl, Suft. Sci. Rep. **59**, 1–152 (2005).

[83] R. Tykhoniuk, J. Tomas, S. Luding, M. Kappl, L. Heim, and H.-J. Butt, Chem. Eng. Sci. **62**, 2843–2864 (2007).

[84] G. Calvert, M. Ghadiri, and R. Tweedie, Adv. Powder Technol. **20**, 4–16 (2009).

[85] J. R. van Ommen, J. M. Valverde, and R. Pfeffer, J. Nanopart. Res. **14**, 737 (2012).

[86] J.-P. Hansen and L. Verlet, Phys. Rev. **184**, 151–161 (1969).

[87] J. J. Nicolas, K. E. Gubbins, W. B. Streett, and D. J. Tildersley, Mol. Phys. **37**, 1429–1454 (1979).

[88] Y. Adachi, I. Fijihara, M. Takamiya, and K. Nakanishi, Fluid Phase Equilibr. **39**, 1–38 (1988).

[89] A. Lotfi, J. Vrabec, and J. Fischer, Mol. Phys. **76**, 1319–1333 (1992).

[90] J. K. Johnson, J. A. Zollweg, and K. E. Gubbins, Mol. Phys. **78**, 591–618 (1993).

[91] J. Kolafa, H. L. Vörtler, K. Aim, and I. Nezbeda, Mol. Simulat. **11**, 305–319 (1993).

[92] R. H. Heist and H. He, J. Phys. Chem. Ref. Data **23**, 781–805 (1994).

[93] R. Strey, P. E. Wagner, Y. Viisanen, J. Phys. Chem. **98**, 7748—7758 (1994).

[94] K. Yasuoka and M. Matsumoto, J. Chem. Phys. **109**, 8451–8462 (1998).

[95] M. K. Müller and S. Luding, Math. Model. Nat. Phenom. **6**, 118–150 (2011).

[96] E. Murphy and S. Subramaniam, Phys. Fluids **27**, 043301 (2015).

[97] J. S. Rowlinson and B. Widom, "Molecular Theory of Capillarity" (Dover Publications, Inc., New York, 1982).

[98] C. D. Willett, M. J. Adams, S. A. Johnson, and J. P. K. Seville, Langmuir **16**, 9396–9405 (2000).

[99] K. L. Johnson, K. Kendall, and A. D. Roberts, Proc. R. Soc. London Ser. A. **324**, 301–313 (1971).

[100] J. N. Israelachvili, "Intermolecular and Surface Forces: Revised Third Edition" (Academic, New York, 2011).

[101] S. Luding, Granul. Matter **10**, 235–246 (2008).

[102] A. Singh, V. Magnanimo, K. Saitoh, and S. Luding, Phys. Rev. E **90**, 022202 (2014).

[103] S. Ulrich, T. Aspelmeier, A. Zippelius, K. Roeller, A. Fingerle, and S. Herminghaus, Phys. Rev. E **80**, 031306 (2009).

[104] S. Ulrich, T. Aspelmeier, K. Roeller, A. Fingerle, S. Herminghaus, and A. Zippelius, Phys. Rev. Lett. **102**, 148002 (2009).

[105] J. R. Royer, D. J. Evans, L. Oyarte, Q. Guo, E. Kapit, M. Möbius, S. R. Waitukaitis, and H. M. Jaeger, Nature **459**, 1110–1113 (2009).

[106] S. R. Waitukaitis, H. F. Grütjen, J. R. Royer, and H. M. Jaeger, Phys. Rev. E **83**, 051302 (2011).

[107] K. Saitoh, S. Takada, and H. Hayakawa, Soft Matter, **11**, 6345–6528 (2015).

[108] A. Onuki, Phys. Rev. Lett. **94**, 054501 (2005).

[109] A. Onuki, Phys. Rev. E **75**, 036304 (2007).

[110] A. W. Lees and S. F. Edwards, J. Phys. C: Solid State Phys. **5**, 1921–1929 (1972).

[111] T. Gerz, U. Schumann, and S. E. Elghobashi, J. Fluid Mech. **200**, 563–594 (1989).

[112] A. J. Wagner and I. Pagonabarraga, J. Stat. Phys. **107**, 521–537 (2002).

[113] J. J. Brey, J. W. Dufty, and A. Santos, J. Stat. Phys. **87**, 1051–1066 (1997).

[114] J. Jenkins and C. Zhang, Phys. Fluids **14**, 1228–1235 (2002).

[115] D. Yoon and J. Jenkins, Phys. Fluids **17**, 083301 (2005).

[116] J. F. Lutsko, Phys. Rev. E **72**, 021306 (2005).

[117] S. Takada, K. Saitoh, and H. Hayakawa, Phys. Rev. E 90, 062207 (2014).

[118] J. Lutsko and W. Dufty, Phys. Rev. A **32**, 3040–3054 (1985).

[119] D. C. Rapaport, "The Art of Molecular Dynamics Simulation" (Cambridge University Press, Cambridge, 2004).

[120] M. P. Allen and D. J. Tildersley, "Computer Simulation of Liquids" (Oxford University Press, New York, 1989).

[121] B. J. Alder and T. E. Wainwright, J. Chem. Phys. **31**, 459–466 (1959).

[122] M. W. Weber, D. K. Hoffman, and C. M. Hrenya, Granul. Matter, **6**, 239–254 (2004).

[123] G. A. Bird, "Molecular Gas Dynamics and the Direct Simulation of Gas Flows" (Oxford University Press, New York, 1994).

[124] F. J. Alexander and A. L. Garcia, Comp. Phys. **11**, 588–593 (1997).

[125] A. J. Garcia, "Numerical Methods for Physics Second Edition" (Prentice Hall, Englewood Cliffs NJ, 2000).

[126] K. Nanbu, J. Phys. Soc. Jpn. **49**, 2042–2049 (1980).

[127] K. Nanbu, J. Phys. Soc. Jpn. **52**, 3382–3388 (1983).

[128] J. J. Brey, M. J. Ruiz-Montero, and D. Cubero, Europhys. Lett. **48**, 359–364 (1999).

[129] J. M. Montanero, Trend Stat. Phys. **4**, 1–13 (2004).

[130] J. M. Montanero, A. Santos, and V. Garzó, in *Proceedings of RAREFIED GAS DYNAMICS: 24the International Symposium on Rarefied Gas Dynamics*, edited by M. Capitelli, AIP Conf. Proc. No. 762 (AIP, New York, 2005), p. 797.

[131] T. Pöschel and T. Schwager, "Computational Granular Dynamics" (Springer, Berlin, 2005).

[132] J. M. Montanero and A. Santos, Phys. Rev. E **54**, 438–444 (1996).

[133] J. J. Brey, M. J. Ruiz-Montero, and D. Cubero, Phys. Rev. E **54**, 3664–3671 (1996).

[134] S. Takada and H. Hayakawa, in *Powders and Grains 2013, Proceedings of the Seventh International Conference on Micromechanics of Granular Media*, edited by A. Yu, K. Dong, R. Yang, and S. Luding, AIP Conf. Proc. No. 1542 (AIP, New York, 2013), p. 819–822.

[135] D. J. Evans and G. P. Morriss, Phys. Rev. A **30**, 1528–1530 (1984).

[136] D. J. Evans and G. Morriss, "Statistical Mechanics of Nonequilibrium Liquids, 2nd ed." (Cambridge University Press, Cambridge, 2008).

[137] D. Chandler and J. D. Weeks, Phys. Rev. Lett. **25**, 149–152 (1970).

[138] J. D. Weeks, D. Chandler, and H. C. Andersen, J. Chem. Phys. **54**, 5237–5247 (1971).

[139] R. Kubo, M. Toda, and N. Hashitsume, "Statistical Physics II: Nonequilibrium Statistical Mechanics" (Springer, Berlin, 1991).

[140] R. Zwanzig, "Nonequilibrium Statistical Mechanics" (Oxford University Press, New York, 2001).

[141] A. Kawarada and H. Hayakawa, J. Phys. Soc. Jpn. **73**, 2037–2040 (2004).

[142] P.-G. de Gennes, J. Stat. Phys. **119**, 953–962 (2005).

[143] H. Hayakawa, Physica D **205**, 48–56 (2005).

[144] I. Goldhirsch, Annu. Rev. Fluid Mech. **35**, 267–293 (2003).

[145] I. Goldhirsch, Powder Technol. **182**, 130–136 (2008).

[146] S. Takada and H. Hayakawa, in *Proceedings of the Fourth International Symposium on Slow Dynamics in Complex Systems: Keep Going Tohoku*, edited by M. Tokuyama and I. Oppenheim, AIP Conf. Proc. No. 1518 (AIP, New York, 2013), p. 741–744.

[147] V. Garzó and A. Santos, "Kinetic Theory of Gases in Shear Flows Nonlinear Transport" (Kluwer, Dordrecht, 2003).

[148] E. M. Holleran and H. M. Hulburt, J. Chem. Phys. **19**, 232–241 (1951).

[149] J. O. Hirschfelder, R. B. Bird, and E. L. Spotz, J. Chem. Phys. **16**, 968–981 (1948).

[150] J. O. Hirschfelder, and C. F. Curtiss, "Molecular Theory of Gases and Liquids" (John Wiley & Sons, Inc., New York, 1954).

[151] I. Gallagher, L. Saint-Raymond, and B. Texier, "From Newton to Boltzmann: Hard Spheres and Short-range Potentials" (European Mathematical Society, Zürich, 2013).

[152] L. D. Landau and E. M. Lifshitz, "Mechanics Third Edition (Course Of Theoretical Physics)" (Butterworth-Heinemann, Oxford, 1976).

[153] H. Goldstein, C. Poole, and J. Safko, "Classical Mechanics Third Edition" (Addison Wesley, Bostion, 2001).

[154] C. Bizon, M. D. Shattuck, J. B. Swift, and H. L. Swinney, Phys. Rev. E **60**, 4340–4351 (1999).

[155] Z. Donkó and B. Nyíri, Phys. Plasmas **7**, 45–50 (2000).

[156] J. M. Montanero, M. Alaoui, A. Santos, and V. Garzó, Phys. Rev. E **49**, 367–375 (1994).

[157] F. Vega Reyes and J. S. Urbach, J. Fluid Mech. **636**, 279–293 (2009).

[158] F. Vega Reyes, A. Santos, and V. Garzó, Phys. Rev. Lett. **104**, 028001 (2010).

[159] Y. Gu, S. Chialvo, and S. Sundaresan, Phys. Rev. E **90**, 032206 (2014).

[160] S.-H. Chong, M. Otsuki, and H. Hayakawa, Prog. Theor. Phys. Suppl. **184**, 72–87 (2010).

[161] S.-H. Chong, M. Otsuki, and H. Hayakawa, Phys. Rev. E **81**, 041130 (2010).

[162] H. Hayakawa and M. Otsuki, Phys. Rev. E **88**, 032117 (2013).

[163] M. Abramowitz and I. A. Stegun, "Handbook of Mathematical Functions: With Formulas, Graphs, and Mathematical Tables" (Dover, New York, 1964).